THE UNIVERSITY
of ADELAIDE

SUB CRUCE LUMEN

Functional Composite Nanocarriers
for Traceable Drug Delivery

Lei Liu

A thesis submitted for the degree of Doctor of Philosophy

School of Chemical Engineering

Faculty of Engineering, Computer and Mathematic Sciences

The University of Adelaide

February 2018

Table of Contents

Thesis Declaration Statement by Author

I certify that this work contains no material which has been accepted for the award of any other degree or diploma in any university or other tertiary institution and, to the best of my knowledge and belief, contains no material previously published or written by another person, except where due reference has been made in the text. In addition, I certify that no part of this work will, in the future, be used in a submission for any other degree or diploma in any university or other tertiary institution without the prior approval of the University of Adelaide and where applicable, any partner institution responsible for the joint-award of this degree.

I give consent to this copy of my thesis, when deposited in the University Library, being made available for loan and photocopying, subject to the provisions of the Copyright Act 1968.

I also give permission for the digital version of my thesis to be made available on the web, via the University's digital research repository, the Library catalogue and also through web search engines, unless permission has been granted by the University to restrict access for a period of time.

Name of Candidate: Lei Liu

Signature: _____

Date: 18/06/2018

Acknowledgement

Over the course of my four years at the University of Adelaide as a PhD candidate, not only have I grasped incredible amount of fundamental principles of research, but I have obtained practical experiences of chemical experiments as well. I have thoroughly enjoyed the study life at Adelaide, where I have achieved the help of many people. Here I would like to take the opportunity to express my sincere gratitude to them.

Firstly, I would like to thank my principle supervisor Prof. Shi-Zhang Qiao (School of Chemical Engineering, the University of Adelaide) for his precious and invaluable supervision, support and assistances during every day of my PhD candidature. Without his kind help, I should not have the opportunity to continue my study directly after Master graduation, and have the chance to participate in a robust research group and make certain achievements. Over the past four years, I feel deeply indebted to Prof. Qiao who makes me from a real beginner of research to someone could compose research paper.

Meanwhile, I would like to convey my heartfelt thanks to my co-supervisor Prof. Sheng Dai (School of Engineering, Newcastle University). I really benefited a lot from his great theoretical and experimental knowledge, which helped me to understand my project, form novel research ideas and make pragmatic research plans.

Subsequently, I should express my appreciations to A/Prof. Jingxiu Bi. Without her assistance and kind training of cell culture related operations, I could not work on biological related experiments and conduct research on biomaterials. I also feel appreciative to Dr. Xin Du and Dr. Lin Xiong, who offer me meaningful guidance and precious assistances during my research.

Additionally, I would like to express my thanks to our analytical services coordinator Dr. Qiuhong Hu for her great and detailed training and support on numerous characterization instruments, especially confocal Raman microscopy.

Moreover, my thanks also give to the staff in Adelaide Microscopy such as Ms. Lyn Waterhouse and Mr. Ken Neubauer for their technique support and training at the very beginning of my research.

In addition, I would like to show my great gratitude to Prof Freddy Kleitz (Department of Chemistry and Centre de Recherche sur les Matériaux Avancés (CERMA), Université Laval) for his help on my research paper revision. And my thanks also should go to Prof Youhong Tang (Centre for Nano Scale Science and Technology, School of Computer Science, Engineering, and Mathematics, Flinders University) for his assistance on sample characterizations. Without their help, I could not compose the research paper successfully.

Furthermore, I am very glad to be a research student in School of Chemical Engineering, and I would like to thank all colleagues in pharmaceutical lab, Dr. Lin Xiong, Mr. Bingyang Zhang and Mr. Seonho Yun. Through corporations and communications with them, my research could conduct smoothly and effectively.

Additionally, I also show my gratitude to other members in Prof. Qiao's research group for their help and suggestions on my research study. Thanks Dr. Ji Liang, Dr. Yao Zheng, Dr. Ruifeng Zhou, Dr. Yan Jiao, Dr. Sheng Chen, Dr. Jingjing Duan, Dr. Bita Bayatsarmadi, Dr. Lei Zhang, Dr. Jingrun Ran, Mr. Jinlong Liu, Mr. Dongdong Zhu, Mr. Fangxi Xie, Ms. Xuesi Wang, Mr. Mohammad Ziaur Raham, Mr. Ye Chao, to name but a few.

The last but not the least is that I reckon it is my parents, who are always close to my heart, who deserves my acknowledgment. Without their support and encouragements, I could not be here to study and enjoy a wonderful life in Australia. I own what I have achieved today to them.

Abstract

Nowadays, nanoscale drug/gene delivery systems have formed great platforms for modern cancer therapy. Since many nanocarriers were employed for intracellular delivery applications, the potential cytotoxicity of these very small inorganic nanocarriers has raise worldwide considerations. In that case, the intracellular imaging and trace of nanocarriers' delivery performance became of utmost importance.

Different analytical techniques have been developed for bio-imaging and tracing applications. Among them, fluorescence imaging is the widely applied one. Although the detecting and analyzing technologies of fluorescence imaging are almost mature, there still existing certain inevitable issues. The fluorescent agents have rapid photo-bleaching properties, so that the fluorescence trace is far away from nondestructive method. Moreover, the auto-fluorescence of cells can get rise to background interruptions during detecting procedure. On the contrary, the intensities of Raman spectrum are more photo-stable and the Raman signals are easier to separate. The only disadvantage of Raman is that the low Inherent intensity. In that case, surface enhanced Raman scattering (SERS) technology is employed as a solution to that problem. That is why certain part of our research focus on SERS traceable delivery.

The aim of this research project is to design and discover a serial of novel functional composite nanocarriers based on conventional silica and emerging graphitic carbon nitride materials with favourable size, morphology, structure and surface modifications, which can be applied for Raman or Surface-enhanced Raman scattering (SERS) traceable drug/gene delivery. The works included in this thesis are listed as the following.

1) A new smart DDS with 5-10 nm gold nanoparticles aggregated on the surface of silica nanoparticles with an average particle diameter of ca. 80-100 nm was designed through SERS-traceable nanocarriers baring carboxylic hydrazone-conjugated. This design

displays a *sesame-bread* structure to stimulate SERS effects by the aggregation of small exposed gold seeds. It is evident that the nanocarriers have adequate biocompatibilities, while the smart DDS exhibits selective cytotoxicities between cancer and healthy cells. In here, we confirm the feasibility of SERS traceable drug delivery nanocarriers.

2) A novel stellate porous silica based delivery system was designed for SERS trace purpose. This stellate porous silica particles with an average particle size of 80-120 nm and center-radial pores of 10-30 nm were coated with in-site reduced gold nanoparticles and could materialise SERS trace after grafted SERS reporters. The trace results show high sensitivity and non-invasive features, which makes the constructed delivery system have considerable potentials to discover the dynamic delivery performances in living cells. In this work, another structured silica-gold composite nanocarrier has been constructed for SERS traceable gene delivery. We prove the SERS traceable nanocarriers could apply for gene delivery.

3) A novel ultrathin graphitic carbon nitride (g-C₃N₄) based system with small sheet size of 100-150 nm and thickness of nearly 0.6 nm was developed for small interfering RNA (siRNA) delivery. The g-C₃N₄ materials were surface modified with low molecular weight branched polyethylenimine (PEI) to obtain the capabilities of siRNA loading. The simple and label-free siRNA delivery system, which avoid possible interactions of artificial labels, shows cytotoxicity in KHOS cancer cells and good biocompatibility in HEK293 normal human cells. As g-C₃N₄ is Raman-active, the intracellular uptake performances of the label-free delivery system have been directly traced by Raman spectroscopies. In this work, we figured out a new material g-C₃N₄ that can be used for making Raman trace delivery carriers.

4) Advanced label-free g-C₃N₄ composite nanocarriers were designed for surface enhanced Raman scattering (SERS) imaging applications, and smart three-dimensional

displays a *sesame-bread* structure to stimulate SERS effects by the aggregation of small exposed gold seeds. It is evident that the nanocarriers have adequate biocompatibilities, while the smart DDS exhibits selective cytotoxicities between cancer and healthy cells. In here, we confirm the feasibility of SERS traceable drug delivery nanocarriers.

2) A novel stellate porous silica based delivery system was designed for SERS trace purpose. This stellate porous silica particles with an average particle size of 80-120 nm and center-radial pores of 10-30 nm were coated with in-site reduced gold nanoparticles and could materialise SERS trace after grafted SERS reporters. The trace results show high sensitivity and non-invasive features, which makes the constructed delivery system have considerable potentials to discover the dynamic delivery performances in living cells. In this work, another structured silica-gold composite nanocarrier has been constructed for SERS traceable gene delivery. We prove the SERS traceable nanocarriers could apply for gene delivery.

3) A novel ultrathin graphitic carbon nitride ($g\text{-}C_3N_4$) based system with small sheet size of 100-150 nm and thickness of nearly 0.6 nm was developed for small interfering RNA (siRNA) delivery. The $g\text{-}C_3N_4$ materials were surface modified with low molecular weight branched polyethylenimine (PEI) to obtain the capabilities of siRNA loading. The simple and label-free siRNA delivery system, which avoid possible interactions of artificial labels, shows cytotoxicity in KHOS cancer cells and good biocompatibility in HEK293 normal human cells. As $g\text{-}C_3N_4$ is Raman-active, the intracellular uptake performances of the label-free delivery system have been directly traced by Raman spectroscopies. In this work, we figured out a new material $g\text{-}C_3N_4$ that can be used for making Raman trace delivery carriers.

4) Advanced label-free $g\text{-}C_3N_4$ composite nanocarriers were designed for surface enhanced Raman scattering (SERS) imaging applications, and smart three-dimensional

nanocarriers were constructed for fluorescence imaging applications. By the aggregations of small gold nanoparticles on ultrathin PEI-g-C$_3$N$_4$ nanosheets, the spontaneous Raman intensity of g-C$_3$N$_4$ can be enhanced up to 5 orders of magnitude, which makes it possible for high sensitive SERS imaging. On the other hand, by using redox-sensitive non-fluorescent cross-linker to form three-dimensional smart cross-linked-g-C$_3$N$_4$ (CL-g-C$_3$N$_4$) nanocomposites, the fluorescence imaging of the designed nanocomposites can be specific and show selectivity between healthy and cancer cells. In this work, we find that advanced modified g-C$_3$N$_4$ materials have the potentials to be used for the applications of SERS and smart fluorescence traceable delivery.

All in all, this project combines the branches of material chemistry, surface chemistry, analytic technology, biology and nano-medicines together. The introduction of emerging SERS imaging and traceable methodology will give certain new knowledge and ideas of nanotechnology and bioengineering. The completion of this project will become the foundation of a series of novel inorganic nanocarriers for drug/gene delivery with outstanding performances like targeting, controllable stimuli-responsive release and higher therapeutic efficiency to against cancers and other human diseases threating on the human health. That is why this project will finally contribute to increase the health and welfare levels of individuals, society and the whole human beings.

Chapter 1 Introduction

1.1. Background and Significance

Cancer is becoming one of the greatest enemies of the human race. On account of millions of individuals are diagnosed with cancer each year, and this number is predicted to increase due to the scarcity of effective medical treatments and therapeutics. This is easily trigger the ever-elevated requirements of patients for high effective therapeutics. However, most of the anticancer drugs and genes of poor solubility and stability carry a substantial risk of systemic toxicity and have low therapeutic efficacy.[1, 2] Although certain anticancer drugs have potent chemotherapeutic features, their applications are limited by the serious side effects caused by lethal dose and the rapid resistances of cancer cells. In that case, controlled drug/gene delivery systems based on biocompatible nanocarriers are constructed to address the problems of free cargos.

To trace the delivery profiles, a series of optical bio-imaging methods can be used, such as single fluorescence, two-photon fluorescence, Raman scattering and surface-enhanced Raman scattering(SERS). SERS enjoys high detection sensitivity, good stability, high resolution, water-free interfering and still available if fluorescence quenching, to name but a few. Since Fleischmann et.al first observed the clearly sharp Raman characteristic band on a rough silver electrode with pyridine adsorption in 1974, SERS technology has been rapidly developed.[3] But at that time, the reason of the SERS phenomenon was not sure and many researches on SERS mechanism were in the downturn in the later 10 years. Until the late of 20th century, owning to the researches and developments of nanotechnology, SERS technique was revived. In 1997, the SERS phenomena of single molecule can be regarded as a milestone, which demonstrated that

the detected signal intensity of Raman scattering spectrum was not inferior to those of fluorescence.[4] SERS technique is widely applied to the surface studies, the orientation of biological macromolecules and interface configuration, conformational studies, structural analysis as well as tracing delivery.

This project combines the branches of material chemistry, surface chemistry, SERS analytic technology, biology and nanomedicines together. The introduction of novel SERS imaging traceable methodology will give certain new knowledge and ideas of nanotechnology and bioengineering. The completion of this project will be the foundation of a series of novel inorganic nanocarriers for drug/gene delivery with outstanding performances like targeting, controllable stimuli-responsive release and higher therapeutic efficiency to against cancers and other human diseases threating on the human health.

1.2. Objective and Outline of Thesis

The aim of this research project is to design and discover a serial of novel functional composite nanocarriers based on conventional silica and emerging two dimensional graphitic carbon nitride materials with favourable size, morphology, structure and surface modifications, which can be applied for Raman, surface-enhanced Raman scattering (SERS) and smart fluorescence traceable drug/gene delivery. The main achievements acquired in this thesis are presented in the form of one published paper in peer-reviewed journals and three unpublished and unsubmitted works written in manuscript style. The following chapters in this thesis are organized in accordance with the order below:

In chapter 2, a literature review regarding to the developments from controlled

drug/gene delivery systems, nanoparticle based delivery systems, all the way narrow to inorganic silica, carbon, two dimensional nanocarriers like graphitic carbon nitride. In addition, this section will also review the optical bio-imaging or analytical technologies of tracing delivery.

In chapter 3, smart drug delivery systems (DDSs) were constructed for non-destructive SERS tracing and targeted cancer-cell cytotoxicities. The 5-10 nm gold nanoparticles aggregated on the surface of silica nanoparticles to form hot spots and enhanced general Raman signals of the attached SERS reporter, while the covalent pH-cleavable linkage between drugs and carriers provided the DDSs with targeted cytotoxicities of cancer cells. The excellent and strong integration of gold and silica nanoparticles ensured that the designed DDS have the capability to be traced by SERS during delivery processes in certain severe environments, especially blood circulations. The feasibility of SERS trace is validated. This work has been published in Nanoscale, **2016**, 8, 12803-12811.

In chapter 4, a novel stellate porous silica based delivery system with an average particle size of 80-120 nm and center-radial pores of 10-30 nm was designed for SERS trace purpose. The results show that designed stellate porous silica-gold composite delivery system could materialise SERS trace, and show high sensitivity and non-invasive features, which makes the constructed delivery system have considerable capabilities to discover the delivery performances in vitro. This work was prepared as manuscript to be submitted.

In chapter 5, graphitic carbon nitride (g-C_3N_4) and Low molecular weight polyethylenimine (PEI) composites were constructed as novel small interfering RNA (siRNA) delivery systems. The novel ultrathin graphitic carbon nitride (g-C_3N_4) with small sheet size of 100-150 nm and thickness of nearly 0.6 nm was surface grafted with

3

PEI to ensure loading siRNA. As g-C_3N_4 is Raman-active, the intracellular uptake performances of the label-free delivery system can be directly traced by Raman spectroscopies. The Raman spectrum of g-C_3N_4 was also further validated by theoretically calculation via a Gaussian 09 software. Raman traced images demonstrated higher sensitivity and resolution than common fluorescence traced results, which showed Raman is a better method for real-time tracing and revealing nano-toxicity of delivery carriers. This work was prepared as a manuscript to be submitted.

In chapter 6, advanced label-free g-C_3N_4 composite nanocarriers were designed for surface enhanced Raman scattering (SERS) imaging applications, and smart three-dimensional nanocarriers were also constructed for fluorescence imaging applications. By modification of small gold nanoparticles on ultrathin PEI-g-C_3N_4 nanosheets, the spontaneous Raman intensity of g-C_3N_4 can be enhanced up to 5 orders of magnitude, which makes it possible for high sensitive SERS imaging. Three-dimensional g-C_3N_4 structure shows fluorescence quenching (static quenching), where a single fluorescent PEI-g-C_3N_4 nanosheet makes a ground state complex with the fluorophore so that it becomes nonfluorescent. Later, based on thiol-disulfide exchange reaction of glutathione (GSH) and disulfide cross-linker, higher concentration of GSH in cancer cells could easily cut the linkage between PEI-g-C_3N_4 nanosheets. By using redox-sensitive non-fluorescent cross-linker to form three-dimensional CL-g-C_3N_4 nanocomposites, the fluorescence imaging can be specific and show selectivity between healthy and cancer cell. The decrease in the quantum yield of fluorescence intensity caused by quenching can be recovered. This work was prepared as a manuscript to be submitted.

In chapter 7, the general concluding remarks of this thesis and perspective on the future directions of the research are proposed.

1.3. References

[1]   X. Zhang, F. Li, S. Guo, X. Chen, X. Wang, J. Li, Y. Gan, *Biomaterials* **2014,** *35,* 3650.

[2]   F. Qiu, D. Wang, Q. Zhu, L. Zhu, G. Tong, Y. Lu, D. Yan, X. Zhu, *Biomacromolecules* **2014,** *15,* 1355.

[3]   S. Schlucker, *Angewandte Chemie* **2014,** *53,* 4756.

[4]   K. A. Stoerzinger, J. Y. Lin, T. W. Odom, *Chemical Science* **2011,** *2,* 1435.

Chapter 2 Literature Review

2.1. Introduction

2.1.1. Controlled Drug/Gene Delivery System

Cancer is regarded as a serious threat on the human health, because millions of human beings are diagnosed with cancer every year, and the number is predicted to increase due to the scarcity of effective medical treatments and therapeutics. Consequently, cancer may in all probability become one of the greatest enemies against the human race. Currently, most of the anticancer drugs and gene medicines such as small molecule anticancer drugs, proteins, siRNA, and DNA have severe issues, which may be caused by poor solubility and stability, high dosage, in vivo degradation, short circulating half-life, poor pharmacokinetic profiles, lack of selectivity of cancer cells and non-specific target delivery. These medicines carry a substantial risk of systemic toxicity and have low therapeutic efficacy.[1, 2] Under that situation, numerous cancer patients are urged for the treatments of high effective therapeutics formulations. Alarmingly, although certain anticancer drugs have potent chemotherapeutic features, these 'free' cargos applications are limited by the serious side effects caused by lethal dose and the rapid resistances of cancer cells.[3-5] That is why drug/gene delivery system has been established. A drug delivery system can be recognized as a formulation, which controls the time-release dosage of drug delivery and targets specific areas of the body (like cancer cells). As a result, the last decade has witnessed an exponential increase in the researches on the formulation manufactures of controlled drug/gene delivery.
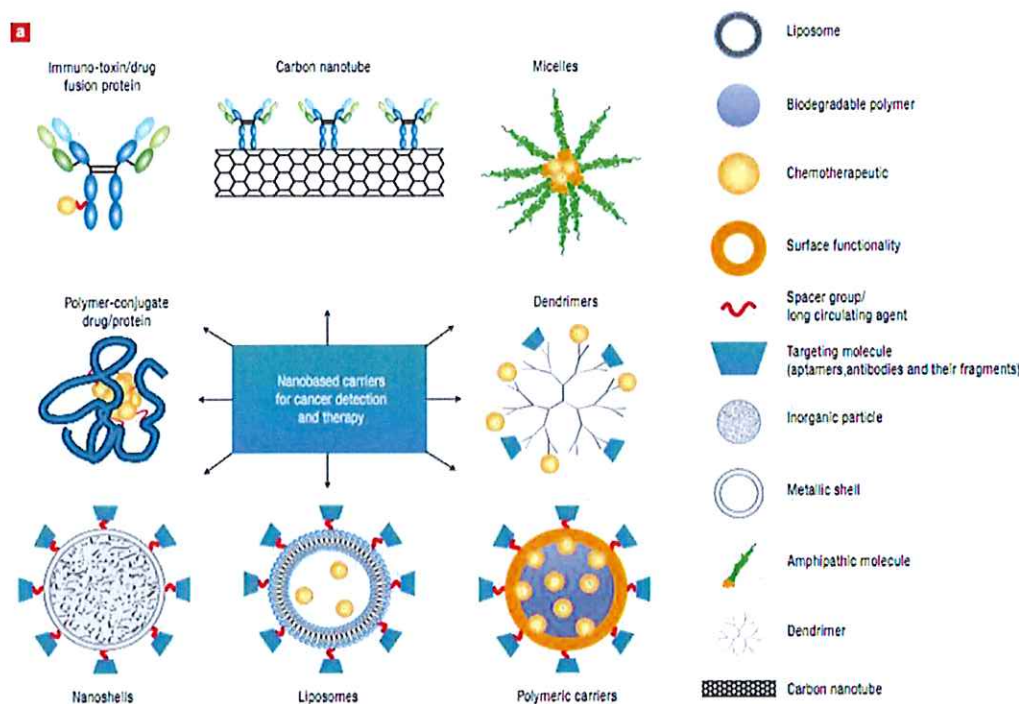
Figure 2.1. The examples of anticancer nanocarriers. Reproduced with permission. Copyright (2007) Nature Publishing Group.

2.1.2. Nanoparticles based Delivery Carriers

Nowadays, nanoscale drug/gene delivery systems (**Figure 2.1**) such as immune-toxin/drug fusion protein, carbon nanotube, micelles, polymer-conjugate drug/protein, dendrimers, nanoshells, liposomes, polymeric carriers and nano-capsules have formed great platforms for modern cancer therapy.[6, 7] However, there are still several hurdles in the developments of drug/gene delivery systems. It was hard to let the nanocarriers encapsulate adequate drug or control the drug directly release to the target positions in human vivo environment[8]. What is worse, the issues like the toxicity of applied nanomaterials as well as the high expenses and costs of procedures are still in the way of the fabrication of drug/gene delivery systems. All in all, an excellent delivery system is expected to widely distribute in nature and safe to human beings, no burst or premature release, efficient cellular uptake and controlled cargo release. Controlled

drug delivering to targeted cells is still one of the challenges of contemporary medical treatments. This review will focus on the developments of certain inorganic nanoparticle based carriers like silica, carbon nanotubes and graphene as well as the emerging two dimensional graphitic carbon nitride nanocarriers.

2.2. Silica Nanocarriers Developments

Unlike the carrying materials such as polymeric carriers (nanogel and micelle) and liposome delivery vectors, inorganic silica has excellent properties such as high stability for mechanical and thermal changes, high biocompatibility, efficacious fabrication cost and low toxicity.[9-14] In addition, the silica particles may avoid non-specific and deleterious changes to the human body in vivo circumstance.[13]

2.2.1. Structural Developments of Silica Nanoparticle

In accordance with structures and particle morphologies, the silica nanoparticle developments can be divided into three generations[15]. In 1968, Stöber and co-workers first fabricated solid silica spheres by adding silica precursor tetraethyl orthosilicate (TEOS) in a mixed solution of ethanol, aqueous ammonia and water.[16] These one level structural solid silica spheres shown in **Figure 2.2a** are regarded as the first generation of spherical silica nanoparticles.

Then after 24 years later in 1992, silica nanoparticles with hexagonal arrays of uniform sized mesochannels, so called Mobil composite material number 41 (MCM-41), had been synthesized from cetyltrimethylammonium bromide (CTAB) template and first reported by Mobil Oil Company.[17] Hollow spherical silica nanoparticles had been synthesized by numerous approaches like colloidal template[18], sol–gel, hard-template with sol–gel[19], hard-template with layer-by-layer assembly, soft-template

methods[20]. Mesoporous silica nanospheres such as MCM-41(hexagonal), MCM-48 (cubic), and MCM-50(lamellar) are solid materials, and their internal porous structure is like a honeycomb which consists of a great many empty channels (mesopores) , which are used to load the molecules of guest drugs. When the concentration of mesoporous silica nanospheres is adequate, they have greater biocompatibility than amorphous silica materials.[21] These mesoporous silica nanoparticles with an average diameter pore size ranging from 2 to 50 nm have been regarded as the second generations. Two-level-structure silica is shown in **Figure 2.2b**.
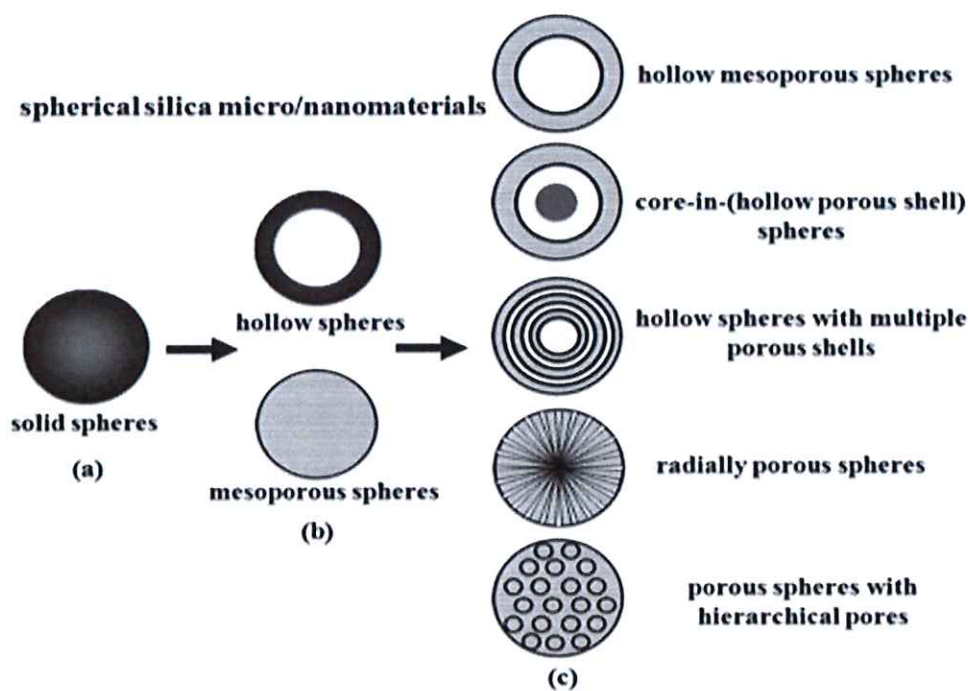
Figure 2.2. Structural developments of spherical silica nanoparticles, a) first generation of solid spheres, b) second generation structures of silica and c) third generations of silica. Reproduced with permission. Copyright (2011) The Royal Society of Chemistry.

Finally, spherical silica nanoparticles with hierarchical structures are recognized as the third generations shown in **Figure 2.2c**. Firstly, hollow mesoporous spherical silica nanoparticles (HMSNs) are consisted of thin nanoshells with ordered mesochannels

9

penetrating from outside to the interior cages, and they could be fabricated by multi-phase polymerization, emulsion or interface assembly, active surfactant polymerization assembly, self-assembly as well as electrostatic interaction layer assembly methods etc.[8] And among them, one of the effective and efficient way is the template method, which can be categorized into three classifications, which are soft (oil-in-water emulsion, surfactant vesicles)[22], hard (hard spherical particles)[23] and self-template (solid silica sphere itself)[24] approaches. Additionally, core-in-hollow porous shell sphere or the so-called rattle-type structure or yolk/shell structure silica has a core in the cage of the mesoporous shell. The preparations of yolk/shell silica are including core–vesicle complex fabrication from surfactant, mesostructured silica shell deposition, TEOS hydrolysis and condensation and surfactant removal under calcination.[25-28] In addition, hollow porous silica spheres with multiple concentric shells are a combination of several HMSNs, and they are usually synthesized by dual-template or co-surfactants methods.[29-32] The last but not the least third-generation structure are porous silica spheres with hierarchical pores or dendritic nanoparticles. They are silica nanoparticles, which are consisted of center-radial large pores structures with mesochannels on the wall of pores.[33]

2.2.2. Multifunctional Mesoporous Silica Nanoparticles

Non-invasive and biocompatible mesoporous silica nanoparticles (MSNs) have fundamental features like large specific surface area, good porosity and high chemical and thermal stabilities. Since the Mobil composite material number 41 (MCM-41) mesoporous silica materials was first involved in DDS by Vallet-Regí and co-workers in 2001[34], an overwhelming majority of research breakthroughs and advances of mesoporous silica nanoparticles (MSNs) have been made in nanotechnologies areas to benefit biomedicine and clinical trials significantly over the past few decades[35, 36].

Based on specific structures and morphologies, MSNs can be independently medicated on particle framework, outer particle shells and inter surface mesochannels to obtain multifunctional MSNs platform. As concluded in **Figure 2.3**, after functionalized by tracking marker, spacer, targeting ligands, gatekeeper and endosomal escape triggers, MSNs can also be given additional properties like traceable features, dispersibility, targeting specificity, stimuli-responsive and release-control possibilities[12].

Currently, these inorganic nanocarriers can be further functionalized and equipped with several desired functional groups like amino ($-NH_2$)[37], phenyl ($-C_6H_5$)[38], thiol (-SH)[39], and vinyl ($-CH=CH_2$)[40] to synthesize a multifunctional composite for the specific stimuli-controls of delivery profiles. The modification of -Si-OH groups can be both on the particle surfaces and pores. In addition, certain polymers such as polyethylene glycol (PEG), polyethylene imine (PEI)[41], poly-vinyl pyrrolidone (PVP)[42]and poly-L-lysine (PLL)[43] can change the surface charge of nanoparticles and therefore provide them with high capacity of loading large molecules and high biocompatibility in vitro circumstance. To date, considerable amounts of studies have been researched on inorganic nanomaterials with stimuli-responsive functions such as temperature[44, 45], pH[46-48], light[49], external magnetic fields[50-52] as well as enzymes[39, 53]. In addition, a series of targeting ligands such as small molecules like folic acid (vitamin B9)[54], biotin (vitamin B7)[55], peptides and proteins like octreotide[56], RGD peptides[57], and antibody fragments are grafting on the surface of drug vehicles to enhance nanocarriers specific delivery to targeted cells[12, 58].
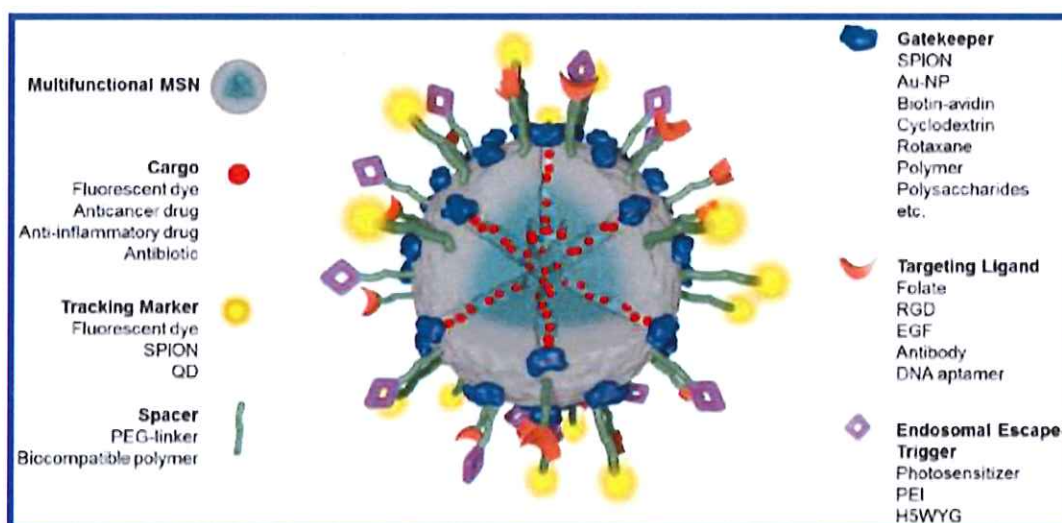
Figure 2.3. The illustration of multifunctional MSNs for stimuli-responsive controlled release. SPION: superparamagnetic iron oxide nanoparticle; QD: quantum dot; PEG: poly (ethylene glycol); Au-NP: gold nanoparticle; RGD: Arg-Gly-Asp amino acid sequence; EGF: epidermal growth factor; PEI: poly (ethylene imine); H5WYG: endosomolytic peptide. Reproduced with permission. Copyright (2014) American Chemical Society.

2.3. Developments of Carbon and Two-dimensional Nanocarriers
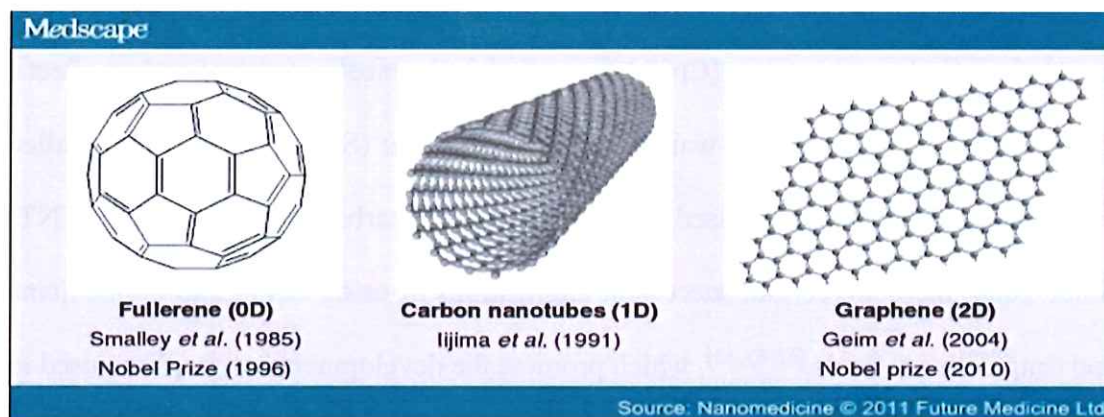
2.3.1 Carbon Nanocarriers

Nanoscale carbon materials are also considered as one of the promising carriers. On account of their small size and unique structures, they are possibly be used to probe, adjust and control drug/gene delivery at the intracellular and subcellular levels[59].

According to the difference of dimensions (**Figure 2.4**)[60], manufactured Sp^2-carbon nanomaterials are divided into three types, which are fullerene (zero dimensional, 0D), carbon nanotubes (one dimensional, 1D) and graphene (two dimensional, 2D). Functionalized fullerenes were reported as delivery carriers of the green fluorescent protein gene in vitro and in vivo to get higher gene expression[61]. Carbon nanotubes[62,

[63] as well as carbon nanohorns[64] were also employed as carriers for controlled drug delivery and release, which achieved high drug-loading capacity and stabilities in blood circulation. Carbon nanotubes (CNTs) are cylindrical nanostructures of carbon sheets. They are classified as single-walled carbon nanotubes (SWNTs) and multi-walled carbon nanotubes (MWNTs) based on the number of the carbon sheets formed the CNTs. Since 2004, there are certain successful applications of using CNTs into biomedicine and drug delivery fields [62, 63, 65], which promote the developments of graphene used in drug delivery. As an emerging class of manufactured nanocarbon materials, two dimensional graphene also exhibits their possibility in drug delivery fields. Because every atom of graphene is exposed on the surface [66-68], it has large surface area, which in turn contributes to ultra-high drug loading capability and efficiency.

Although SWNTs and graphene have promising features like extremely high drug loading efficiency and little cytotoxicity after surface modification, they have adverse problems. They are by no means biodegradable, and the long-term toxicity of carbon nanotubes and graphene are still need to be seriously considered. What is even worse is that the shortage of active sites and steric hindrances of SWNTs and graphene limited the further functionalization of functional groups on them. That is to say, after surface functionalized with linkers, they are difficult to further graft targeting ligands and traceable labels. As an advanced of graphene, subsequently in 2008, graphene oxide (GO) was first applied by Dai and co-workers [69, 70] as drug nanocarriers for anticancer drugs SN38 and doxorubicin. GO has many oxygen-containing functional groups, so the targeting ligands can be directly functionalized, which offer GO flexibility in drug/gene delivery. In terms of toxicity analysis, non-functionalized GO has high cytotoxicity and unstable in physiological circumstances. [60] To address that problem, polyethylene glycol (PEG) was used to modify GO surface and to decrease the toxicity

of many cells in vitro.[69, 70]

Figure 2.4. Three major types of Sp^2-nanosized carbons. Reproduced with permission. Copyright (2011) Future Medicine Ltd

2.3.2 Two Dimensional Nanocarriers-especially Graphitic Carbon Nitride

The successfully isolation and investigation (2010 Nobel Prize) of the graphene motivated and sparked the search of a series of new two-dimensional materials (2DMs) with unique optical, electrical and thermal features.[71-73] Based on the previous studies of mesoporous nanoparticles, the large surface area of mesopores highly contribute to efficient cargo loading[74]. In that case, 2DMs with ultrathin thickness and two dimensional morphologies, which provide ultrahigh surface-area for loading and adsorbing guest cargos, could be ideal carriers for drug/gene delivery system. Another benefit of the thin 2DMs is the rapid-response of stimuli like light and laser, which contribute to effectiveness of optical therapies such as photo-thermal[75, 76] and photodynamic therapy[77, 78].

As summarized in **Figure 2.5**, 2DMs such as layered double hydroxides (LDHs)[79], ultra-thin black phosphorous (BP)[80, 81], graphitic carbon nitride (g-C$_3$N$_4$)[77, 82, 83], hexagonal boron nitride (hBN, so called 'white graphene')[84], transition metal

dichalcogenides like MoS_2[85] and WS_2[86] have been used in numerous bio-applications including cancer theranostics, antimicrobial activity, tissue engineering, bio-sensing, and bio-imaging and tracing applications.
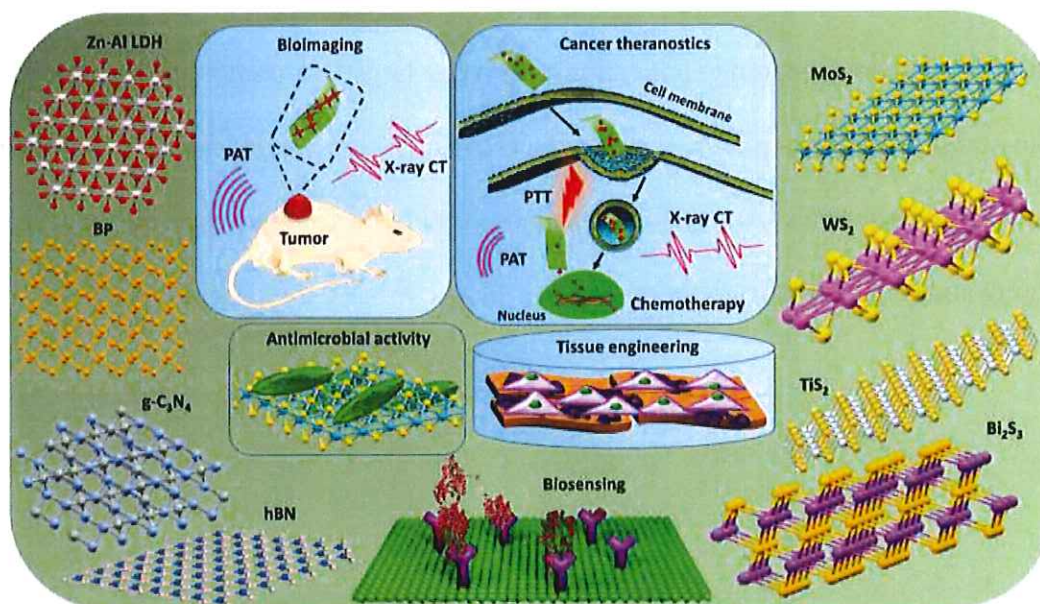
Figure 2.5. Molecular structures and bio-applications of 2DMs. Reproduced with permission. Copyright (2016) WILEY-VCH Verlag GmbH & Co. KGaA, Weinheim.

Unlike other 2DMs, g-C_3N_4 has promising water dispersibility without further surfactants or oxidation treatments, and that is why it can be easily direct-exfoliated in aqueous solutions like water.[77, 87] In addition, g-C_3N_4 also hold great features like small sheet size, high hydrophilicity and low toxicity, which makes it as a wonderful material for forming delivery vehicles. For instances, a kind of water-dispersed exfoliated g-C_3N_4 nanosheets with pH-dependent photoluminescence (PL) was reported as fluorescence nanocarriers for imaging within HeLa cells (**Figure 2.6**)[83]. Ultrathin g-C_3N_4 nanocarriers with an average hydrodynamic diameter of 55 nm and 1.1 nm thickness were fabricated for anticancer drug (doxorubicin, Dox) delivery and photodynamic therapy[77]. Graphene-like g-C_3N_4/Fe_3O_4 nanocomposites were

synthesised for controlled magnetically targeting drug delivery[82]. Graphitic hollow carbon nitride nanospheres were constructed as photochemical internalization photo-sensitizers, imaging agents and drug carriers to conquer endo/lysosomal restriction[78]. Single-layered biocompatible g-C$_3$N$_4$ quantum dots (QDs) were introduced to two-photon fluorescence imaging applications, for it has large two-photon absorption, high photo-stability and great photo-thermal effect[88]. The tunable large band-gaps and good fluorescence properties of g-C$_3$N$_4$ have made it suitable for fluorescence-based bio-imaging and tracing applications.
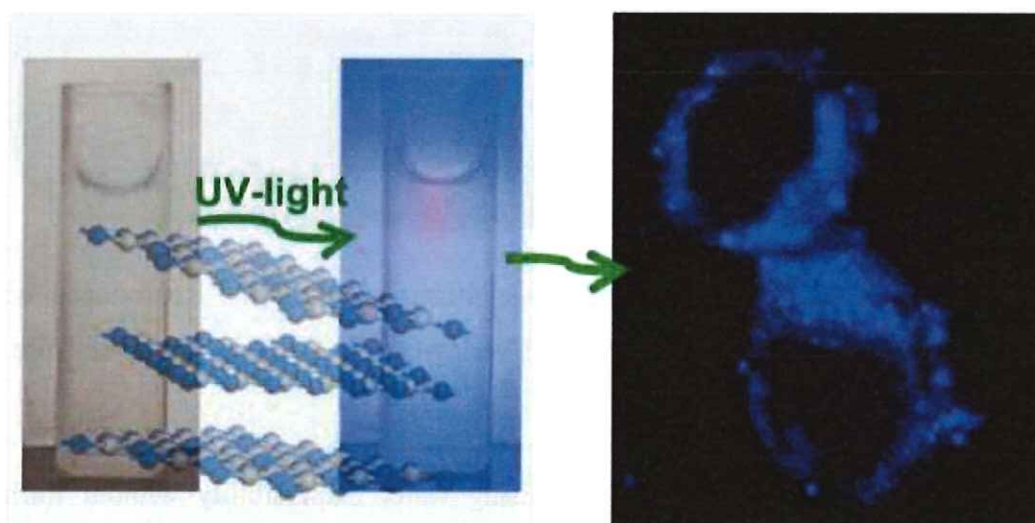
Figure 2.6. The image of g-C$_3$N$_4$ nanosheets dispersed in water. From left to right are optical image under nature-light, under UV-light and bio-image of g-C$_3$N$_4$ nanosheets in HeLa cells. Reproduced with permission. Copyright (2013), American Chemical Society.

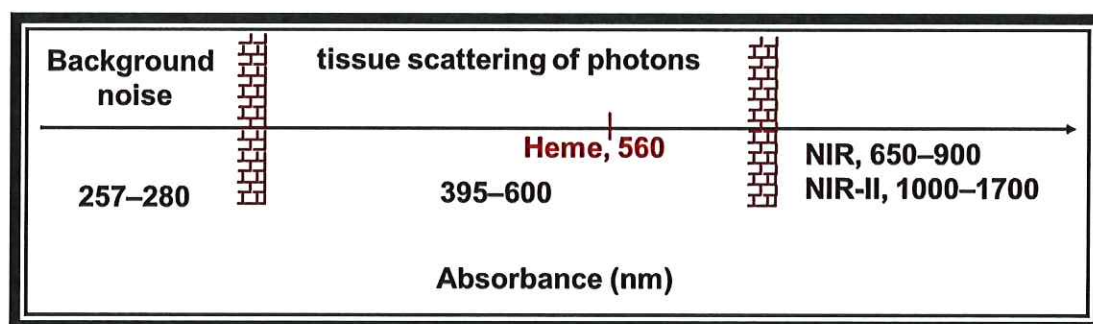## 2.4. Optical Bio-Imaging and Tracing Delivery

Optical imaging is a non-invasive, low cost and high sensitivity technique with short acquisition time and multiplexing capability, which uses special properties of visible light or photons to achieve detailed images of organs, tissues, and smaller structures

such as cells and even molecules[89, 90]. The common chemically-selective optical imaging methods are mainly including fluorescence (FL) imaging, two-photon FL imaging (TPFI) and Raman imaging, to name but a few. In addition, using imaging method in drug/gene delivery field, the imaging reporters, no matter fluorescence or Raman, can conjugated with either nanocarriers or guest cargos to enable tracing delivery.

2.4.1 Fluorescence Imaging and Two-Photon Fluorescence Imaging (TPFI)

Non-destructive fluorescence imaging is based on photons emitted from fluorescent reporters, which play a crucial role in a variety of biological areas such as drug/gene delivery. However, there still exists a great many problems to conduct safe and effective imaging processes. The issues are including but not limited by photo-bleaching, photo-toxicity and photo-thermal effects of fluorescence reporters[91]. Despite that, optical fluorescence bio-imaging method also has certain inevitable limitations (**Figure 2.7**). In the region of 257-280 nm, due to tissue auto-fluorescence and light absorption by proteins, the imaging results could be interrupted by the backgrounds. While in the visible light region of 395-600 nm, the imaging may also be influenced by strong tissue scattering of photons such as heme groups with absorbance maximum at 560 nm[92, 93]. To overcome these barriers, near-infrared window (NIR, 650–900 nm) and second NIR window (NIR-II, 1000–1700 nm) imaging approaches have been established with the advantages of reduced auto-fluorescence, and tissue scattering for optical-imaging. Compared with single-photon excitation using one continuous-wave lasers, two-photon nonlinear excitation requires high reflux of excitation photons, usually by a femtosecond laser. These nonlinear excitation generates relatively high level of spatial resolution and decreases photo-bleaching. Because of low Rayleigh scattering and low tissue absorption of NIR light, two-photon fluorescence imaging (TPFI) approach could

reduce the influence of background, get larger imaging depth, reduced low photo-damages[88, 94]. Additionally, the two-photon excitation wavelength is regarded as the range of 700–1350 nm, which is great for imaging biological agents in deep areas.

Background noise	tissue scattering of photons		NIR, 650–900
Heme, 560		
257–280	395–600	NIR-II, 1000–1700
	Absorbance (nm)	

Figure 2.7. Barriers of optical imaging.

2.4.2 Raman Imaging

Raman scattering (RS) imaging technology is based on the inelastic scattering of photons. When a beam of light illuminates the substance, most photons are elastically scattered (Rayleigh scattering) from an atom or molecule. Due to the conservation of energy, scatted photons have the same energy as the incident photons. For RS, small fractions of photons are inelastically scattered, so the energy of these photons are different from the incident photons. If the vibrational quantum is excited, the scattering is called Stokes Raman scattering. However, when the vibrational quantum is annihilated, it is an anti-Stokes Raman scattering. Raman spectroscopy is a real-time characterization and detection of molecular structures based on the polarizability of samples. That is why Raman can provide more information than Infrared spectroscopy based on the dipole moment of samples.[95] Unlike fluorescence which has problems such as rapid photo-bleaching properties of fluorescent agents and the background interruptions from auto-fluorescence of cells, the intensity of Raman spectra are more

photo-stable and Raman spectra are not easily influenced by the auto-fluorescence background.[96] Moreover, Raman scattering can be processed in aqueous conditions. As high polarity water is a very weak Raman scatterer and strong Infrared absorber, Raman related technologies are superior for biological based characterizations.

The Raman spectrum can be divided into three parts, which are fingerprint region below 1800 cm^{-1}, the silent region of 1800–2800 cm^{-1} and the high frequency region above 2800 cm^{-1}[97]. To imaging a single cell is to define the Raman spectrum of major building block molecules of a cell comprise proteins, nucleic acids, lipids as well as phospholipids, and carbohydrates among others. Raman spectra of cells[98] and an overview of important band positions[99] in regions <1800 cm^{-1} and >2800 cm^{-1} mainly contains proteins, nucleic acids, and lipids. (**Figure 2.8.and Table 2.1**)

Admittedly, although Raman has the above merits, conventional spontaneous Raman has a great problem of low intensity. In order to obtain the Raman spectra for nanocarriers with low inherent Raman intensity, the high laser irradiation and long acquisition times are inevitably required. But they could trigger serious heat problems and damage the detecting cells. In order to address that problem, the solutions can be clarified into two major methods. One is increasing the intensity and energy of incident light, and the other one is using alternative analytical method based on the localized surface plasmon resonance, which triggers the emergence of surface-enhanced Raman scattering (SERS)[100].
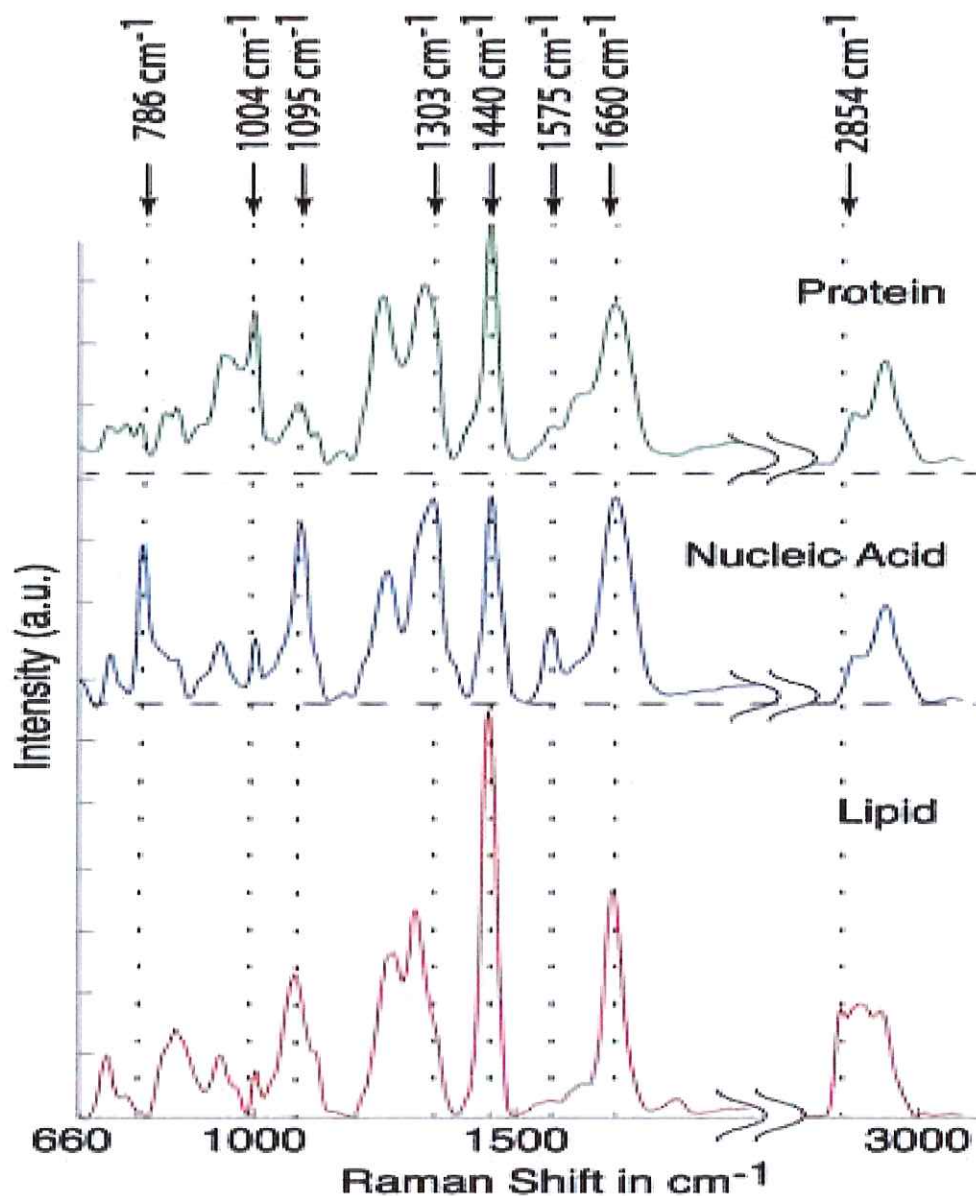
Figure 2.8. Raman spectra of important cellular molecules, protein, nucleic acid and lipid. Reproduced with permission. Copyright (2014) The Royal Society of Chemistry

Table 2.1. An overview of important band positions and cell related functional groups. Reproduced with permission. Copyright (2015) Elsevier B.V.

Band position [cm-1]	Assignment		
785-788	Pyrimidine bases	Ringbreathing	Nucleic acid
1002-1005	Phenylalanine	Symmetric stretch	Proteins
1092-1095	O-P-O	Symmetric stretch	Nucleic acid backbone, phospholipids
1254-1255	Amide III	CH/NH deformation	Proteins
1425-1475	CH_2, CH_3	Deformation	Proteins, lipids
1655-1662	Amide Ⅰ	C=O stretching mode	Proteins
2800-3020	CH_3, CH_2, CH	Stretching	Lipids, proteins, other

2.5. Surface-Enhanced Raman Scattering (SERS) Traceable Delivery

2.5.1. The SERS Developments

In the year 1974, scientists observed that adsorbed pyridine on a roughened silver electrode has remarkable sensitivity of Raman spectroscopy, and this is the first published record of surface-enhanced Raman scattering (SERS)[101]. However, the reason of this SERS phenomenon was not sure for years. Until 1977, the first correct interpretation of this SERS phenomenon was proposed as an electric field enhancement effect [102]. At the beginning, SERS technology was applied by limited amount scientists from electrochemistry and Raman spectroscopy, small research community with sufficient knowledge of optics and lasers. Then time comes to the late of 20th century in 1997, the observation of single-molecule or single-nanoparticle SERS[103, 104] contributes a lot to the boom of SERS used in various disciplines chemistry, physics, materials science, surface science, nanoscience, especially life science.

Based on rapidly developing nanotechnology, surface preparation and modification techniques, scientists have capabilities to control the material, size, and shape of a nanostructured surface or nanoparticle to form the SERS hot spot, which is the dominated factor of SERS phenomenon. Since then, SERS has been recognized as a competitive analytical method as conventional fluorescence, as the strength of SERS spectrum was not inferior to that of fluorescence one. Unlike fluorescence which has problems such as rapid photo-bleaching properties of fluorescent agents and the background interruptions from auto-fluorescence of cells, SERS method, which is similar to Raman technique, is more photo-stable and the Raman scattering signals are not influenced by the auto-fluorescence interruptions of cell background.[96]

2.5.2. Two Enhancement Mechanisms of SERS

Although an overwhelming majority of researches and studies have been carried out and a great many concepts and disciplines between light, molecules and nanoscale metal have been formed to establish the SERS theory and technique, until now the consensus understanding of SERS has been still failed to achieved. Two common accepted explanations of enhancement are electromagnetic and chemical enhancement mechanism[105-107]. The compounds adsorbed on roughened metal surfaces can trigger electromagnetic and physical enhancement, due to the excitation of Plasmon on the localized surface. When excite the localized surface plasmon resonance (LSPR) of a nanostructured or nanoparticle noble metallic structures surface, the local electromagnetic field is enhanced. As the strength of Raman scattering is proportional to the magnitude of the incident electromagnetic field, electromagnetic enhancement is one reason for SERS phenomenon. Surface-Enhanced Raman scattering (SERS) is equal to high molecular specificity of Raman spectroscopy plus metal nanostructures supporting localized surface plasmon resonances plus high sensitivity.

Towards chemical enhancement mechanism, the atomic clusters on rough metal surfaced and the molecules adsorption on the surface can form active chemical sites and excite localized electronic resonances or metal-to-adsorbate charge-transfer resonances, which also contributes to Raman scattering signal enhancements. Moreover, the electromagnetic enhancement is regarded as the major contribution, while the chemical one is acted as the minor contribution. When the distance of two near nanoparticles is close enough (<1nm), the electromagnetic field strength can significantly increase, which can possibly rocket the intensity of SERS signal to approximately 10^{9-11} times higher than normal Raman one. In addition, the

electromagnetic enhancement is regarded as the major contribution and the chemical one is acted as the minor contribution.

2.5.3. Single Molecule SERS

SERS tracing demonstrate high sensitivity and resolution features, as the strengths of original Raman peak can be theoretically enhanced to 8-11 orders of magnitude by SERS[108-110]. Enhancement of fingerprint Raman signals, which are 10-100 times narrower than fluorescence[111], can materialise the navigation pathway of a single molecule from samples, cells, or even intracellular compartments. The high sensitivity of detecting a single molecule has transferred SERS form a surface phenomenon to an emerging analytical approach for life and biological science researches on the interaction between drugs and body activities and the occurrence and development of diseases. In addition, Raman spectroscopy is a real-time characterization of molecular structures based on the polarizability of samples, and it can be processed in aqueous conditions, as high polarity water is a very weak Raman scatterer and strong infrared absorber.[95] SERS analytical technologies are superior for biological based research fields like drug/gene delivery.

2.5.4. SERS Tags and Reporters

When the distance of two near metallic nanoparticles are close enough (<1nm), the electromagnetic field strength can significantly increase and caused the SERS enhancement, which can rocket the Raman signal. These metallic nanostructures could be silver, gold, copper as well as platinum[112]. Among those metallic materials, only gold can be utilized for living cell SERS studies[113-115]. The most common metallic nanostructure is nanoscale sphere. However, other structures such as nanorods[116-120], nanoflowers[121-124] and nanostars[125-127] have also been reported as SERS tags. Those

probes can be directly linked to the sample molecule or be applied together with the sensing analyte. For no analyte available cases, the metallic nanoparticles are usually aggregated with SERS reporters to realize SERS imaging. The common SERS reporters are 4-mercaptobenzoic acid[119, 128, 129], 4-mercaptopyridine[124] and 4-aminothiophenol[130], to name but a few. In addition, outer-layer coatings such as silica[117] or polymer[131] can improve stability and biocompatibility of SERS tags and reporters.

2.6. Summary

The common analytical technique of tracing drug/gene delivery is the fluorescence based evaluation approach. Although the detecting and analyzing technologies are almost mature, there still existing certain inevitable issues. The fluorescent agents have rapid photo-bleaching properties, so that the fluorescence trace is far away from nondestructive method. Moreover, the auto-fluorescence of cells can get rise to background interruptions during detecting procedure. The overlap of fluorescence spectra is hardly distinguished. On the contrary, Raman labels are more photo-stable and the Raman signals are easier to separate, as Raman spectra is finger-printed. In addition, Raman analysis can operate in aqueous condition, as the high polar water is a very weak Raman scatterer and strong Infrared absorber. Raman related technologies are superior for biological based characterizations. The significant disadvantage of Raman is the low inherent intensity. In that case, surface enhanced Raman scattering (SERS) technology is proposed to address that problem. Currently, very few research is related to using SERS technology to trace drug/gene delivery. That rise my interests on designing functional composite nanocarriers for traceable drug delivery, especially

based on SERS technology.

Nanoscale drug/gene delivery systems have been regarded as great platforms for modern cancer therapy. After a series of functionalization, these systems are given capabilities to widely distribute in nature and safe to human beings, obtain efficient cellular uptake, control time-release dosage of drug/gene delivery and target specific areas of the body. Although nanoscale drug/gene delivery systems have a large majority of types including organic and inorganic nanomaterials, this thesis only focus on inorganic based silica and graphitic carbon nitride (g-C_3N_4) nanoscale delivery systems. This is because that simple and facile silica synthesis method is mature enough to obtain high biocompatibility, high stability for mechanical and thermal changes, high biocompatibility, low fabrication cost and time-saving silica nanoparticles. It is crucial to explore the feasibility of novel SERS traceable delivery systems on easy-obtained platforms. In addition, the reason of choosing g-C_3N_4 is because of the SERS-active properties of g-C_3N_4 materials, which avoids further artificially functionalized SERS reporters.

The researches in this thesis is aimed to fabricate novel inorganic silica and g-C_3N_4 nanocarriers conducted as delivery vehicles of anticancer drugs/genes to improve the therapeutic efficiency and reduce the side effects of hard-to-cure human diseases like cancers. In the meanwhile, SERS analytical techniques conducted by a high sensitive confocal Raman Spectroscopy are employed to trace the delivery profiles of the controllable synthesized systems to get background-noise-free SERS mapping images.

2.7. References

[1]   X. Zhang, F. Li, S. Guo, X. Chen, X. Wang, J. Li, Y. Gan, *Biomaterials* **2014,**

35, 3650.

[2]   F. Qiu, D. Wang, Q. Zhu, L. Zhu, G. Tong, Y. Lu, D. Yan, X. Zhu, *Biomacromolecules* **2014,** *15*, 1355.

[3]   F. Meng, R. Cheng, C. Deng, Z. Zhong, *Materials Today* **2012,** *15*, 436.

[4]   Y. Wang, P. Brown, Y. Xia, *Nat Mater* **2011,** *10*, 482.

[5]   C. E. Ashley, E. C. Carnes, G. K. Phillips, D. Padilla, P. N. Durfee, P. A. Brown, T. N. Hanna, J. Liu, B. Phillips, M. B. Carter, N. J. Carroll, X. Jiang, D. R. Dunphy, C. L. Willman, D. N. Petsev, D. G. Evans, A. N. Parikh, B. Chackerian, W. Wharton, D. S. Peabody, C. J. Brinker, **2011,** *10*, 389.

[6]   D. Peer, J. M. Karp, S. Hong, O. C. Farokhzad, R. Margalit, R. Langer, **2007,** *2*, 751.

[7]   M. E. Davis, Z. Chen, D. M. Shin, *Nat Rev Drug Discov* **2008,** *7*, 771.

[8]   F. Tang, L. Li, D. Chen, *Advanced Materials* **2012,** *24*, 1504.

[9]   Z. Wang, G. Liu, H. Zheng, X. Chen, *Biotechnology Advances* **2014,** *32*, 831.

[10]   Q. He, J. Shi, *Adv Mater* **2014,** *26*, 391.

[11]   Y. Gao, J. Xie, H. Chen, S. Gu, R. Zhao, J. Shao, L. Jia, *Biotechnology Advances* **2014,** *32*, 761.

[12]   C. Argyo, V. Weiss, C. Bräuchle, T. Bein, *Chemistry of Materials* **2014,** *26*, 435.

[13]   Z. Teng, X. Su, Y. Zheng, J. Sun, G. Chen, C. Tian, J. Wang, H. Li, Y. Zhao, G. Lu, *Chemistry of Materials* **2013,** *25*, 98.

[14]   X. Fang, X. Zhao, W. Fang, C. Chen, N. Zheng, *Nanoscale* **2013,** *5*, 2205.

[15]   X. Du, J. He, *Nanoscale* **2011,** *3*, 3984.

[16]   W. Stöber, A. Fink, E. Bohn, *Journal of Colloid and Interface Science* **1968,** *26*, 62.

[17]   C. T. Kresge, M. E. Leonowicz, W. J. Roth, J. C. Vartuli, J. S. Beck, *Nature* **1992,** *359*, 710.

[18]   F. Caruso, R. A. Caruso, H. Möhwald, *Science* **1998,** *282*, 1111.

[19]   Y. Wan, S.-H. Yu, *The Journal of Physical Chemistry C* **2008,** *112*, 3641.

[20] G. Zhang, Y. Yu, X. Chen, Y. Han, Y. Di, B. Yang, F. Xiao, J. Shen, *Journal of Colloid and Interface Science* **2003**, *263*, 467.

[21] J. L. Vivero-Escoto, Slowing, II, B. G. Trewyn, V. S. Lin, *Small* **2010**, *6*, 1952.

[22] Z. Teng, Y. Han, J. Li, F. Yan, W. Yang, *Microporous and Mesoporous Materials* **2010**, *127*, 67.

[23] Z.-Z. Li, L.-X. Wen, L. Shao, J.-F. Chen, *Journal of Controlled Release* **2004**, *98*, 245.

[24] X. Fang, X. Zhao, W. Fang, C. Chen, N. Zheng, *Nanoscale* **2013**, *5*, 2205.

[25] Y. Zhu, E. Kockrick, T. Ikoma, N. Hanagata, S. Kaskel, *Chemistry of Materials* **2009**, *21*, 2547.

[26] Y. Zhu, T. Ikoma, N. Hanagata, S. Kaskel, *Small* **2010**, *6*, 471.

[27] L. Tan, D. Chen, H. Liu, F. Tang, *Adv Mater* **2010**, *22*, 4885.

[28] Y. Wang, F. Wang, B. Chen, H. Xu, D. Shi, *Chemical Communications* **2011**, *47*, 10350.

[29] S. Yang, X. Zhou, P. Yuan, M. Yu, S. Xie, J. Zou, G. Q. Lu, C. Yu, *Angewandte Chemie International Edition* **2007**, *46*, 8579.

[30] B. Yang, K. Edler, C. Guo, H. Liu, *Microporous and Mesoporous Materials* **2010**, *131*, 21.

[31] Y. Zhang, M. Yu, L. Zhou, X. Zhou, Q. Zhao, H. Li, C. Yu, *Chemistry of Materials* **2008**, *20*, 6238.

[32] D. Shen, J. Yang, X. Li, L. Zhou, R. Zhang, W. Li, L. Chen, R. Wang, F. Zhang, D. Zhao, *Nano Letters* **2014**, *14*, 923.

[33] X. Du, S. Z. Qiao, *Small* **2015**, *11*, 392.

[34] M. Vallet-Regi, A. Rámila, R. P. del Real, J. Pérez-Pariente, *Chemistry of Materials* **2001**, *13*, 308.

[35] Z. Li, J. C. Barnes, A. Bosoy, J. F. Stoddart, J. I. Zink, *Chemical Society Reviews* **2012**, *41*, 2590.

[36] P. Yang, S. Gai, J. Lin, *Chemical Society Reviews* **2012**, *41*, 3679.

[37] X. Du, J. He, *Nanoscale* **2012**, *4*, 852.

[38]   A. J. Paula, L. A. Montoro, A. G. Filho, O. L. Alves, *Chemical communications* **2012,** *48*, 591.

[39]   J. Mendez, A. Monteagudo, K. Griebenow, *Bioconjugate chemistry* **2012,** *23*, 698.

[40]   R. Liu, P. Liao, J. Liu, P. Feng, *Langmuir : the ACS journal of surfaces and colloids* **2011,** *27*, 3095.

[41]   X. Li, Y. Chen, M. Wang, Y. Ma, W. Xia, H. Gu, *Biomaterials* **2013,** *34*, 1391.

[42]   H.-L. Liu, S. P. Ko, J.-H. Wu, M.-H. Jung, J. H. Min, J. H. Lee, B. H. An, Y. K. Kim, *Journal of Magnetism and Magnetic Materials* **2007,** *310*, e815.

[43]   M. Kar, P. S. Vijayakumar, B. L. Prasad, S. Sen Gupta, *Langmuir : the ACS journal of surfaces and colloids* **2010,** *26*, 5772.

[44]   D. E. Meyer, B. C. Shin, G. A. Kong, M. W. Dewhirst, A. Chilkoti, *Journal of Controlled Release* **2001,** *74*, 213.

[45]   H. Jin, K. A. Kang, Application Of Novel Metal Nanoparticles As Optical/Thermal Agents In Optical Mammography And Hyperthermic Treatment For Breast Cancer. In *Oxygen Transport to Tissue XXVIII*, Maguire, D. J.; Bruley, D. F.; Harrison, D. K., Eds. Springer US: Boston, MA, 2008; pp 45.

[46]   Y.-L. Zhao, Z. Li, S. Kabehie, Y. Y. Botros, J. F. Stoddart, J. I. Zink, *Journal of the American Chemical Society* **2010,** *132*, 13016.

[47]   R. Liu, Y. Zhang, X. Zhao, A. Agarwal, L. J. Mueller, P. Feng, *Journal of the American Chemical Society* **2010,** *132*, 1500.

[48]   S. Aryal, J. J. Grailer, S. Pilla, D. A. Steeber, S. Gong, *Journal of Materials Chemistry* **2009,** *19*, 7879.

[49]   N. Rapoport, *Progress in Polymer Science* **2007,** *32*, 962.

[50]   D. Niu, Z. Liu, Y. Li, X. Luo, J. Zhang, J. Gong, J. Shi, *Advanced materials* **2014,** *26*, 4947.

[51]   Z. Li, K. Dong, S. Huang, E. Ju, Z. Liu, M. Yin, J. Ren, X. Qu, *Advanced Functional Materials* **2014,** n/a.

[52] A. Ito, M. Shinkai, H. Honda, T. Kobayashi, *Journal of Bioscience and Bioengineering* **2005**, *100*, 1.

[53] M. Zelzer, S. J. Todd, A. R. Hirst, T. O. McDonald, R. V. Ulijn, *Biomaterials Science* **2013**, *1*, 11.

[54] F. Wang, G. M. Pauletti, J. Wang, J. Zhang, R. C. Ewing, Y. Wang, D. Shi, *Advanced materials* **2013**, *25*, 3485.

[55] A. Schlossbauer, S. Warncke, P. M. E. Gramlich, J. Kecht, A. Manetto, T. Carell, T. Bein, *Angewandte Chemie International Edition* **2010**, *49*, 4734.

[56] M. de Jong, W. A. P. Breeman, D. J. Kwekkeboom, R. Valkema, E. P. Krenning, *Accounts of chemical research* **2009**, *42*, 873.

[57] C. C. Kumar, *Current Drug Targets* **2003**, *4*, 123.

[58] S. Ganta, H. Devalapally, A. Shahiwala, M. Amiji, *Journal of controlled release : official journal of the Controlled Release Society* **2008**, *126*, 187.

[59] J. Wang, Z. Hu, J. Xu, Y. Zhao, *NPG Asia Mater* **2014**, *6*, e84.

[60] L. Feng, Z. Liu, *Nanomedicine* **2011**, *6*, 317.

[61] E. Nakamura, H. Isobe, *The Chemical Record* **2010**, *10*, 260.

[62] Z. Liu, S. Tabakman, K. Welsher, H. Dai, *Nano. Res.* **2009**, *2*, 85.

[63] Y. Zhang, S. F. Ali, E. Dervishi, Y. Xu, Z. Li, D. Casciano, A. S. Biris, *ACS Nano* **2010**, *4*, 3181.

[64] J. Guerra, M. A. Herrero, E. Vazquez, *Rsc Advances* **2014**, *4*, 27315.

[65] P. Cherukuri, S. M. Bachilo, S. H. Litovsky, R. B. Weisman, *Journal of the American Chemical Society* **2004**, *126*, 15638.

[66] K. Yang, L. Feng, X. Shi, Z. Liu, *Chemical Society reviews* **2013**, *42*, 530.

[67] Y. Chen, P. Xu, Z. Shu, M. Wu, L. Wang, S. Zhang, Y. Zheng, H. Chen, J. Wang, Y. Li, J. Shi, *Advanced Functional Materials* **2014**, n/a.

[68] D. He, X. He, K. Wang, Z. Zou, X. Yang, X. Li, *Langmuir : the ACS journal of surfaces and colloids* **2014**, *30*, 7182.

[69] Z. Liu, J. T. Robinson, X. Sun, H. Dai, *Journal of the American Chemical Society* **2008**, *130*, 10876.

[70] X. Sun, Z. Liu, K. Welsher, J. T. Robinson, A. Goodwin, S. Zaric, H. Dai, *Nano Res* **2008,** *1*, 203.

[71] Y. Chen, C. Tan, H. Zhang, L. Wang, *Chemical Society Reviews* **2015,** *44*, 2681.

[72] D. Chimene, D. L. Alge, A. K. Gaharwar, *Advanced Materials* **2015,** *27*, 7261.

[73] R. Kurapati, K. Kostarelos, M. Prato, A. Bianco, *Advanced Materials* **2016,** *28*, 6052.

[74] C. E. Ashley, E. C. Carnes, G. K. Phillips, D. Padilla, P. N. Durfee, P. A. Brown, T. N. Hanna, J. Liu, B. Phillips, M. B. Carter, N. J. Carroll, X. Jiang, D. R. Dunphy, C. L. Willman, D. N. Petsev, D. G. Evans, A. N. Parikh, B. Chackerian, W. Wharton, D. S. Peabody, C. J. Brinker, *Nat Mater* **2011,** *10*, 389.

[75] H.-W. Yang, Y.-J. Lu, K.-J. Lin, S.-C. Hsu, C.-Y. Huang, S.-H. She, H.-L. Liu, C.-W. Lin, M.-C. Xiao, S.-P. Wey, P.-Y. Chen, T.-C. Yen, K.-C. Wei, C.-C. M. Ma, *Biomaterials* **2013,** *34*, 7204.

[76] B. Tian, C. Wang, S. Zhang, L. Feng, Z. Liu, *ACS Nano* **2011,** *5*, 7000.

[77] L.-S. Lin, Z.-X. Cong, J. Li, K.-M. Ke, S.-S. Guo, H.-H. Yang, G.-N. Chen, *Journal of Materials Chemistry B* **2014,** *2*, 1031.

[78] C. Liu, Z. Chen, Z. Wang, W. Li, E. Ju, Z. Yan, Z. Liu, J. Ren, X. Qu, *Nanoscale* **2016,** *8*, 12570.

[79] Y. Zhao, C. J. Wang, W. Gao, B. Li, Q. Wang, L. Zheng, M. Wei, D. G. Evans, X. Duan, D. O'Hare, *Journal of Materials Chemistry B* **2013,** *1*, 5988.

[80] H. Wang, X. Yang, W. Shao, S. Chen, J. Xie, X. Zhang, J. Wang, Y. Xie, *Journal of the American Chemical Society* **2015,** *137*, 11376.

[81] Z. Sun, H. Xie, S. Tang, X.-F. Yu, Z. Guo, J. Shao, H. Zhang, H. Huang, H. Wang, P. K. Chu, *Angewandte Chemie International Edition* **2015,** *54*, 11581.

[82] C. G. Liu, X. T. Wu, X. F. Li, X. G. Zhang, *Rsc Advances* **2014,** *4*, 62492.

[83] X. Zhang, X. Xie, H. Wang, J. Zhang, B. Pan, Y. Xie, *J Am Chem Soc* **2013,** *135*, 18.

[84] D. Lee, B. Lee, K. H. Park, H. J. Ryu, S. Jeon, S. H. Hong, *Nano Letters* **2015,** *15*, 1238.

[85] X. Wang, N. D. Mansukhani, L. M. Guiney, Z. Ji, C. H. Chang, M. Wang, Y.-P. Liao, T.-B. Song, B. Sun, R. Li, T. Xia, M. C. Hersam, A. E. Nel, *Small* **2015,** *11*, 5079.

[86] S. Xu, D. Li, P. Wu, *Advanced Functional Materials* **2015,** *25*, 1127.

[87] X. Dong, F. Cheng, *Journal of Materials Chemistry A* **2015,** *3*, 23642.

[88] X. Zhang, H. Wang, H. Wang, Q. Zhang, J. Xie, Y. Tian, J. Wang, Y. Xie, *Advanced Materials* **2014,** *26*, 4438.

[89] S. M. Janib, A. S. Moses, J. A. MacKay, *Advanced drug delivery reviews* **2010,** *62*, 1052.

[90] J. Wang, P. Mi, G. Lin, Y. X. J. Wáng, G. Liu, X. Chen, *Advanced Drug Delivery Reviews* **2016,** *104*, 44.

[91] B. Fahrenkrog, U. Aebi, *Nat Rev Mol Cell Biol* **2003,** *4*, 757.

[92] P. Debbage, W. Jaschke, *Histochemistry and Cell Biology* **2008,** *130*, 845.

[93] K. Park, S. Lee, E. Kang, K. Kim, K. Choi, I. C. Kwon, *Advanced Functional Materials* **2009,** *19*, 1553.

[94] J. M. Yoo, J. H. Kang, B. H. Hong, *Chemical Society Reviews* **2015,** *44*, 4835.

[95] J. T. Krug Ii, G. D. Wang, S. R. Emory, S. Nie, *J. Am. Chem. Soc.* **1999,** *121*, 9208.

[96] S. Keren, C. Zavaleta, Z. Cheng, A. de la Zerda, O. Gheysens, S. S. Gambhir, *Proceedings of the National Academy of Sciences of the United States of America* **2008,** *105*, 5844.

[97] H.-J. van Manen, Y. M. Kraan, D. Roos, C. Otto, *Proceedings of the National Academy of Sciences of the United States of America* **2005,** *102*, 10159.

[98] I. W. Schie, L. Alber, A. L. Gryshuk, J. W. Chan, *Analyst* **2014,** *139*, 2726.

[99] B. Kann, H. L. Offerhaus, M. Windbergs, C. Otto, *Advanced Drug Delivery Reviews* **2015,** *89*, 71.

[100] M. Kerker, *Accounts of Chemical Research* **1984,** *17*, 271.

[101] M. Fleischmann, P. J. Hendra, A. J. McQuillan, *Chemical Physics Letters* **1974,** *26*, 163.

[102] D. L. Jeanmaire, R. P. Van Duyne, *Journal of Electroanalytical Chemistry and Interfacial Electrochemistry* **1977,** *84*, 1.

[103] S. Nie, S. R. Emory, *Science* **1997,** *275*, 1102.

[104] K. Kneipp, Y. Wang, H. Kneipp, L. T. Perelman, I. Itzkan, R. R. Dasari, M. S. Feld, *Physical Review Letters* **1997,** *78*, 1667.

[105] X. M. Qian, S. M. Nie, *Chemical Society reviews* **2008,** *37*, 912.

[106] M. Fan, G. F. Andrade, A. G. Brolo, *Analytica chimica acta* **2011,** *693*, 7.

[107] X. Gong, Y. Bao, C. Qiu, C. Jiang, *Chemical communications* **2012,** *48*, 7003.

[108] X. M. Qian, S. M. Nie, *Chemical Society Reviews* **2008,** *37*, 912.

[109] M. Fan, G. F. S. Andrade, A. G. Brolo, *Analytica Chimica Acta* **2011,** *693*, 7.

[110] X. Gong, Y. Bao, C. Qiu, C. Jiang, *Chemical Communications* **2012,** *48*, 7003.

[111] M. Vendrell, K. K. Maiti, K. Dhaliwal, Y.-T. Chang, *Trends in Biotechnology* **2013,** *31*, 249.

[112] K. A. Stoerzinger, J. Y. Lin, T. W. Odom, *Chemical science* **2011,** *2*, 1435.

[113] J. Kneipp, H. Kneipp, M. McLaughlin, D. Brown, K. Kneipp, *Nano Letters* **2006,** *6*, 2225.

[114] K. Kneipp, A. S. Haka, H. Kneipp, K. Badizadegan, N. Yoshizawa, C. Boone, K. E. Shafer-Peltier, J. T. Motz, R. R. Dasari, M. S. Feld, *Appl. Spectrosc.* **2002,** *56*, 150.

[115] A. Sujith, T. Itoh, H. Abe, A. A. Anas, K. Yoshida, V. Biju, M. Ishikawa, *Applied Physics Letters* **2008,** *92*, 103901.

[116] S. Zong, Z. Wang, H. Chen, D. Zhu, P. Chen, Y. Cui, *Ieee Transactions on Nanobioscience* **2014,** *13*, 55.

[117] S. Zong, Z. Wang, H. Chen, J. Yang, Y. Cui, *Analytical chemistry* **2013,** *85*, 2223.

[118] D. Lin, T. Qin, Y. Wang, X. Sun, L. Chen, *Acs Applied Materials & Interfaces* **2014,** *6*, 1320.

[119] L. Xiao, S. Harihar, D. R. Welch, A. Zhou, *Analytica Chimica Acta* **2014,** *843*, 73.

[120] Z. Wang, S. Zong, W. Li, C. Wang, S. Xu, H. Chen, Y. Cui, *Journal of the American Chemical Society* **2012**, *134*, 2993.

[121] J. Xie, Q. Zhang, J. Y. Lee, D. I. C. Wang, *ACS Nano* **2008**, *2*, 2473.

[122] J. Fang, S. Du, S. Lebedkin, Z. Li, R. Kruk, M. Kappes, H. Hahn, *Nano Letters* **2010**, *10*, 5006.

[123] Z. Wang, J. Zhang, J. M. Ekman, P. J. A. Kenis, Y. Lu, *Nano Letters* **2010**, *10*, 1886.

[124] Q. Li, Y. Jiang, R. Han, X. Zhong, S. Liu, Z.-Y. Li, Y. Sha, D. Xu, *Small* **2013**, *9*, 927.

[125] A. M. Fales, H. Yuan, T. Vo-Dinh, *Langmuir* **2011**, *27*, 12186.

[126] A. M. Fales, H. Yuan, T. Vo-Dinh, *Molecular Pharmaceutics* **2013**, *10*, 2291.

[127] H. Yuan, A. M. Fales, C. G. Khoury, J. Liu, T. Vo-Dinh, *Journal of Raman spectroscopy : JRS* **2013**, *44*, 234.

[128] A. Michota, J. Bukowska, *Journal of Raman Spectroscopy* **2003**, *34*, 21.

[129] L. Wei, B. Jin, S. Dai, *The Journal of Physical Chemistry C* **2012**, *116*, 17174.

[130] M. K. Gregas, F. Yan, J. Scaffidi, H.-N. Wang, T. Vo-Dinh, *Nanomedicine: Nanotechnology, Biology and Medicine* **2011**, *7*, 115.

[131] L. Jiang, J. Qian, F. Cai, S. He, *Analytical and Bioanalytical Chemistry* **2011**, *400*, 2793.

Chapter 3 The Feasibility of Constructing Surface-Enhanced Raman Scattering (SERS) Traceable Drug Delivery Systems

3.1. Introduction, Significance and Commentary

Smart drug delivery systems (DDSs) have been constructed for non-destructive surface-enhanced Raman scattering (SERS) tracing and targeted cancer-cell cytotoxicities. SERS tracing based on the designed DDSs have higher sensitivities and resolutions than conventional fluorescence tracking, which provide the DDSs with great autonomy and potentials to discover the dynamic processes of general drug delivery performances in living cells. The highlights of this work include:

1. Smart SERS traceable DDSs system

The covalent pH-cleavable linkage between drugs and carriers provides the DDSs with targeted cytotoxicities of cancer cells. Our work finds that this "smart" function can work independently and harmoniously with SERS tracing.

2. Small gold nanoparticles based SERS used in tracing DDSs

The 5-10 nm gold nanoparticles aggregate on the surface of silica nanoparticles to form hot spots, in which Raman signals can be greatly enhanced. It has seldom employed for DDSs tracing.

3. Wide range feasibility and higher sensitivities of SERS trace

The feasibility of SERS trace is validated by the fluorescence approach. New approach might be widely used to evaluate other general drugs without fluorescence. As SERS trace has higher sensitivities than fluorescence ones, it could effectively replace the latter in tracing.

4. Excellent stabilities of gold-silica integration to guarantee SERS trace

The integrated gold nanoparticles can still be observed after a series of complex modifications which are important for SERS trace. The excellent and strong integration ensures the designed DDS can be traced by SERS during delivery processes in certain severe environments, especially blood circulations.

3.2. Smart SERS Traceable Drug Delivery System

This section is included in the thesis as it appears as a paper published by L. Liu, Y. Tang, S. Sheng, F. Kleitz and S. Z. Qiao. Smart Surface Enhanced Raman Scattering Traceable Drug Delivery System, Nanoscale, **2016**, 8, 12803-12811.

Statement of Authorship

Title of Paper	Smart Surface Enhanced Raman Scattering Traceable Drug Delivery System
Publication Status	☑ Published ☐ Accepted for Publication ☐ Submitted for Publication ☐ Unpublished and Unsubmitted work written in manuscript style
Publication Details	First published on 30th May 2016 DOI: 10.1039/C6NR03869G

Principal Author

Name of Principal Author (Candidate)	Lei Liu (First Author)
Contribution to the Paper	Research plan, material synthesis, material characterization, material performance assessment, manuscript drafting.
Overall percentage (%)	80%
Certification:	This paper reports on original research I conducted during the period of my Higher Degree by Research candidature and is not subject to any obligations or contractual agreements with a third party that would constrain its inclusion in this thesis. I am the primary author of this paper.
Signature	Date 29/11/2017

Co-Author Contributions
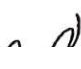
By signing the Statement of Authorship, each author certifies that:

i. the candidate's stated contribution to the publication is accurate (as detailed above);

ii. permission is granted for the candidate in include the publication in the thesis; and

iii. the sum of all co-author contributions is equal to 100% less the candidate's stated contribution.

Name of Co-Author	Prof. Yonghong Tang
Contribution to the Paper	Assistance with material characterization
Signature	Date 28-11-2017

Name of Co-Author	Prof. Sheng Dai (Corresponding Authors)
Contribution to the Paper	Design of the project, assistance with research plan, material synthesis and manuscript revision
Signature	Date 28/11/2017

Name of Co-Author	Prof. Freddy Kleitz
Contribution to the Paper	Assistance with manuscript revision
Signature		Date	28/11/2017

Name of Co-Author	Prof. Shi Zhang Qiao (Corresponding Authors)
Contribution to the Paper	Design of the project, organization of the research and supervision, manuscript revision
Signature		Date	17/1/2018

Please cut and paste additional co-author panels here as required.

CrossMark
*click for updates

Smart surface-enhanced Raman scattering traceable drug delivery systems†

Lei Liu,[a] Yonghong Tang,[b] Sheng Dai,*[a] Freddy Kleitz[c] and Shi Zhang Qiao*[a]

A novel smart nanoparticle-based system has been developed for tracking intracellular drug delivery through surface-enhanced Raman scattering (SERS). This new drug delivery system (DDS) shows targeted cytotoxicity towards cancer cells via pH-cleavable covalent carboxylic hydrazone links and the SERS tracing capability based on gold@silica nanocarriers. Doxorubicin, as a model anticancer drug, was employed to compare SERS with conventional fluorescence tracing approaches. It is evident that SERS demonstrates higher sensitivity and resolution, revealing intracellular details, as the strengths of the original Raman signals can be amplified by SERS. Importantly, non-destructive SERS will provide the designed DDS with great autonomy and potential to study the dynamic procedures of non-fluorescent drug delivery into living cells.

Introduction

Most of the small-molecule anticancer drugs have potent chemotherapeutic characteristics, but their therapeutic efficacy is often limited by severe side effects caused by systemic toxicity and rapid resistance or aggregation issues caused by poor solubility, low stability and unsuitable pharmacokinetic profiles as well as the lack of selectivity.[1,2] For the improvement of the practical and clinical performances of drugs to combat human cancer, nanoparticle-based drug delivery systems (DDSs) have, over the recent years, drawn worldwide attention in the field of anticancer research. For example, impressive efforts have been made to construct physical feature-controlled,[3,4] highly biocompatible[5] and multifunctional[6] DDSs. Among those nanoparticles applied for drug delivery, silica nanoparticles (SNs) possess the excellent properties of high stability against chemical, mechanical and thermal changes, as well as high biocompatibility and straightforward surface functionalisation,[7–9] thus they are considered as an ideal platform for functional DDSs. Unlike physical adsorption and diffusion, which may lead to premature, burst drug release and ultimately severe side effects, smart covalent linkages between the drug and carrier, especially carboxylic hydrazone links,[10–12] could bring effective impacts on sustainable drug release and reduce side effects, making the development of such smart DDSs a high priority.

When it comes to tracking the intracellular performance of DDSs, the conventional widely implemented approach is fluorescence evaluation. However, it has certain inevitable limitations. In general, DDSs require artificial labelling, which might change physicochemical properties, uptake pathways and pharmacological effects of the loaded drugs. Moreover, photo-bleaching fluorophores and the fluorescent background interruptions from cells tend to limit long-term tracing.[13] As the characteristic peak in the fluorescence spectra is very broad, it raises the difficulty of distinguishing overlapping spectra from multi-fluorescence labelled tracing systems.[14] Conversely, surface-enhanced Raman scattering (SERS) has been introduced into life science research,[14–16] where these fluorescence barriers could be mitigated and crossed. The results of SERS tracing demonstrate high sensitivity and resolution features, as the strength of the original Raman peak can be theoretically enhanced to 8–11 orders of magnitude by SERS.[17–19] Enhancement of fingerprint Raman signals (10–100 times narrower than fluorescence[14]) can materialise the navigation pathway of a single molecule from samples, cells, or even intracellular compartments. However, only limited work has been performed in the area of SERS-tracking drug delivery. For instance, single metal nanoparticles with a silica coating of size larger than 100 nm were reported,[20] as this size of noble metal particles is acceptable for SERS tracing. However, clusters of small (5–10 nm) metal nanoparticles can also form hot spots in the junctions between them to enhance Raman signals,[16] which could make them suitable to replace larger single nanoparticles as the most effective SERS traceable agents. However, to date, DDSs based on small metal nanoparticle-induced SERS have remained largely unexplored.

[a]School of Chemical Engineering, The University of Adelaide, Adelaide, SA 5005, Australia. E-mail: s.qiao@adelaide.edu.au, s.dai@adelaide.edu.au
[b]Centre for Nano Scale Science and Technology, School of Computer Science, Engineering, and Mathematics, Flinders University, Adelaide, SA 5042, Australia
[c]Department of Chemistry and Centre de Recherche sur les Matériaux Avancés (CERMA), Université Laval, Quebec City, QC G1 V 0A6, Canada
†Electronic supplementary information (ESI) available. See DOI: 10.1039/c6nr03869g

Herein, a smart SERS traceable drug delivery system (DDS) has been constructed, in which the drug-carrier linkages are pH-cleavable. Silica nanoparticles (SNs) are viewed as the framework, and small exposed gold particles with SERS reporters are settled on SNs. Owing to the covalent pH-cleavable drug-carrier links, the chosen anticancer drug (DOX) will remain conjugated into the DDS to avoid premature and uncontrolled drug leakage in healthy cell regions. As shown in Scheme 1, when delivered to cancer cells, the chemical links of the DDS will be cleaved by the more acidic surroundings of the cancer cells, and DOX will be dissociated and released into the cells to perform its pharmacological purpose. Therefore, this smart DDS design will offer targeted cytotoxicity while being efficiently tracked by SERS.

Experimental

Chemicals

Fetal bovine serum (FBS), Dulbecco's modified eagle medium (DMEM), pH = 7.4 phosphate buffered saline (PBS), antibiotic-antimycotic (Anti-anti, 100×), 0.25% (w/v) trypsin–0.03% (w/v) ethylenediaminetetraacetic acid (EDTA) solution, 3-(4,5-dimethylthiazol-2-yl)-2,5-diphenyltetrazolium bromide (MTT) and LIVE/DEAD® viability/cytotoxicity kit (calcein-AM/ethidium homodimer-1) were purchased from Life Technologies Australia Pty Ltd. Doxorubicin hydrochloride (DOX), which is selected as a model drug for cancer therapy, was purchased from Beijing Huafeng United Technology Co Ltd. Gold(III) chloride trihydrate ($HAuCl_4 \cdot 3H_2O$) and aqueous ammonia (NH_4OH, 25%) were purchased from Chem-Supply Australia Pty Ltd. Sodium borohydride ($NaBH_4$), N-hydroxysuccinimide (NHS), N-(3-dimethylaminopropyl)-N′-ethylcarbodiimide

hydrochloride (EDC), 4-mercaptobenzoic acid (4-MBA), tetraethyl orthosilicate (TEOS, ≥98%), (3-aminopropyl)triethoxysilane (APTES, ≥98%), sodium citrate (Na_3Ct), trifluoroacetic acid (TFA), N,N-dimethylformamide (DMF), tert-butyl carbazate (Boc-NHNH$_2$), succinic anhydride, dimethyl sulfoxide (DMSO) and other chemicals were purchased from Sigma Aldrich. All materials were of analytical grade and used as received without further purification. Millipore water was obtained from a three-stage Millipore Mill-Q plus 185 purified cation system (Academic) with a resistivity higher than 18.2 MΩ cm.

Characterisation

Scanning electron microscopy (SEM) observations were carried out on an FEI Quanta 450 FEG environmental emission scanning electron microscope operated at 10 kV. A 5 nm platinum layer coating by ion sputtering was required for each specimen before SEM observation. For obtaining transmission electron microscopy (TEM) images, an FEI Tecnai G2 Spirit transmission electron microscope at an acceleration voltage of 120 kV was employed. Fourier transform infrared (FTIR) spectra were recorded at room temperature on a Thermo Scientific NICOLET 6700 FTIR spectrometer. The hydrodynamic sizes and zeta-potentials of different products dispersed in deionized water were determined at room temperature by using a Malvern Zeta-sizer Nano ZS (Malvern Inst. Ltd, UK) equipment. The concentration of particles in water was kept at 0.1 ± 0.05 mg mL^{-1} for particle size analysis, while the zeta potential results were calculated based on the statistical analysis of 10 parallel runs. The pH values were measured by using a pH meter (EL20, METTLER TOLEDO). UV-Vis absorption spectra were recorded on a UV-2600 spectrophotometer (Shimadzu Corporation). X-ray diffraction (XRD) patterns were obtained on a powder X-ray diffractometer at 40 kV and 15 mA using Co-Kα radiation (Miniflex, Rigaku). In addition, an Axis Ultra (Kratos Analytical, UK) XPS spectrometer equipped with an Al Kα source (1486.6 eV) was used for X-ray photoelectron spectrum (XPS) collection. Fluorescence excitation and emission images were obtained on a ZEISS Axio Vert. A1 inverted microscope equipped with 488 nm and 530 nm lasers. A HORIBA Lab RAM HR Evolution equipped with a 785 nm laser was employed for obtaining Raman spectra and SERS mapping images.

Synthetic procedures of SN-NH$_2$

The SN-NH$_2$ were fabricated by a modified direct Stöber approach.[21] In a typical synthesis run, TEOS (2.3 mL) was quickly added to a mixed solution of 25% aqueous ammonia (3.0 mL), deionized water (1.0 mL), and ethanol (60 mL). The magnetic stirring rate is ca. 800–1000 rpm. The mixture was stirred at 40 °C for 4 h, and then 0.1 mL APTES was added into the system. After 800–1000 rpm stirring for another 2 h at 40 °C and washing with ethanol, the aminated silica nanospheres, labelled as SN-NH$_2$, were obtained.

Synthetic procedures of Au–SN-NH$_2$

The gold nanoparticles were prepared by the $NaBH_4$ and Na_3Ct reduction method.[22,23] 1.0% $HAuCl_4 \cdot 3H_2O$ (0.1 mL) and de-
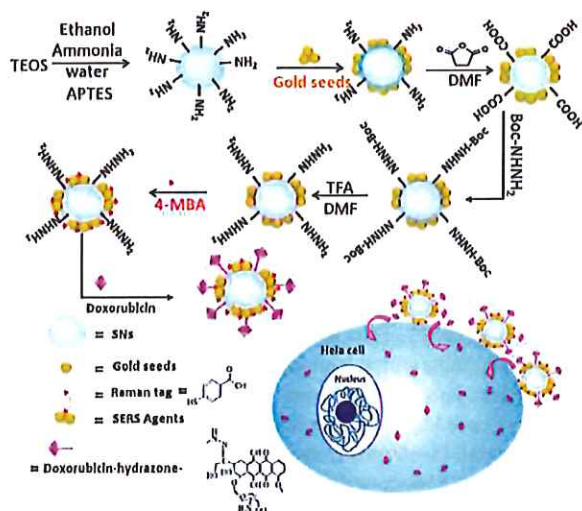
Scheme 1 Schematic diagram representing the synthesis of doxorubicin-conjugated SERS nanocomposites and the pathway of intracellular drug release.

ionized water (9 mL) were stirred for 1 min with 800–1000 rpm stirring rate at room temperature, and then 38.8 mM Na_3Ct (0.2 mL) was added into the system. After adding 0.075% $NaBH_4$ (0.1 mL), gold nanoparticles of *ca.* 5–10 nm were synthesised. Subsequently, these gold nanoparticles were attached to the $SN-NH_2$ with a gold nanoparticle-to-SN molar ratio of 4, under 30 min sonication in deionized water. The resulting Au–$SN-NH_2$ nanoparticles were centrifuged and then washed with ethanol, and the final precipitates were dried in an oven at 60 °C for 24 h.

Synthetic procedures of 4-MBA–Au–SN-NHNH₂

As illustrated in Scheme 1, 100 mg Au–$SN-NH_2$ particles were dispersed in DMF (12 mL) by ultrasonic treatment. 900 mg succinic anhydride was dissolved in DMF and then added into the prepared Au–$SN-NH_2$ suspension. After stirring for 6 h at room temperature, the products were centrifuged, washed with ethanol and water and dried to obtain Au–SN-COOH powder. Then, Au–SN-COOH particles were added in DMF (20 mL), and stirred with 54 mg EDC and 32 mg NHS for 1 h at room temperature, before 37 mg Boc-$NHNH_2$ were finally added into the system. The mixture was further stirred at room temperature for another 24 h. The products were centrifuged, washed with ethanol and water and dried to yield Au–SN-NHNH-Boc. To remove the protective Boc group, Au–SN-NHNH-Boc particles were dispersed in a mixture of DMF (10 mL) and TFA (5 mL). The system was stirred at room temperature for 24 h, before the final products Au–SN-$NHNH_2$ were centrifuged, washed with ethanol and dried in an oven at 60 °C. 1 mM 4-MBA was added to the Au–SN-$NHNH_2$ aqueous suspensions with a molar ratio of 1 : 100. After stirring for 24 h at room temperature, the SERS tag 4-MBA was integrated onto the gold nanoparticles. The 4-MBA–Au–SN-$NHNH_2$ nanocarriers were centrifuged and then washed several times with ethanol to remove any unreacted 4-MBA, and the final precipitates were dried in an oven at 60 °C for 24 h.

DOX conjugation and *in vitro* release

Regarding doxorubicin conjugation (Scheme 1), 1.0 mg of dried 4-MBA–Au–SN-$NHNH_2$ nanocarriers was added into *ca.* 0.5 mg mL^{-1} DOX/PBS solution, and stirred at 1000 rpm at room temperature for 24 h in a dark environment. After washing with ethanol 3 times, the final 4-MBA–Au–SN–hydrazone–DOX products were collected by centrifugation, washed with standard pH 7.4 PBS and dried in an oven at 60 °C for 24 h. The supernatant of the initial DOX/PBS solution and all the washing supernatants were collected for the evaluation of the DOX conjugation efficiency. The corresponding DOX doses were estimated by using 480 nm UV-vis adsorption values and a standard DOX calibration curve.

The release profiles of DOX from 4-MBA–Au–SN–hydrazone–DOX were evaluated independently in three PBS media with different pH values 5.0, 6.0 and 7.4. The pH value of each system was adjusted using acetate buffer and PBS, and measured by using a pH meter. For each release investigation, 5 mg DOX-conjugated particles were added into the buffer solution (5 mL), and continuously stirred with a rate of 100 rpm at 37 °C under dark conditions. 1 mL of release medium was removed at selected time intervals. The supernatant was centrifuged for drug release analysis, and the residual parts together with an identical amount of fresh buffer solution were put back into the system. The released amounts of DOX were analysed by using 480 nm UV-vis adsorption values and a standard DOX calibration curve.

Cytotoxicity studies

The cell viability results obtained by MTT assays against human cervical cancer HeLa cells and human embryonic kidney HEK 293 cells were used to investigate the cytotoxicities of the fabricated nanocarriers 4-MBA–Au–SN-$NHNH_2$ before and after DOX conjugation. Both HeLa and HEK293 cells were incubated in cell culture medium (DMEM, 10% FBS and 1× Anti-anti) at 37 °C in a 5% CO_2 humid environment. For MTT assays, cells were seeded into a 96-well plate at a density of 5×10^4 cells per mL, and incubated for 24 h in cell culture medium (0.1 mL). Subsequently, an identical volume of cell culture medium (0.1 mL) containing different particles (nanocarriers, DOX-conjugated products and free DOX) was replaced by the previous medium and further incubated for 24 h. Then, 0.5 mg mL^{-1} MTT (0.01 mL) was added to each well, and after incubation for 4 h, DMSO (0.15 mL) was used to replace the medium and dissolve formazan crystals. The MTT assays were conducted in quadruplicate for each sample, and the final absorbance of formazan crystals was measured by using an ELx808 Absorbance Microplate Reader (Biotek, USA) at a wavelength of 595 nm.

The cytotoxicity results of 4-MBA–Au–SN–hydrazone–DOX were further confirmed by using fluorescence LIVE/DEAD® viability/cytotoxicity studies. HEK293 and HeLa cells were added into a 24-well plate at 5×10^4 cells per mL seeding density, and incubated in cell culture medium (1 mL) for 24 h. Later, 0.2 mg mL^{-1} DOX-conjugated products in cell culture medium (1 mL) were replaced and incubated for another 24 h. After removal of the medium and PBS washing, the cells were harvested by using EDTA and resuspended in PBS solution. 0.4 mL LIVE/DEAD® viability/cytotoxicity kit (2 µM calcein-AM and 4 µM ethidium homodimer-1) was added in a dark environment, and then incubated for 30 min. The cells were gently washed with PBS to remove excessive dyes. The final cytotoxicity results were checked by using images obtained with a fluorescence microscope.

SERS tracking of 4-MBA–Au–SN–hydrazone–DOX

HeLa cells were seeded at a concentration of 2×10^5 cells per mL with 2 mL cell culture medium per well into a 6-well plate with 22 mm cover-glass slides inside, and incubated for 24 h at 37 °C under 5% CO_2. The fresh medium (2 mL) containing 0.4 mg DOX-conjugated products was replaced and incubated for another 4 h. Subsequently, the glass substrate with cells and DOX conjugated products was collected after three times of gentle washing with PBS. The Raman study was conducted with a 785 nm laser and 100× objectives. The area is 30 ×

30 μm with a resolution of 961 data points for mapping. The acquisition time for each data point is 1 s.

Flow cytometry analysis of 4-MBA–Au–SN–hydrazone–DOX

In terms of flow cytometry analysis, 0.2 mg mL^{-1} DDSs were dispersed in cell culture medium (DMEM with 10% FBS and 1% PS). HeLa cells were added into a 24-well plate at 2×10^4 cells per mL seeding density, and incubated in 1 mL cell culture medium for 24 h at 37 °C under 5% CO_2. Fresh media (1 mL) containing 0.2 mg mL^{-1} 4-MBA–Au–SN–hydrazone–DOX was incubated for different time periods. The cells were harvested by the digestion of EDTA solution, and gently washed with PBS twice. With a 200–600 cells per second flow rate, ca. 1×10^4 cells were analysed by using a FACS Calibur flow cytometer (Becton Dickinson). The testing result of healthy HeLa cells was selected as a negative control, and the red fluorescence intensities of DOX were directly measured by cytometry. The data were analysed using Cell Quest 3.3 software, while one-color flow cytometry was used to evaluate cellular uptake.

Results and discussion

Characterization of the smart drug delivery system

The 4-MBA–Au–SN–hydrazone–DOX smart DDS was prepared following the procedure illustrated in Scheme 1. The amino-functionalized silica nanoparticles (SN–NH_2) were synthesized in one pot by a modified Stöber method.[21] The scanning electron microscopy image (SEM, Fig. 1a) and transmission electron microscopy image (TEM, Fig. 1b) demonstrate that SNs are uniform nanospheres with an average particle diameter of ca. 80–100 nm. The size results are further verified from

Fig. 1 Electron microscopy images. (a) SEM, (b) TEM images of SN–NH_2, (c) gold nanoparticles, and (d) Au–SN–$NHNH_2$.

dynamic light scattering (DLS) measurements (Table S1† and Fig. 2a), where the average hydrodynamic diameter of SN–NH_2 is 91 nm with an average zeta potential of +18.3 mV. In the FTIR spectra (Fig. S1†) of SN–NH_2, the typical silica Si–O–Si asymmetric stretching, Si–OH and Si–O symmetric stretching vibrations can be observed at around 1066, 945 and 795 cm^{-1}, respectively.[24] The –OH stretching vibration at approximately 1635 cm^{-1} may be the deformation band of physically absorbed H_2O. The 3357 cm^{-1} peak is the signature of N–H stretching vibrations, and N–H bending bands appear around 1500 cm^{-1}. The existence of amino groups is crucial for further anchoring of gold nanoparticles.

Gold nanoparticles (Au NPs) were synthesised by sodium borohydride reduction and sodium citrate stabilization.[22,24] Sphere-like Au NPs with an average 5–10 nm diameter can be observed in the high resolution TEM images (Fig. 1c). The hydrodynamic size of Au NPs measured by DLS (Table S1† and Fig. 2a) is around 12 nm with a negative average zeta potential of −33.1 mV, which is in line with the TEM size results. As displayed in the enlarged image (inset of Fig. 1c), the average distance of the lattice fringes is approximately 0.23 nm, which is evidence of the presence of the (111) crystallographic planes.[24,25] As shown in Fig. S2a,† the surface plasmon resonance (SPR) of the synthesised Au NPs, collected by UV-vis measurements, can be clearly visible as a peak at 520 nm in the UV-vis spectra. According to the reference experimental data,[23,26] this SPR peak fits the behaviour of spherical Au NPs with the particle size range of 5–10 nm. In addition to the theoretical calculation, the measured ratio of the absorbance at the SPR peak to the absorbance at 450 nm is 1.20, and according to the size in dependence of the particle diameter data of spherical Au NPs,[23] the particle diameter can be estimated as 4–5 nm.

Au–SN–NH_2 was formed by attachment of Au NPs on SN–NH_2 based on selective bonding between gold atoms and the amine groups.[27] From the DLS data (Table S1† and Fig. 2a), the hydrodynamic diameter of Au–SN–NH_2 is around 103 nm with an average zeta potential of +9.4 mV. The decrease of zeta potential from SN–NH_2 to Au–SN–NH_2 may be attributed to the presence of Au NPs linked to SN–NH_2. Furthermore, in Fig. S2a,† the SPR peak shifts from 520 nm to 535 nm, which might be due to the Au NP aggregation on the silica particle surfaces. According to the wide-angle XRD pattern (Fig. 2b) and standard pattern JCPDS card no. 04-0784, the first broad diffraction pattern from the 2θ range 10 to 30° can be assigned to the amorphous silica component, while the peaks at 2θ = 38.18°, 44.39°, 64.58° and 77.55° correspond to the (111), (200), (220) and (311) planes of Au NPs, respectively. The estimated average size of Au NPs calculated using the Scherrer formula is about 5.5 nm, in accordance with the full width at half maximum of the intense (111) reflection of Au NPs. Furthermore, the FTIR spectroscopy result (Fig. S1†) of Au–SN–NH_2 is almost identical to SN–NH_2, with signals at 1066, 945 and 795 cm^{-1} confirming the presence of silica, while 3357 and 1500 cm^{-1} are evidence of the amino groups.
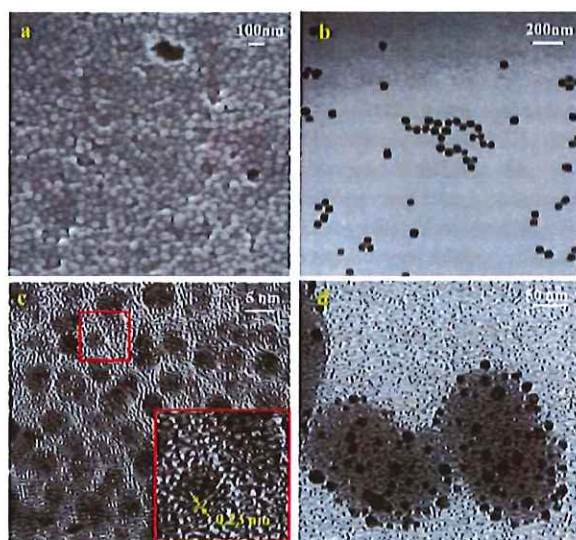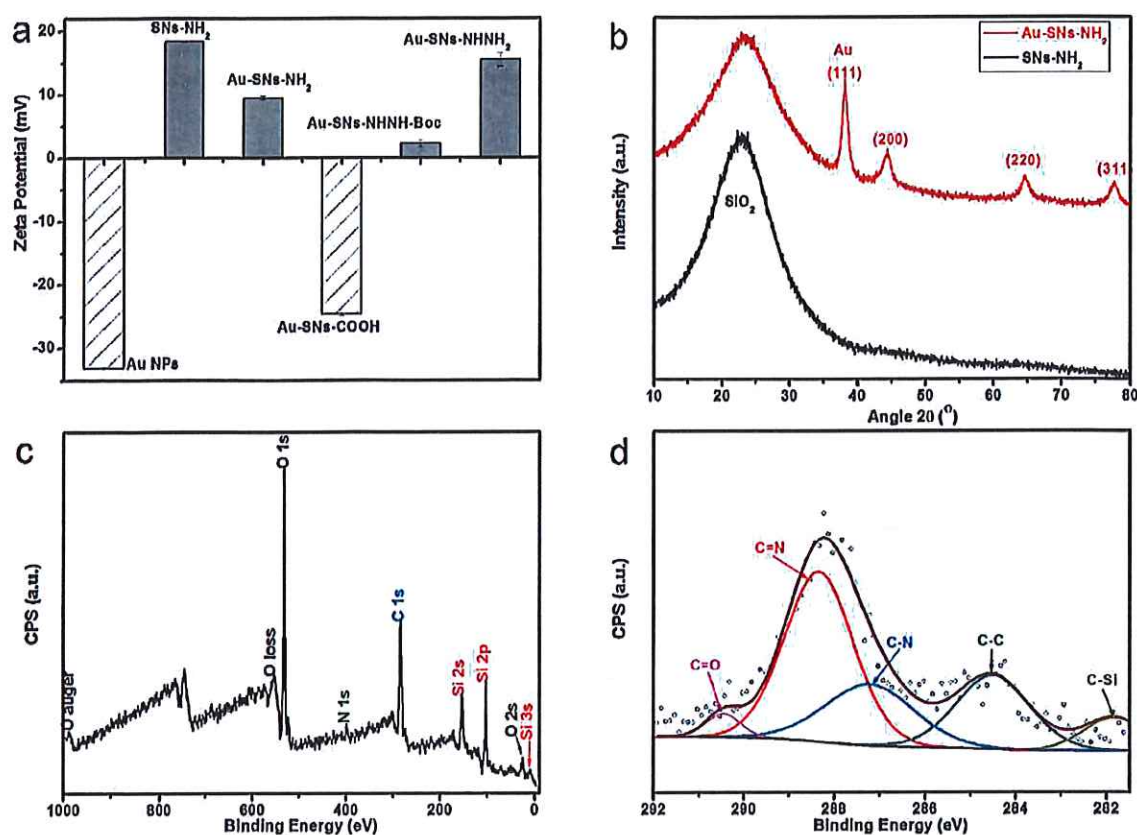
Fig. 2 (a) Zeta potentials of different products at different synthesis stages, (b) XRD patterns of SN-NH$_2$ and Au–SN-NH$_2$, (c) XPS spectra of DOX-conjugated composites, and (d) the enlarged C 1s region.

Towards surface modification, two intermediate products, Au–SN-COOH and Au–SN-NHNH-Boc, were synthesised. From the DLS data (Table S1† and Fig. 2a), the hydrodynamic size of Au–SN-COOH is about 115 nm with an average zeta potential of −24.6 mV, while Au–SNsNHNH-Boc with a hydrodynamic size of ca. 174 nm has an average zeta potential of +2.3 mV. The negative–positive change of the zeta potentials could be attributed to the conversion of surface groups from –COOH to –NHNH-Boc. From the FTIR spectra (Fig. S1†), the peak at 1720 cm^{-1} is attributed to the symmetric stretching of –C=O, which confirms the presence of carboxyl groups, while the 1657 cm^{-1} peak indicates the existence of –NH–C=O stretching vibrations.

After removing Boc groups using TFA,[10] Au–SN-NHNH$_2$ was obtained. From the TEM image (Fig. 1d), the average particle size is about 150–170 nm, combined with the ~5–10 nm dark spots recognized as Au NPs. By further characterization by DLS (Table S1† and Fig. 2a), the hydrodynamic size of Au–SN-NHNH$_2$ is about 167 nm with an average zeta potential of +15.4 mV. This size of nanocarriers is believed to be superior for drug delivery applications not only for favouring the enhanced permeability and retention effects (EPR), but also for limiting non-targeted cellular uptake and undesired cyto-

toxicity.[28] The zeta potential increase from Au–SN-NHNH-Boc to Au–SN-NHNH$_2$ is attributed to the surface hydrazine groups on Au–SN-NHNH$_2$. The presence of hydrazine groups was also confirmed by FTIR. The 3357 cm^{-1} N–H stretching and 1500 cm^{-1} N–H bending vibration peaks can be clearly identified in Fig. S1.†

4-MBA–Au–SN–hydrazone–DOX DDSs were created by attaching 4-MBA as SERS tags,[29,30] and DOX conjugation was realized via a pH-cleavable carboxylic hydrazone linkage.[10,31]

In the FTIR spectra (Fig. S1†), the peak at 1734 cm^{-1} is attributed to the –C=O symmetric stretching vibrations from 4-MBA. The signal at 1657 cm^{-1} represents the hydrazone bonds, which arise from the reaction between hydrazine and the carbonyl groups from DOX. Characteristic peaks at 1540, 1467 and 1412 cm^{-1} belong to the skeleton vibrations of the ring of DOX,[32] which proves the presence of DOX on the DDS particles. The 2850 and 2917 cm^{-1} bands are attributed to C–H vibrations.

The DOX conjugation was also verified by testing the fluorescence of the well-washed DDS composites. From Fig. S2b,† the 503 nm excitation and 557 nm emission peaks are evidence of DOX linked to DDSs. Moreover, the X-ray photoelectron spectroscopy results shown in Fig. 2c illustrate that

DDSs contain C, O, N and Si elements. However, the presence of S from 4-MBA and Au element could not be detected plausibly because of their too low surface contents. The enlarged C 1s region (Fig. 2d) demonstrates the presence of C–Si, C–C,

C–N, C=N, and C=O groups. These high resolution XPS results confirm the occurrence of hydrazone bonds, which is also proof of the DOX–hydrazone conjugations.

SERS effective enhancement factor

The Raman spectra of bulk 4-MBA and 4-MBA–Au–SN-NHNH$_2$ (Fig. 3) are compared to estimate the SERS effective enhancement factor (EEF).

For 4-MBA, the Raman peaks at 1099 cm^{-1} and 1595 cm^{-1} are attributed to ν8a and ν12 aromatic ring vibrations of 4-MBA.[29] However, for 4-MBA–Au–SN-NHNH$_2$, these two peaks shift to 1078 cm^{-1} and 1580 cm^{-1}, respectively. The occurrence of such blue shifts confirms the interaction between 4-MBA and Au NPs. The EEF can be estimated based on the calculation result using the 1078 cm^{-1} band with the following equation:

$$EEF = \frac{I_{SERS}N_{bulk}}{I_{bulk}N_{SERS}}$$

where I_{SERS} and I_{bulk} are the intensities of SERS and bulk spectra at the 1078 cm^{-1} band, and $\frac{N_{bulk}}{N_{SERS}}$ is the molar ratio

Fig. 3 Raman spectra of bulk 4-MBA and the SERS spectra of 4-MBA–Au–SN-NHNH$_2$.
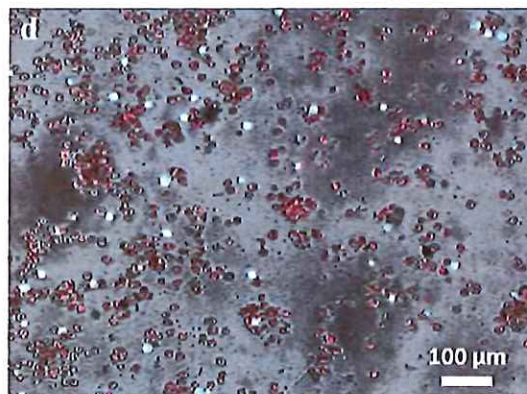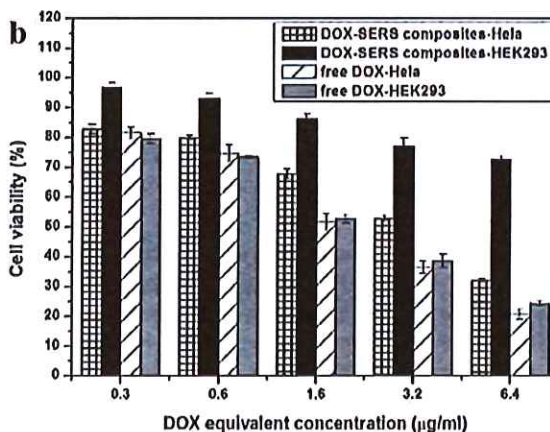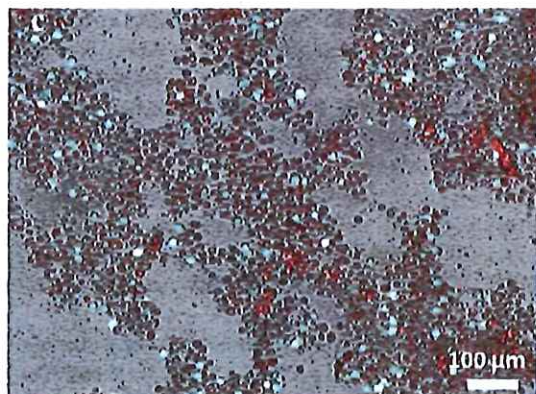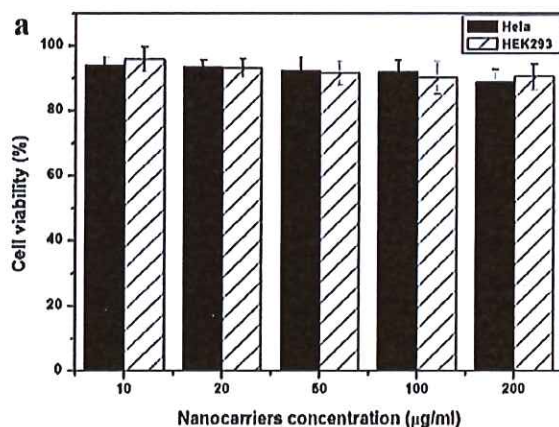
Fig. 4 Cytotoxicity data of (a) SERS traceable nanocarriers, (b) DDSs and free DOX, and LIVE/DEAD® analysis of 24 h DDS incubation of (c) HEK293, and (d) HeLa cells.

between the bulk and SERS sample.[29,33] Thus, the EEF of 4-MBA–Au–SN-NHNH$_2$ is approximately 1.7×10^5.

Biocompatibility and targeted cytotoxicity of DDSs

The biocompatibility of the nanocarriers (4-MBA–Au–SN-NHNH$_2$) and the cytotoxicity of the DDS, and free DOX as a reference, were determined and compared for the HeLa (cancer) and HEK293 (healthy) cell lines. As shown in Fig. 4a, the nanocarriers demonstrate great biocompatibility in both cell lines. After 24 h of incubation at 37 °C under 5% CO$_2$, cell viabilities remained above 85%, for particle concentrations below 200 μg ml^{-1}.

For the DDS particles and free DOX, the results, shown in Fig. 4b, reveal that cell viabilities are decreasing with the increasing DOX equivalent concentration in both cell lines. For free DOX, no distinct differences of cytotoxicity are observed between the cell lines. However, for DDSs, the tolerability of HEK 293 cells is much better than that of HeLa cells at high particle dosage. At 6.4 μg ml^{-1} of DOX equivalent concentration, the cell viability of HEK 293 is around 70%, which is higher than the 30% in HeLa. This difference could be attributed to the acidic-cleavage of the carboxylic hydrazone bond existing between DOX and nanocarriers, which accelerated the release of DOX from the nanocarriers in the cancer cells. The difference in DDS cytotoxicities between cancer and healthy cells evidences the feasibility of a pH-smart DDS. Furthermore, the SERS tracing agents seem to exert little influence on cellular selections. In addition, DDS cytotoxicities in both HEK 293 and HeLa cell lines were investigated by LIVE/DEAD® viability/cytotoxicity measurements. For this, 6.4 μg ml^{-1} DOX equivalent concentration of DDS particles was incubated for 24 h in both the cell lines. Living cells were stained fluorescent green with Calcein AM, while the dead cells were stained red with ethidium homodimer-1. Fig. 4c and d show the merged optical-fluorescence images of the HEK293 and HeLa cells. For HEK293, the amount of fluorescent green live cells is more than red ones with an estimated cell viability of 70%. While for the HeLa cells, the amount of green living cells is lower than that of the red dead cells, where the cell viability might be estimated to be about 25%.

Cellular uptake using SERS tracing

The cellular uptake performances of the DDS in the HeLa cell lines were analysed by SERS mapping and compared with the fluorescence method. The DDS-treated cells were placed on a microscopy glass substrate and directly observed by Raman microscopy.

Fig. 5a shows the bright field image of the HeLa cells with a 30 × 30 μm mapping area (red square marked). This area demonstrates a single-cell, and its enlarged image with 2
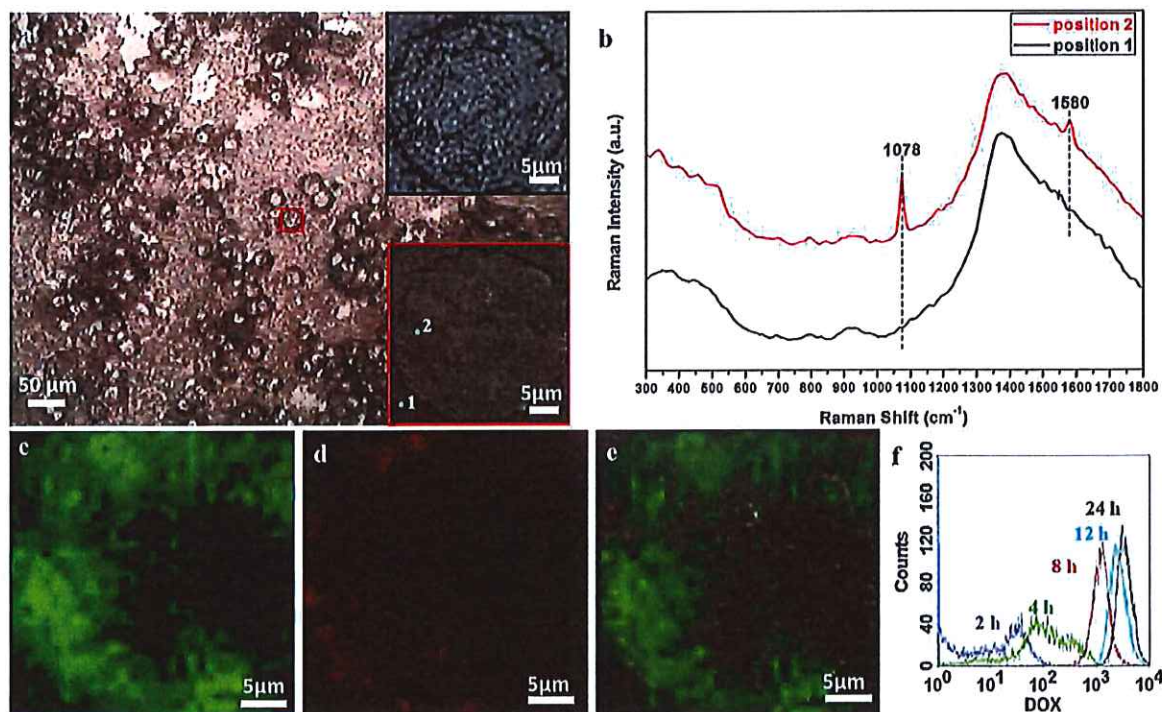
Fig. 5 (a) Optical image of HeLa cells with a red rectangle mapping area, optical images of the enlarged mapping area from the upper inset of (a) fluorescence, and the lower inset of (a) Raman microscopy with two selected positions 1 and 2, (b) Raman spectra of selected positions, (c) SERS mapping image, (d) fluorescence image, (e) merged optical-fluorescence-SERS images, and (h) flow cytometry results with different DOX incubation times.

selected positions is shown in the lower inset of Fig. 5a. These testing positions 1 and 2 are selected to represent the signal obtained from the substrate and that from the cell, respectively. Their corresponding SERS spectra are depicted in Fig. 5b. Although there are background fluorescence interruptions of the glass substrate around 400 and 1400 cm^{-1}, the narrow 1078 and 1580 cm^{-1} SERS peaks are readily distinguished. Thus, the SERS approach offers a certain competitive advantage over the fluorescence method, such as a finger-print narrow band, high sensitivity and easily distinguished signals. Fig. 5c shows the tracing image by SERS mapping, in which the intensities of the 1078 cm^{-1} band are demonstrated by the brightness of green cursors. The possibility of obtaining an SERS tracing image of DDS intracellular performances validates the feasibility of the SERS tracing method. The fluorescence tracing image of DOX (Fig. 5d) was obtained from the same sample used in SERS mapping. Also, the DOX fluorescence tracing was further checked by *in vitro* flow cytometry analysis. DOX fluorescence is tracked from different incubation time points from 2 to 24 h. As demonstrated in Fig. 5f, the DOX fluorescence intensity is proportional to the incubation time, which is indicating the cellular uptake of DOX molecules.[34] To compare the SERS and fluorescence tracing results, the fluorescence image was captured at the same position of the same sample tested, and the enlarged optical image obtained from fluorescence microscopy is shown in the upper inset of Fig. 5a. This single-cell image is identical to the optical image obtained from Raman microscopy shown in the lower inset of Fig. 5a. The merged image in Fig. 5e demonstrates the overlapping area of the optical, SERS and fluorescence images. As the fluorescence tracing result agrees well with the SERS one, efficient SERS tracing is further confirmed. Interestingly, the single-cell SERS tracing image exhibits high resolution and reveals more intracellular details than the red fluorescence one. The black area in the SERS image might demonstrate the position of the cell nucleus, where the DDS particles could not be delivered into.

Conclusions

A new smart DDS was designed through SERS-traceable nanocarriers bearing a carboxylic hydrazone-conjugated DOX anticancer agent. The SN platform contributes to the aggregation of small exposed gold nanoparticles on their surfaces, which benefits SERS tracing. The smart DDS is almost biocompatible in healthy cells, while exhibits targeted cytotoxicities in cancer cells. By choosing DOX as an anticancer model drug, intracellular uptake of DDS particles could be traced by comparing the SERS and fluorescence approaches. As SERS signals have higher sensitivities than the fluorescence ones, it could effectively replace the fluorescence method in tracing. With further consideration of the non-destructive features of SERS methods, these designed DDSs might be implemented to evaluate other general drugs without fluorescence analysis. This point is also valid for general drugs without inhibiting

cell functions. In that case, we envision that these structured nanocarriers might have the capability to unveil dynamic processes of drug delivery in living cells.

Acknowledgements

Notes and references

1 X. Zhang, F. Li, S. Guo, X. Chen, X. Wang, J. Li and Y. Gan, *Biomaterials*, 2014, 35, 3650–3665.
2 F. Qiu, D. Wang, Q. Zhu, L. Zhu, G. Tong, Y. Lu, D. Yan and X. Zhu, *Biomacromolecules*, 2014, 15, 1355–1364.
3 K. C. W. Wu and Y. Yamauchi, *J. Mater. Chem.*, 2012, 22, 1251–1256.
4 V. Malgras, Q. Ji, Y. Kamachi, T. Mori, F.-K. Shieh, K. C. W. Wu, K. Ariga and Y. Yamauchi, *Bull. Chem. Soc. Jpn.*, 2015, 88, 1171–1200.
5 H.-Y. Lian, M. Hu, C.-H. Liu, Y. Yamauchi and K. C. W. Wu, *Chem. Commun.*, 2012, 48, 5151–5153.
6 C. Argyo, V. Weiss, C. Bräuchle and T. Bein, *Chem. Mater.*, 2014, 26, 435–451.
7 X. Du, L. Xiong, S. Dai, F. Kleitz and S. Z. Qiao, *Adv. Funct. Mater.*, 2014, 24, 7627–7637.
8 Z. Teng, X. Su, Y. Zheng, J. Sun, G. Chen, C. Tian, J. Wang, H. Li, Y. Zhao and G. Lu, *Chem. Mater.*, 2013, 25, 98–105.
9 X. Fang, X. Zhao, W. Fang, C. Chen and N. Zheng, *Nanoscale*, 2013, 5, 2205–2218.
10 J. Fan, G. Fang, X. Wang, F. Zeng, Y. Xiang and S. Wu, *Nanotechnology*, 2011, 22, 455102.
11 Y. Zhang, C. Xiao, M. Li, J. Chen, J. Ding, C. He, X. Zhuang and X. Chen, *Macromol. Biosci.*, 2013, 13, 584–594.
12 C. Liu, F. Liu, L. Feng, M. Li, J. Zhang and N. Zhang, *Biomaterials*, 2013, 34, 2547–2564.
13 A. Samanta, K. K. Maiti, K.-S. Soh, X. Liao, M. Vendrell, U. S. Dinish, S.-W. Yun, R. Bhuvaneswari, H. Kim, S. Rautela, J. Chung, M. Olivo and Y.-T. Chang, *Angew. Chem., Int. Ed.*, 2011, 50, 6089–6092.
14 M. Vendrell, K. K. Maiti, K. Dhaliwal and Y.-T. Chang, *Trends Biotechnol.*, 2013, 31, 249–257.
15 S. Zeng, D. Baillargeat, H.-P. Ho and K.-T. Yong, *Chem. Soc. Rev.*, 2014, 43, 3426–3452.
16 S. Schlücker, *Angew. Chem., Int. Ed.*, 2014, 53, 4756–4795.
17 X. M. Qian and S. M. Nie, *Chem. Soc. Rev.*, 2008, 37, 912–920.
18 M. Fan, G. F. S. Andrade and A. G. Brolo, *Anal. Chim. Acta*, 2011, 693, 7–25.

19 X. Gong, Y. Bao, C. Qiu and C. Jiang, *Chem. Commun.*, 2012, 48, 7003–7018.

20 S. Zong, Z. Wang, H. Chen, J. Yang and Y. Cui, *Anal. Chem.*, 2013, 85, 2223–2230.

21 Y. Takeda, Y. Komori and H. Yoshitake, *Colloids Surf., A*, 2013, 422, 68–74.

22 C. J. Johnson, E. Dujardin, S. A. Davis, C. J. Murphy and S. Mann, *J. Mater. Chem.*, 2002, 12, 1765–1770.

23 W. Haiss, N. T. K. Thanh, J. Aveyard and D. G. Fernig, *Anal. Chem.*, 2007, 79, 4215–4221.

24 X. Du and J. He, *Nanoscale*, 2012, 4, 852–859.

25 X. Li, H. Liu, J. Yang, S. Z. Qiao and X. W. Du, *RSC Adv.*, 2014, 4, 1185–1188.

26 G. A. López-Muñoz, J. A. Pescador-Rojas, J. Ortega-Lopez, J. S. Salazar and J. A. Balderas-López, *Nanoscale Res. Lett.*, 2012, 7, 1–6.

27 S. Y. Quek, L. Venkataraman, H. J. Choi, S. G. Louie, M. S. Hybertsen and J. B. Neaton, *Nano Lett.*, 2007, 7, 3477–3482.

28 K. E. Schmalenberg, L. Frauchiger, L. Nikkhouy-Albers and K. E. Uhrich, *Biomacromolecules*, 2001, 2, 851–855.

29 L. Wei, B. Jin and S. Dai, *J. Phys. Chem. C*, 2012, 116, 17174–17181.

30 A. Michota and J. Bukowska, *J. Raman Spectrosc.*, 2003, 34, 21–25.

31 D. Li, J. Tang, C. Wei, J. Guo, S. Wang, D. Chaudhary and C. Wang, *Small*, 2012, 8, 2690–2697.

32 A. Popat, J. Liu, Q. Hu, M. Kennedy, B. Peters, G. Q. Lu and S. Z. Qiao, *Nanoscale*, 2012, 4, 970–975.

33 P. H. C. Camargo, L. Au, M. Rycenga, W. Li and Y. Xia, *Chem. Phys. Lett.*, 2010, 484, 304–308.

34 X. Du, L. Xiong, S. Dai and S. Z. Qiao, *Adv. Healthcare Mater.*, 2015, 4, 771–781.

3.3. Supplementary Information

This section is included in the thesis as supplementary information to section 3.2. It includes additional information which is not put in the main text of the published paper, but as electronic supplementary information freely accessible online.

Smart Surface Enhanced Raman Scattering Traceable Drug Delivery System

*Lei Liu[a], Yonghong Tang[b], Sheng Dai *[c], Freddy Kleitz [d], and Shi-Zhang Qiao *[a]*

[a] School of Chemical Engineering, The University of Adelaide, Adelaide, SA 5005, Australia.

[b] Centre for Nano Scale Science and Technology, School of Computer Science, Engineering, and Mathematics, Flinders University, Adelaide, SA 5042, Australia.

[c]. School of Engineering, Newcastle University, Newcastle Upon Tyne, NE1 7RU, England.

[d] Department of Chemistry and Centre de Recherche sur les Matériaux Avancés (CERMA), Université Laval, Quebec City, QC G1V 0A6, Canada.

* Address for correspondence: s.qiao@adelaide.edu.au; sheng.dai@ncl.ac.uk

Table S1. DLS data for the different products obtained from the synthesis procedure.

Sample Name	Zeta Potential (mV)	Hydrodynamic Size (nm)
Au NPs	-30.1	12
SNs-NH2	+18.4	91
Au-SNs-NH2	+9	103
SNs-Au(-COOH)	-24.6	115
SNs-Au(-NHNH-Boc)	+2.3	174
SNs-Au(-NHNH2)	+15.4	167
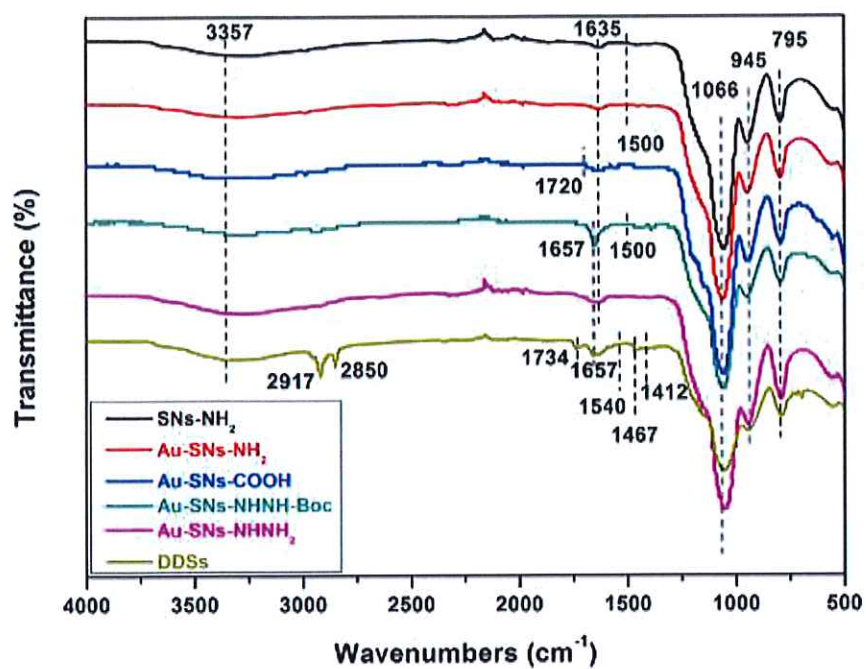
Fig. S1. FTIR spectra of the different products from the synthesis procedure.
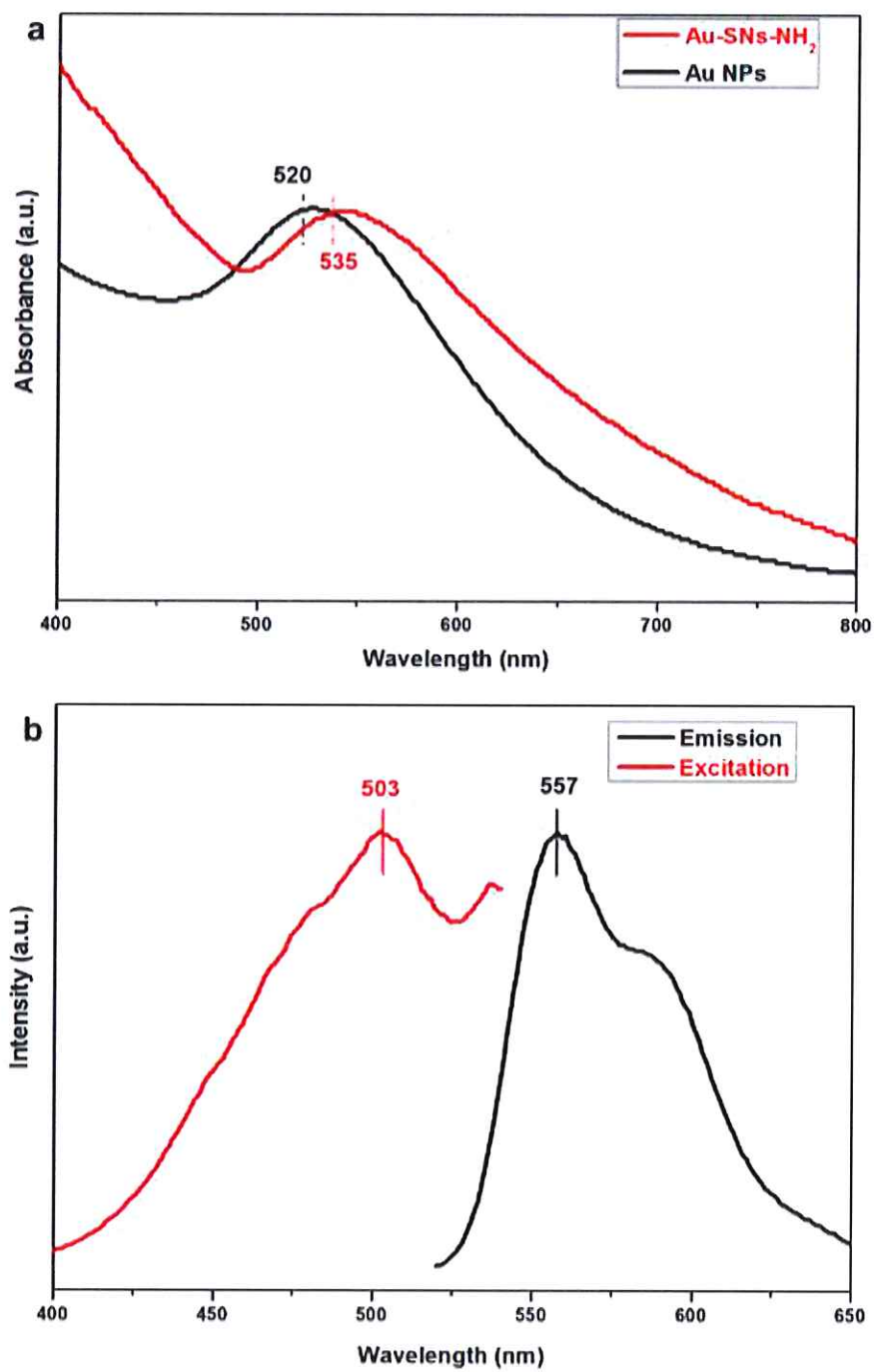
Fig. S2. a) SPR of Au NPs and Au-SNs-NH₂, b) DDS fluorescence spectra.
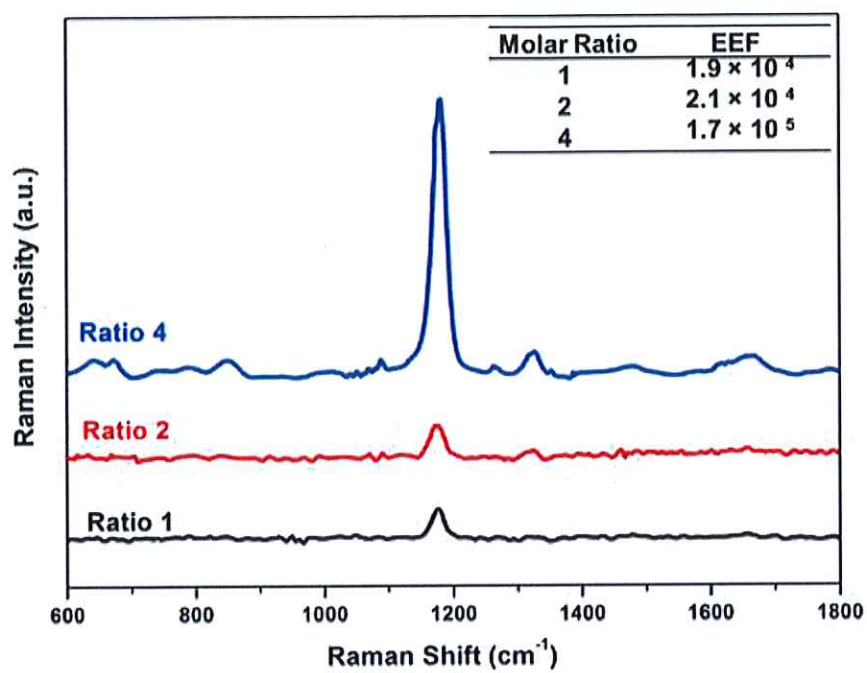
Fig. S3. EEF results of nanocarriers with different gold to silica molar ratios.
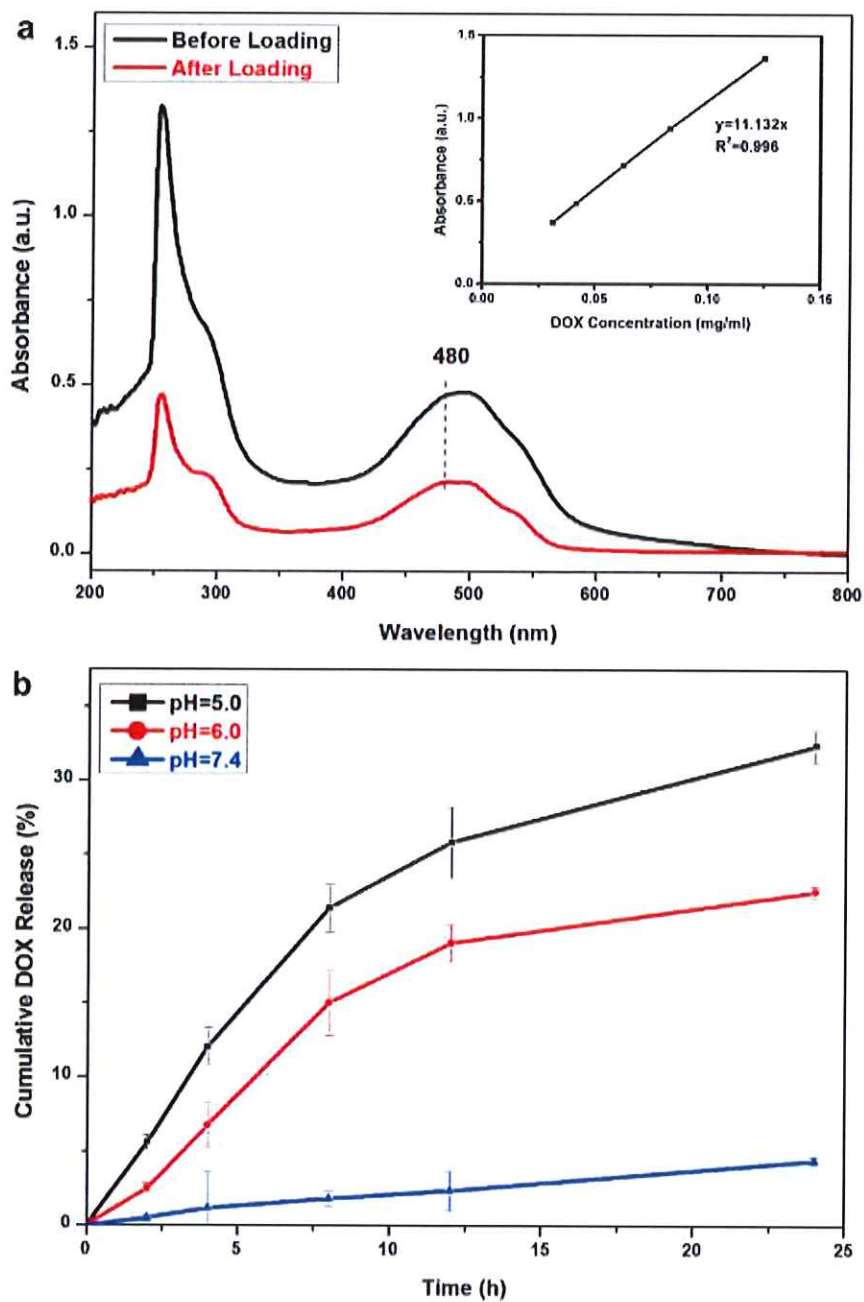
Fig. S4. a) UV-Vis absorbance data of the supernatants collected before and after DOX conjugation with inset DOX standard calibration curve, and b) DOX cumulative release profiles at different pH conditions.
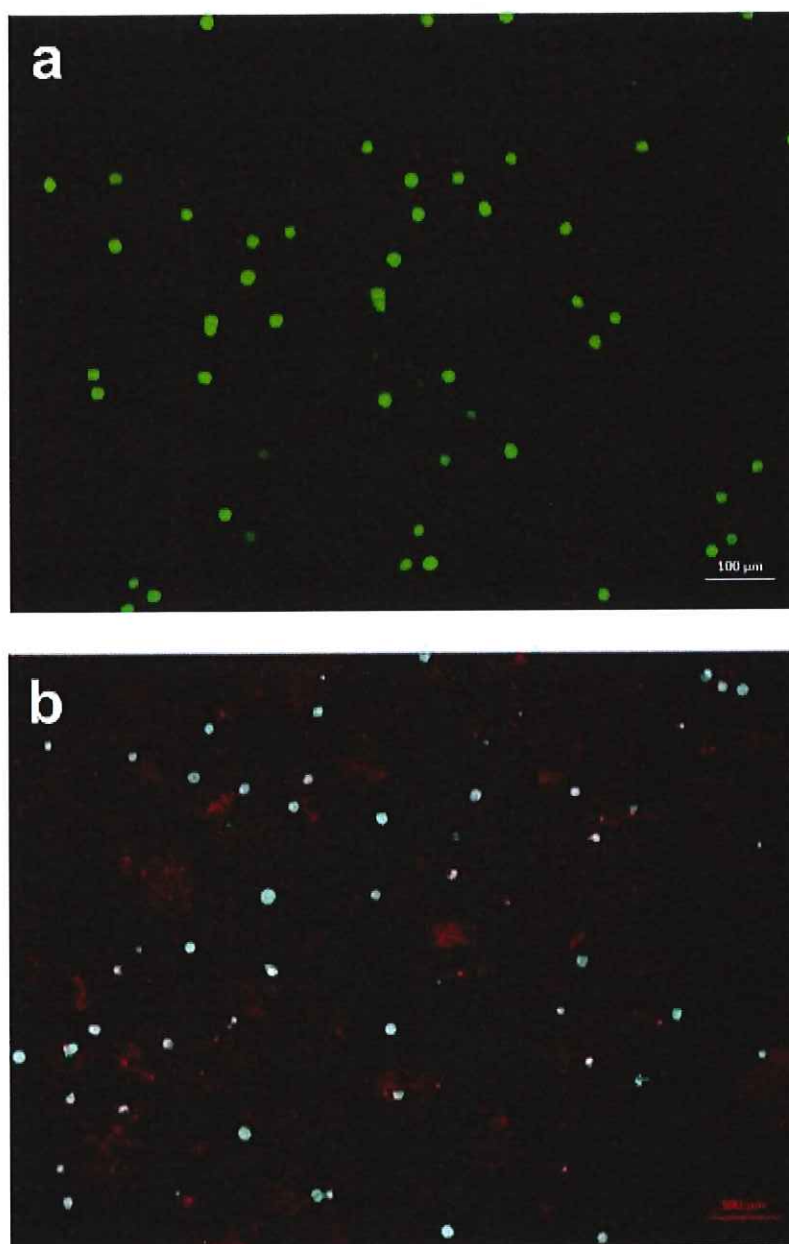
Fig. S5 The fluorescence images of LIVE/DEAD® Analysis of a) nanocarriers and b) DDSs incubated in HeLa cells for 24 h.

Chapter 4 Advanced Silica based Surface-Enhanced Raman Scattering (SERS) Traceable Gene Delivery Systems

4.1. Introduction, Significance and Commentary

A novel stellate porous silica based delivery system has been designed for SERS trace purpose. The results show that designed stellate porous silica delivery system could materialise SERS trace, and show high sensitivity and non-invasive features, which makes the constructed delivery system have considerable potentials to discover the dynamic delivery performances in living cells. The highlights of this work include:

1. Novel stellate porous silica-gold structure as SERS tag

Stellate porous silica nanoparticles with in-site reduction gold nanoparticles are demonstrated as a novel SERS tag. The morphologies and structures can be controlled with small consumptions of gold. The unique stellate porous structures make it easy for gold aggregation on silica skeleton by electrostatic and capillary adsorptions.

2. SERS trace for siRNA delivery

Most of the SERS trace applications in delivery fields is based on drug delivery, this work is designed based on gene delivery. The results prove the feasibility of SERS traceable gene(siRNA) delivery system.

4.2. Stellate Porous Silica based Surface-Enhanced Raman Scattering (SERS) Traceable Delivery Systems

This section is included in the thesis as it appears as an unpublished and unsubmitted work written in manuscript style.

4.2.1. Abstract

Currently, numerous nanocarriers have been developed for intracellular delivery, and the potential cytotoxicity of these very small inorganic nanocarriers has raise great considerations. Consequently, the intracellular trace of nanocarriers became of utmost importance for investigate the delivery performance of nanocarriers. Among different analytical techniques, surface enhanced Raman scattering (SERS) is one of the current state-of-the-art method for cell visualization and trace. In this work, a novel stellate porous silica based delivery system was designed for SERS trace purpose. The results show that designed stellate porous silica delivery system could materialise SERS trace, and show high sensitivity and non-invasive features, which makes the constructed delivery system have considerable capabilities to discover intracellular delivery performances in vitro.

4.2.2. Introduction

A large majority of chemotherapy anticancer drugs and gene medicines are limited by serious side effects caused by lethal dose and the rapid resistances of cancer cells. In that situation, nanoscale drug/gene delivery systems have been employed to overcome these limitations, which caused by poor solubility and stability, high dosage, in vivo degradation, short circulating half-life, poor pharmacokinetic profiles, lack of selectivity of 'free' therapeutic cargos[1-5]. Currently, numerous nanocarriers have been developed for intracellular delivery. Despite the therapeutic purpose of these small systems like high stability for mechanical and thermal changes, high biocompatibility, efficacious fabrication cost and low

toxicity[6-11], the potential cytotoxicity of these very small inorganic nanocarriers has raise great considerations. For these purpose, the trace of inorganic nanocarriers has been established to evaluate the delivery performance of nanocarriers in vitro.

For intracellular trace, a lot of different analytical techniques has been developed. The easiest method is light microscopy, which offers a quick scan of cell morphology and quantity. But this visual resolution is not suitable for specific cell study. Then certain advanced analytic approaches such as electron microscopy and atomic force microscopy are used for a higher resolution bio-image and subcellular structure observation. However, with the limitation of their working principles, these methods can only collect the image of sample surfaces. The inside of cells cannot be observed without killing and sectioning cells. Nevertheless, the above techniques are not sufficient for chemically selective visualization. In that case, external fluorescent labels are used for specifically grafting on the cell structures of interest. Fluorescence microscopy has been introduced for chemically selective trace. In addition, confocal laser scanning fluorescence microscopy is utilized as conventional widely implemented technique for visualizing intracellular uptake. However, as each fluorescence reporter can only excited by one distinct wavelength of laser, simultaneously trace of different structures has great limitations[12]. The artificial fluorescence labelling altered the physic-chemical characteristics of the analyzed system, which might give rise to destructive problems of the system. Alarmingly, photo-bleaching features of fluorophores, and the fluorescent cell background noises might also interrupt the intracellular trace of carrier and drug fate[13]. In order to circumvent these issues, vibrational microscopy like surface enhanced Raman scattering (SERS) technique has been used for non-destructive trace. Unlike fluorescence, Raman reporters are more photo-stable, and the fingerprint Raman signals are not easier interrupted by the auto-fluorescence of cell background.[14] All in

all, the high sensitive and high resolution SERS method is one of the current state-of-the-art technique for bio-imaging, visualization and trace.
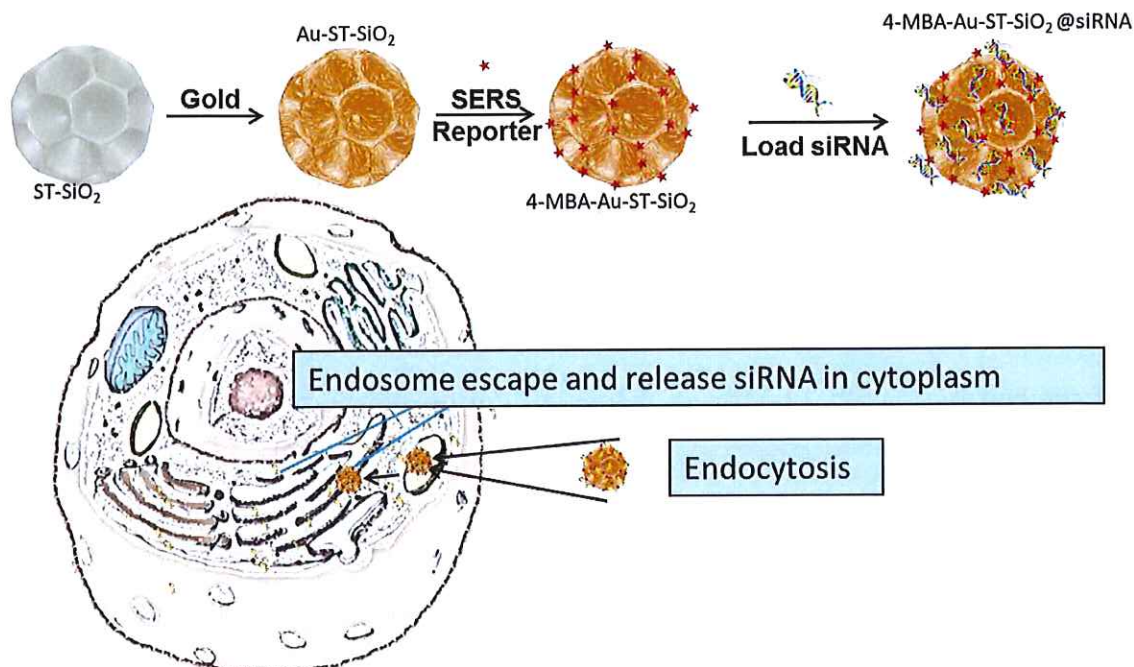
Scheme 4.1 Fabrication of silica nanoparticles with stellate pores based SERS traceable delivery systems and their possible intracellular delivery performances.

In general, SERS is materialized by the combination of SERS tags and SERS reporters. When two SERS tags are in the close vicinity, the electromagnetic field strength can significantly increase and caused the SERS enhancement, which can rocket the Raman signal[15]. The common SERS tags are metallic nanoparticles such as silver and gold, and general structures are nanospheres. However, other structures such as nanorods[16-20], nanoflowers[21-24] and nanostars[25-27] have also been reported. The synthesis of the above metallic SERS tags is complex and limited by high time, cost and energy consumptions. The search for an alternative SERS tag for delivery system could be a good research topic. Only a few work has been reported in this area. In that case, as shown in **Scheme 4.1**, silica-gold composite nanocarriers are designed as novel SERS tags with stellate porous silica platform

together with outside surface aggregation of gold nanoparticles. The possible delivery pathways of the designed delivery systems were also illustrated in **Scheme 4.1**.

4.2.3. Experimental Section

4.2.3.1. Chemicals and Reagents

Triethanolamine (TEA), cetyltrimethylammonium bromide (CTAB), cetyltrimethylammonium tosylate (CTAT), agarose, Human Kinase PLK1 small interfering RNA (siRNA), oligo DNA with same quantity of the bases of siRNA, 4-mercaptobenzoic acid (4-MBA), tetraethyl orthosilicate (TEOS, $\geq$98%), (3-Aminopropyl) triethoxysilane (APTES, $\geq$98%), ethanol solution, dimethyl sulfoxide (DMSO) and other chemicals were purchased from Sigma Aldrich. Human osteosarcoma cell line KHOS was purchased from American Type Culture Collection. Fetal bovine serum (FBS), Dulbecco's modified eagle medium (DMEM), sodium pyruvate (NaP, 100mM), L-Glutamine (200 mM), HEPES (1M) buffers, phosphate buffered saline (PBS), Tris Acetate-EDTA (TAE) buffers, 3-(4,5-Dimethylthiazol-2-yl)-2,5-diphenyltetrazolium bromide (MTT) and trypsin (0.25%) were purchased from Life Technologies Australia Pty Ltd. Gold (III) chloride trihydrate (HAuCl$_4$·3H$_2$O) were purchased from Chem-Supply Australia Pty Ltd. All materials were of analytical grade and used as received without further purification. Millipore water was obtained from a three-stage Millipore Mill-Q plus 185 purified cation system (Academic) with a resistivity higher than 18.2 MΩ·cm.

4.2.3.2. Material Characterisation

Transmission electron microscopy (TEM) images were obtained by a FEI Tecnai G2 Spirit transmission electron microscope at an acceleration voltage of 120 kV. Scanning electron microscopy (SEM) observations were carried out on a FEI Quanta 450 FEG

environmental emission scanning electron microscope operated at 10 kV. A Malvern Zeta-sizer Nano ZS (Malvern Inst. Ltd, U.K.) equipment was used to measure the hydrodynamic sizes and zeta-potentials of different products dispersed in deionized water. The concentration of particles in water was kept at 0.1 ± 0.05 mg/mL for particle size analysis, while the zeta potential results were calculated based on statistical analysis of 10 parallel runs. Fourier transform infrared (FT-IR) spectra were collected at room temperature on a Thermo Scientific NICOLET 6700 FTIR spectrometer with a Diamond ATR (attenuated total reflection) crystal. X-ray diffraction (XRD) patterns were obtained on a powder X-ray diffractometer at 40 kV and 15 mA using Co-Kα radiation (Miniflex, Rigaku). A HORIBA Lab RAM HR Evolution confocal Raman microscopy equipped with 785 nm laser took Raman spectrum and SERS mapping images.

4.2.3.3. Preparation of Stellate Porous Silica (ST-SiO₂)

The formation of stellate porous silica (ST-SiO$_2$) was carried out by TEOS as the silica source, TEA as catalyst and CTAT as pore-makers. According to pervious research reports[28, 29], ST-SiO$_2$ were synthesized at 65 °C. In a typical run, 1.92 g CTAT, 0.347 g TEA first dissolved in 100 mL H$_2$O at 65 °C, and then 14.58 g TEOS was quickly added to the system. After stirring with 1200 rpm for 2 h at 65 °C, the products were centrifuged at 16000 rpm, washed with deionized water and dried in a 60 °C oven overnight. In order to remove surfactants, the products were calcined at 550 °C for 6 h by a Muffle furnace with a ramp rate of 0.5 °C min^{-1} in air.

4.2.3.4. Preparation of Gold Nanoparticles aggregated Stellate Porous Silica

0.01 g calcined ST-SiO$_2$ were dispersed in 40 mL ethanol, and then 0.05 mL APTES was added into the solution. After 800~1000 rpm stirring at 80 °C for 24 h, centrifuged and washed by water, amino functionalized ST-SiO$_2$ were obtained. The gold nanoparticles

aggregated stellate porous silica (Au-ST-SiO$_2$) were synthesized by the deposition–precipitation method. Typically, 0.01 g of amino functionalized ST-SiO$_2$ was dispersed in 10 mL H$_2$O, the color of the solution turned from white to yellow after addition of 2mL of HAuCl$_4$ (2 mM). Then under 30 min sonication in deionized water, certain amount of 0.075 wt % fresh aqueous NaBH$_4$ was added dropwise until the solution color turned pale red. The precipitate Au-ST-SiO$_2$ was centrifuged at 16000 rpm, washed with deionized water, and dried in a 60 °C oven for 24 h.

4.2.3.5. Preparation of SERS Reporters attached Nanocarriers

1 mM 4-MBA was added to Au-ST-SiO$_2$ with molar ratio at 1:100. After stirring for 24 h, centrifuged at 16000 rpm, washed with deionized water and dried in a 60 °C oven for 24 h, the SERS reporter 4-MBA was aggregated on silica nanoparticles and formed 4-MBA-Au-ST-SiO$_2$.

4.2.3.6. Loading Capacity of small interfering RNA (siRNA)

Agarose gel electrophoresis was used to obtain the loading capacity of siRNA on 4-MBA-Au-ST-SiO$_2$ nanocarriers. An oligo DNA with same quantity of the bases of functional siRNA was employed as model gene for electrophoresis. Different weight ratios from 10:1 to 200:1 of various weight of nanocarriers to 0.2 µg model DNA together with a naked model DNA as a control were incubated at room temperature for 30 min before adding gel loading dye blue. Samples were electrophoresed through a gel red stained 0.8% agarose gel in TAE buffer solution at 90 V for 90 min. The gene migration patterns were recorded and collected by UV irradiation (G-BOX, SYNGENE).

4.2.3.7. Cell Culture and Cell Viability

Human osteosarcoma cell line KHOS were incubated in cell growth medium (90% (v/v) DMEM, 10% (v/v) fetal bovine serum (FBS) and 1% Anti-anti) at 37 °C, 5% CO$_2$ and

humidified atmosphere. While in the same incubation environment, human embryonic kidney cell line HEK 293T were incubated in cell growth medium containing (90% (v/v) DMEM, 10% (v/v) fetal bovine serum (FBS), 0.1% sodium pyruvate (NaP), 0.1%L-Glutamin, 0.15% HEPES and 1% Anti-anti. MTT assay was used to evaluate cell viabilities of 4-MBA-Au-ST-SiO$_2$ in each cell line. KHOS and HEK 293T cells were seeded into a 96-well plate at a density of 5×10^4 cells mL^{-1}, and incubated in 100 μL cell culture medium for 24 h. After that, the previous medium was replayed by 100 μL of fresh cell culture medium containing selected concentrations of different particles (4-MBA-Au-ST-SiO$_2$, siRNA @ 4-MBA-Au-ST-SiO$_2$ and free siRNA). After incubation for 24 h, 10 μL of 0.5 mg mL^{-1}MTT was added to each well and further incubated 4 h. Later, the medium in each well was replaced by 150 μL DMSO to dissolve formazan crystals. The MTT assays were conducted in quadruplicate for each sample, and the absorbance of formazan crystals was measured by an ELx808 Absorbance Microplate Reader (Biotek, USA) at 595 nm.

4.2.3.8. Cell Uptake Traced by Confocal Raman Microscopy

Cellular uptake of 4-MBA-Au-ST-SiO$_2$@siRNA was observed with a confocal Raman laser scanning microscopy. In a 6-well plate, 2×10^5 KHOS cells were seeded at a quartz slide with 2 mL growth medium inside each well. After cultured for 24 h, the medium was replaced by 1 mL of 1 μg mL^{-1} 4-MBA-Au-ST-SiO$_2$@siRNA /fresh growth medium solution. After 4 h incubation, the quartz slide with cells and composites were softly washed by PBS buffer twice. The Raman mapping images of cellular uptake were collected by a HORIBA Lab RAM HR Evolution Raman laser scanning microscope under 785 nm laser.

4.2.4. Results and Discussion

The 4-MBA-Au-ST-SiO$_2$@siRNA delivery system was constructed following the procedures and their possible intracellular delivery performances were also illustrated in **Scheme 4.1**. As shown here, when the 4-MBA-Au-ST-SiO$_2$@siRNA are delivered to cancer cells, endocytosis phenomena and endosome escape will occur and siRNA molecules will release to the cytoplasm to carry out their pharmacological and anti-cancer functions.

4.2.4.1. Synthesis and Characterization of nanocarriers

Stellate porous silica (ST-SiO$_2$) was synthesized by TEOS, TEA and CTAT sol-gel synthesis procedure[28, 29]. Scanning electron microscopy (SEM) and transmission electron microscopy (TEM) images show that ST-SiO$_2$ (**Figure S4.1a and b**) with an average particle size of 80-120 nm can be synthesized. After removal of surfactants, the uniform morphology of ST-SiO$_2$ is clearly demonstrated as nanospheres (**Figure S4.1c and Figure S4.2a**) with center-radial pores of 10-30 nm (**Figure S4.1d and Figure S4.2b**). The size is further verified from dynamic light scattering (DLS) measurements (**Table S4.1**). The average hydrodynamic size of ST-SiO$_2$ is 97.2 nm with an average zeta potential of - 30.5 ± 0.7 mV. In FT-IR of ST-SiO$_2$ (**Figure 4.2b**), peaks centre at 1068 cm^{-1}, 945 cm^{-1} and 800 cm^{-1} can be attributed to the typical silica Si-O-Si asymmetric stretching, Si-OH and Si-O symmetric stretching vibrations. In the wide-angle XRD pattern of ST-SiO$_2$ (**Figure 4.2a**), the broad diffraction peak around $2\theta = 22.8°$ demonstrates the evidence of the amorphous silica.

The NH$_2$-ST-SiO$_2$ nanospheres were synthesized by APTES post-graft amino groups, and their existence were measured by DLS (**Table S4.1**), where an average hydrodynamic size is 105 nm with an average zeta potential of 27.1 ± 1.2 mV. From ST-SiO$_2$ to NH$_2$-ST-SiO$_2$, the zeta potential change from negative to positive, which is the evidence of successful

amino groups functionalization. In FT-IR(**Figure 4.2b**), typical silica vibrations at 1068 cm^{-1}, 945 cm^{-1} and 800 cm^{-1} can be found, while 3350 cm^{-1} is attributed to the vibrations of amino groups.

Au-ST-SiO$_2$ was fabricated by in-situ reduction of HAuCl$_4$·3H$_2$O on amino functionalized ST-SiO$_2$ using deposition–precipitation method[30]. In TEM images (**Figure 4.1a and b**), fresh prepared Au-ST-SiO$_2$ are uniform nanospheres with an average particle diameter around 100 nm, and gold nanoparticles with varied small sizes ranging from 2 - 20 nm are aggregated on the surfaces of ST-SiO$_2$ skeletons. The surrounding background is clear compared to TEM images (**Figure 4.1c, d and Figure S4.2c and d**) taken from Au-ST-SiO$_2$ stored in ethanol solutions several days later. In high magnitude images (**Figure 4.1d and S4.2d**), it can be noticed that small gold nanoparticles are distributed inside stellate pores and stable around ST-SiO$_2$. From DLS (**Table S4.1**), Au-ST-SiO$_2$ composites have an average hydrodynamic size of 198.2 nm with zeta potential of 8.7 ± 0.6 mV. The large increase of size may be due to two or several particle aggregations. The decrease of zeta potential value from NH$_2$-ST-SiO$_2$ to Au-ST-SiO$_2$ may be attributed to the electrostatic adsorption between gold and amino groups. In addition, the capillary adsorption of stellate pores can be another contribution to gold-silica aggregations. From the wide-angle XRD pattern of Au-ST-SiO$_2$ (**Figure 4.2a**), diffraction angle 2θ = 22.8° is attributed to amorphous silica existence, while 2θ =38.18°, 44.39°, 64.58° and 77.55° can match the standard gold planes of (111), (200), (220) and (311) from JCPDS card. The intensity proportion of the tested sample can also match the standard one shown by red vertical line.
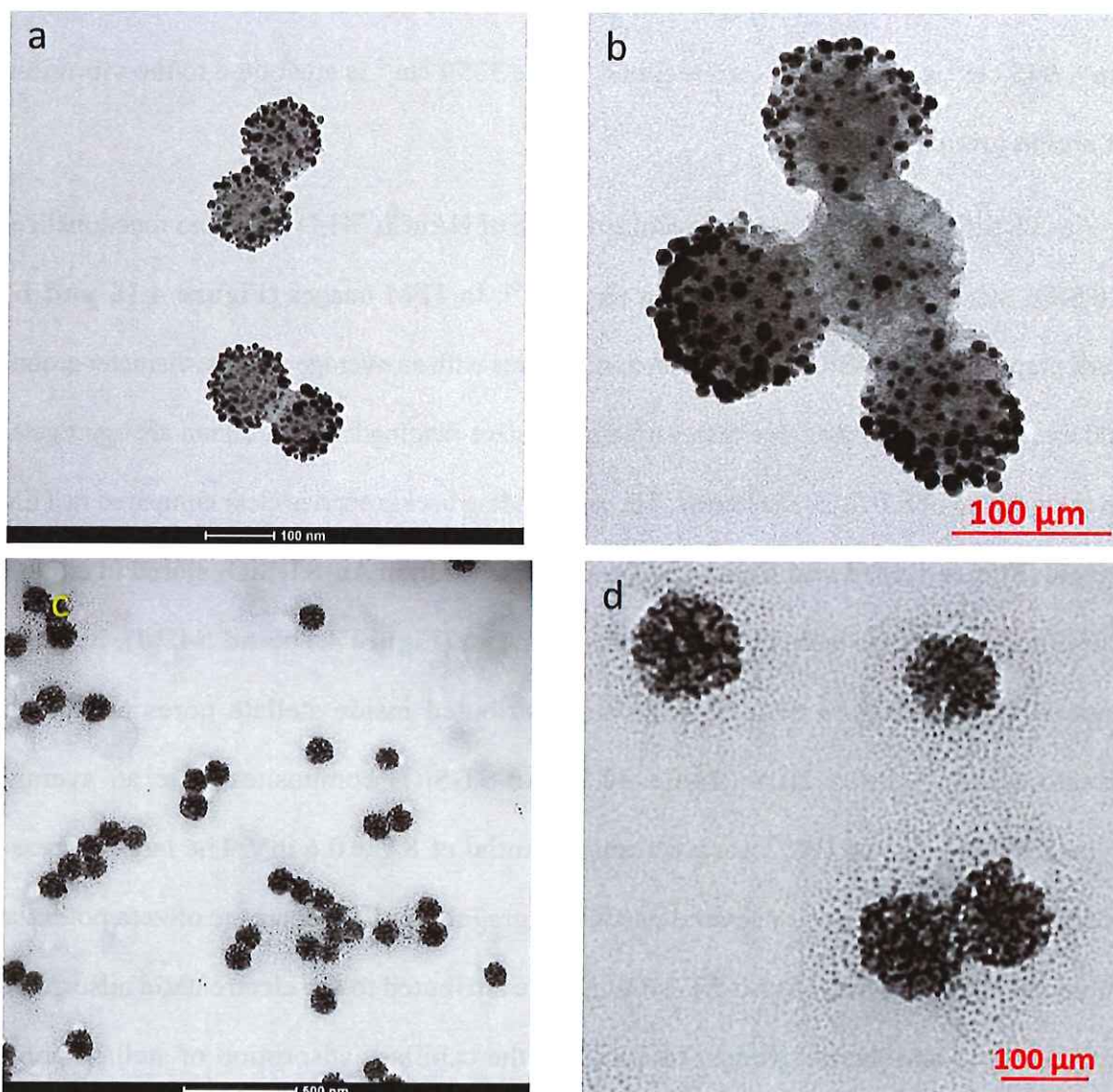
Figure 4.1. TEM images of fresh prepared Au-ST-SiO$_2$ (a, b) and Au-ST-SiO$_2$ stored several days (c, d).

4-MBA-Au-ST-SiO$_2$ nanocarriers were fabricated by attaching SERS reporter 4-MBA on Au-ST-SiO$_2$ [31, 32]. FTIR spectroscopy (**Figure 4.2b**) shows peaks centre at 3350 cm^{-1}, 1068 cm^{-1}, 945 cm^{-1} and 800 cm^{-1} for -NH$_2$, Si-O-Si, Si-OH and Si-O groups vibrations, while peak centres at 1735 cm^{-1} may be the evidence of -COOH group vibrations from 4-MBA. The 4-MBA attachments were also verified by SERS spectra (**Figure 4.2d**). For pure SERS reporter 4-MBA, obvious Raman peaks at 1099.1 cm^{-1}

66
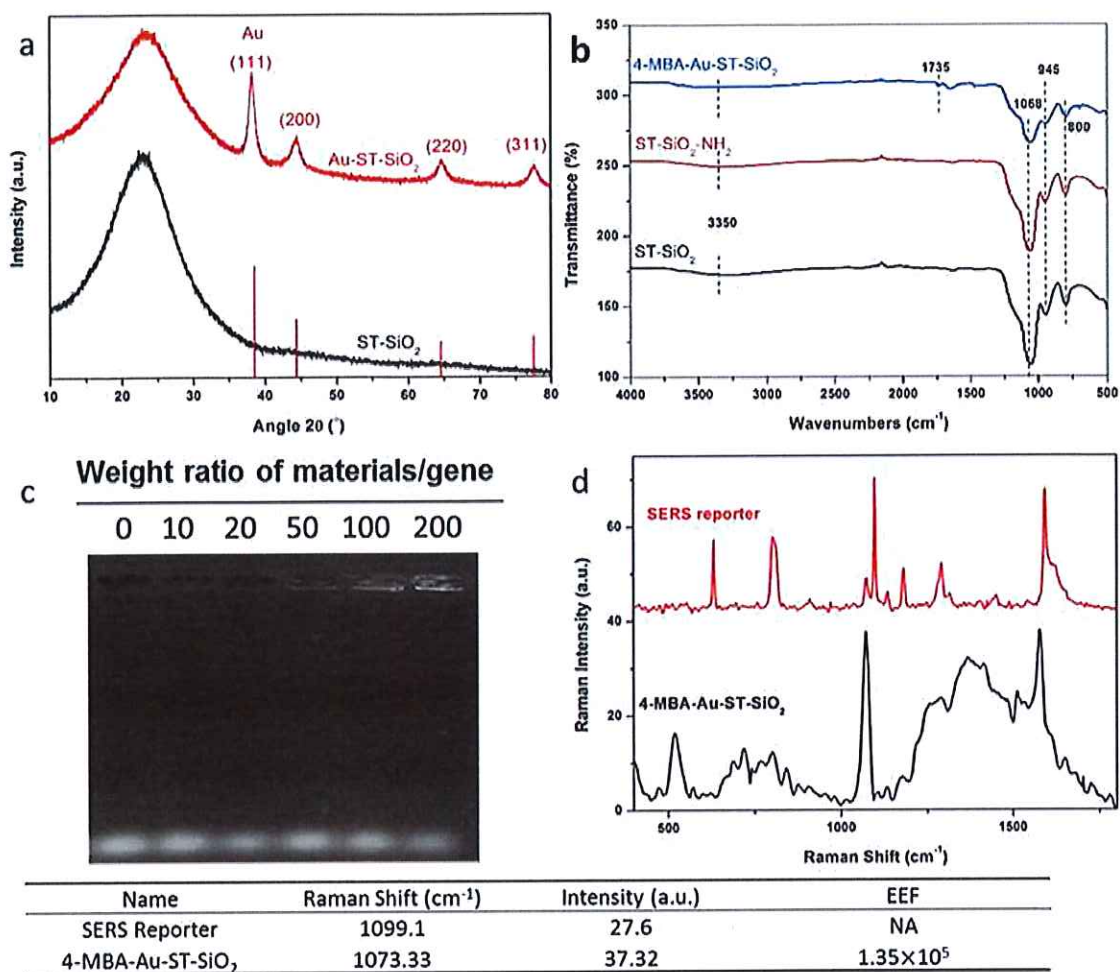
Figure 4.2. a) XRD pattern of Au-ST-SiO₂ and ST-SiO₂ with standard gold intensity obtained from JCPDS card no. 04-0784, b) FTIR of 4-MBA-Au-ST-SiO₂, ST-SiO₂ -NH₂ and ST-SiO₂, c) agarose gel retardation assay of materials/siRNA at different weight ratios, d) Raman spectra of SERS reporter 4-MBA and nanocarriers 4-MBA-Au-ST-SiO₂ together with the calculated effective enhancement factor (EEF).

and 1595.5 cm^{-1} are due to υ8a and υ12 aromatic ring vibrations[31]. While in SERS spectrum of 4-MBA-Au-ST-SiO₂, the dominate peaks are centered at 1073.3 cm^{-1} and 1585.5 cm^{-1}, these blue shift can be attributed to the interactions between 4-MBA and gold nanoparticles. Effective enhancement factor (EEF) of 4-MBA-Au-ST-SiO₂ can be roughly calculated by the following equation.

$$EEF = \frac{I_{SERS}N_{bulk}}{I_{bulk}N_{SERS}}$$

Where I_{SERS} and I_{bulk} are the intensities of SERS and bulk spectra at the 1078 cm^{-1} band, $\frac{N_{bulk}}{N_{SERS}}$ is the molar ratio between bulk and SERS sample[31, 33]

As shown in Table from **Figure 4.2d**, EEF of 4-MBA-Au-ST-SiO$_2$ is calculated as approximate 1.35×10^5, based on 1099.1 cm^{-1} Raman peak as reference. That means the constructed 4-MBA-Au-ST-SiO$_2$ nanocarriers can really trigger SERS phenomenon and SERS technique has high sensitivity.

4.2.4.2. Binding capabilities of small interfering RNA

The Binding capabilities of small interfering RNA (siRNA) on 4-MBA-Au-ST-SiO$_2$ nanocarriers was measured by agarose gel electrophoresis. For economic reason, a model oligo DNA instead of expensive siRNA with same quantity of the bases of functional siRNA was applied for experiments. As shown in **Figure 4.2c**, the weight ratio of nanocarriers to model DNA is range from 10 to 200 with a naked oligo DNA as a control. The brightness of binding DNA occurs and increases from weight ratio 50 to 200, showing the 4-MBA-Au-ST-SiO$_2$ nanocarriers have binding capabilities of gene. In addition, the brightness decrease of escaped DNA also verified gene binding. The designed delivery nanocarriers can load siRNA at the weight ratio of nanocarriers to siRNA of 200, and that value was used for cell viability studies.
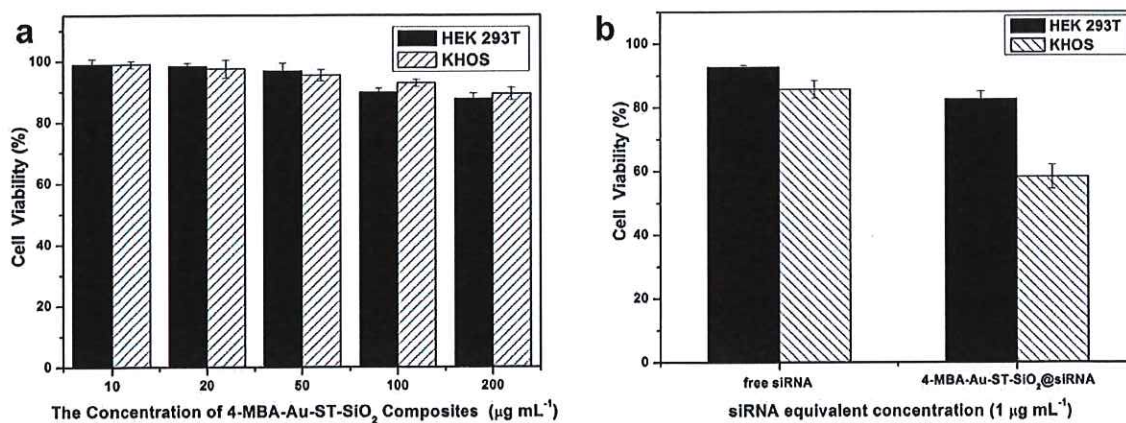
Figure 4.3. a) The biocompatibility and b) cytotoxicity studies in healthy human cell line HEK 293T and human osteosarcoma cell line KHOS.

4.2.4.3. cell viability studies

For cell viability studies, the biocompatibilities of 4-MBA-Au-ST-SiO$_2$ nanocarriers and the cytotoxicities of 4-MBA-Au-ST-SiO$_2$@siRNA were investigated by 3-(4,5-dimethylthiazol-2-yl)-2,5-diphenyltetrazolium bromide (MTT) assays against human embryonic kidney (HEK 293T) and human osteogenic sarcoma (KHOS) cell lines. As illustrated in **Figure 4.3a**, cell viabilities of both HEK 293T and KHOS cells remain above 85% with 4-MBA-Au-ST-SiO$_2$ nanocarriers concentration increase from 10 to 200 µg mL^{-1}. It is evident that 4-MBA-Au-ST-SiO$_2$ nanocarriers are biocompatible in both healthy and cancer cells.

Based on the binding 200 weight ratio of nanocarriers to siRNA, 4-MBA-Au-ST-SiO$_2$@siRNA were synthesised, while an equivalent concentration of 1 µg mL^{-1} free siRNA/cell growth medium and 4-MBA-Au-ST-SiO$_2$@siRNA/ cell growth medium mixtures were prepared for MTT assays. As demonstrated in **Figure 4.3b**, free siRNA and 4-MBA-Au-ST-SiO$_2$@siRNA have little toxicity in HEK 293 cells with cell viabilities around 98.2 and 85.7 %. However, the results in KHOS cell line are different.

1 μg mL^{-1} free siRNA is a bit cytotoxic in KHOS cells with 81.6 % cell viability, but siRNA @ 4-MBA-Au-ST-SiO$_2$ with equivalent concentration demonstrate higher anti-cancer abilities with corresponding cell viability of 57.7 %. In consequence, delivery systems could make the siRNA have better pharmacological treatment performance.

4.2.4.4. SERS traced cellular uptake

Cellular uptake of 4-MBA-Au-ST-SiO$_2$ carriers were observed with confocal Raman laser scanning microscopy. The traced SERS mapping image were taken based on the intensity of SERS spectra peak centred at Raman shift of 1073.3 cm^{-1}.

Figure 4.4a shows the optical image of KHOS cells containing 4-MBA-Au-ST-SiO$_2$ nanocarriers which taken photo after SERS tracing. The mapping area with approximate 6 cells is shown by red rectangle frame and enlarged in the right corner with each tested mapping point shown by green cursor. The cell morphologies are good for well-growth cells, which means they are healthy and alive at the moment of taking photo. The selected points 1 and 2 are represented the signal obtained from the cell and that from the quartz background (**Figure 4.4b**). Their corresponding SERS spectra are demonstrated in **Figure 4.4c**, while the original mapping data is shown in **Figure S4.3 and S4.4**. The 1260 cm^{-1} peak is attributed to quartz substrates, while SERS peak centred at 1073.3 cm^{-1} can be obviously noticed in the SERS spectrum of point 1 (**Figure 4.4c**). The SERS mapping images illustrated in **Figure 4.4d**. The brightness of red cursor is reflected the intensity of 1073.3 cm^{-1} SERS peak. **Figure 4.4e** is the merged image, which shows that the SERS mapping image and optical image are identical and can match successfully. This performance can confirm the feasibility of SERS tracing 4-MBA-Au-ST-SiO$_2$. As the morphologies of cells were not change or damaged after SERS trace, it means that cells are non-destructive during trace procedure.
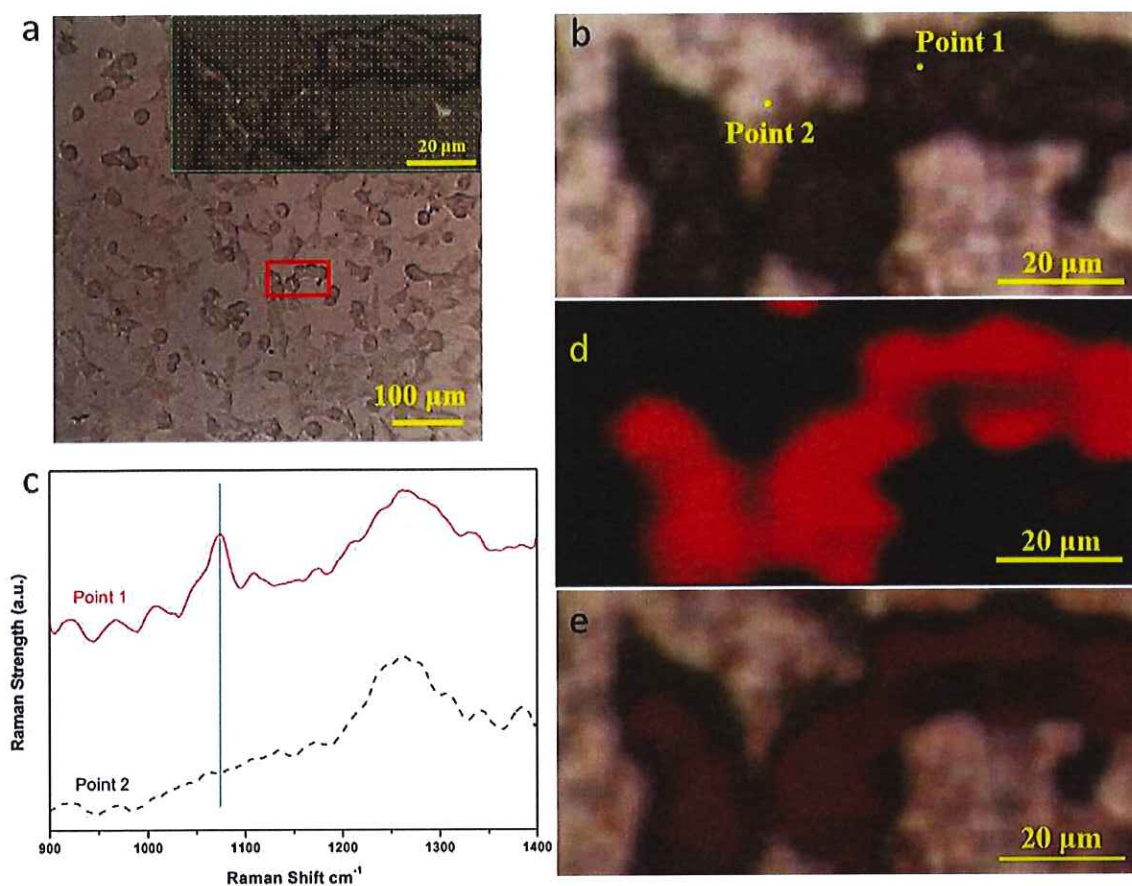
Figure 4.4. a) Optical image with marked selected mapping area (the inset shown the enlarged mapping area with each tested point), b) optical image of the selected points, c) SERS spectrum of points 1 and 2, d) SERS image and e) the merged image.

4.2.5. Conclusion

The novel surface-enhanced Raman scattering (SERS) traceable delivery system has been synthesized under a stellate porous silica platform. In here, gold nanoparticles were obtained by in-site reduction of $HAuCl_4·3H_2O$, and aggregated on silica skeleton by electrostatic and capillary adsorptions. The special gold-silica structure can give the delivery system SERS active effects and form SERS tags, which allows the SERS trace to be possible. In addition, SERS trace is great for delivery performance, as it has high sensitivity and non-

invasive features, which makes the constructed delivery system have considerable capabilities to discover real-time delivery performances in living cells.

4.2.6. Supporting Information

Stellate Porous Silica based Surface-Enhanced Raman Scattering (SERS) traceable delivery systems
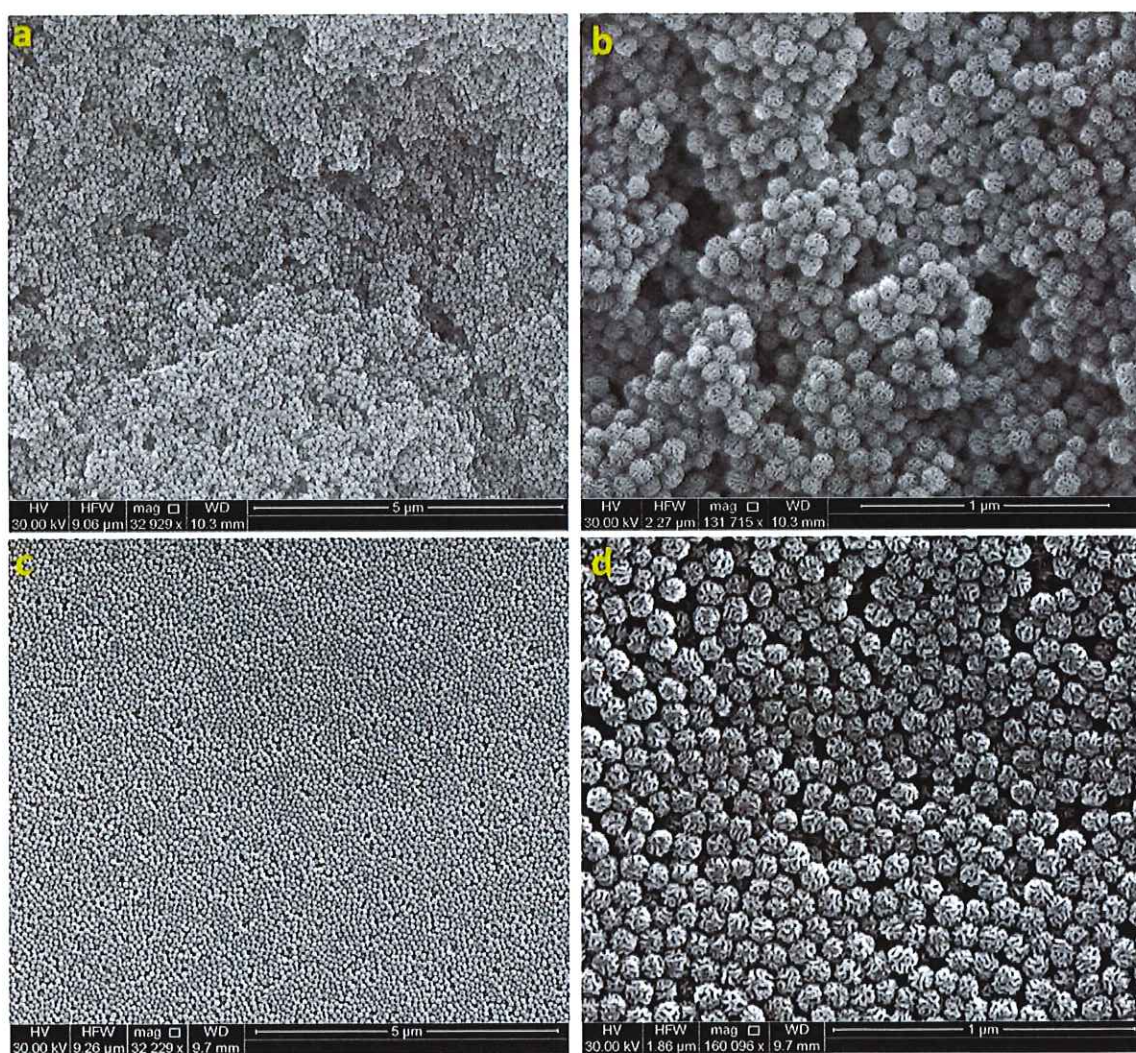
Figure S4.1. SEM images of silica with stellate pores with (a, b) and without (c, d) surfactants in low magnitude (a, c) and high magnitude (b, d).
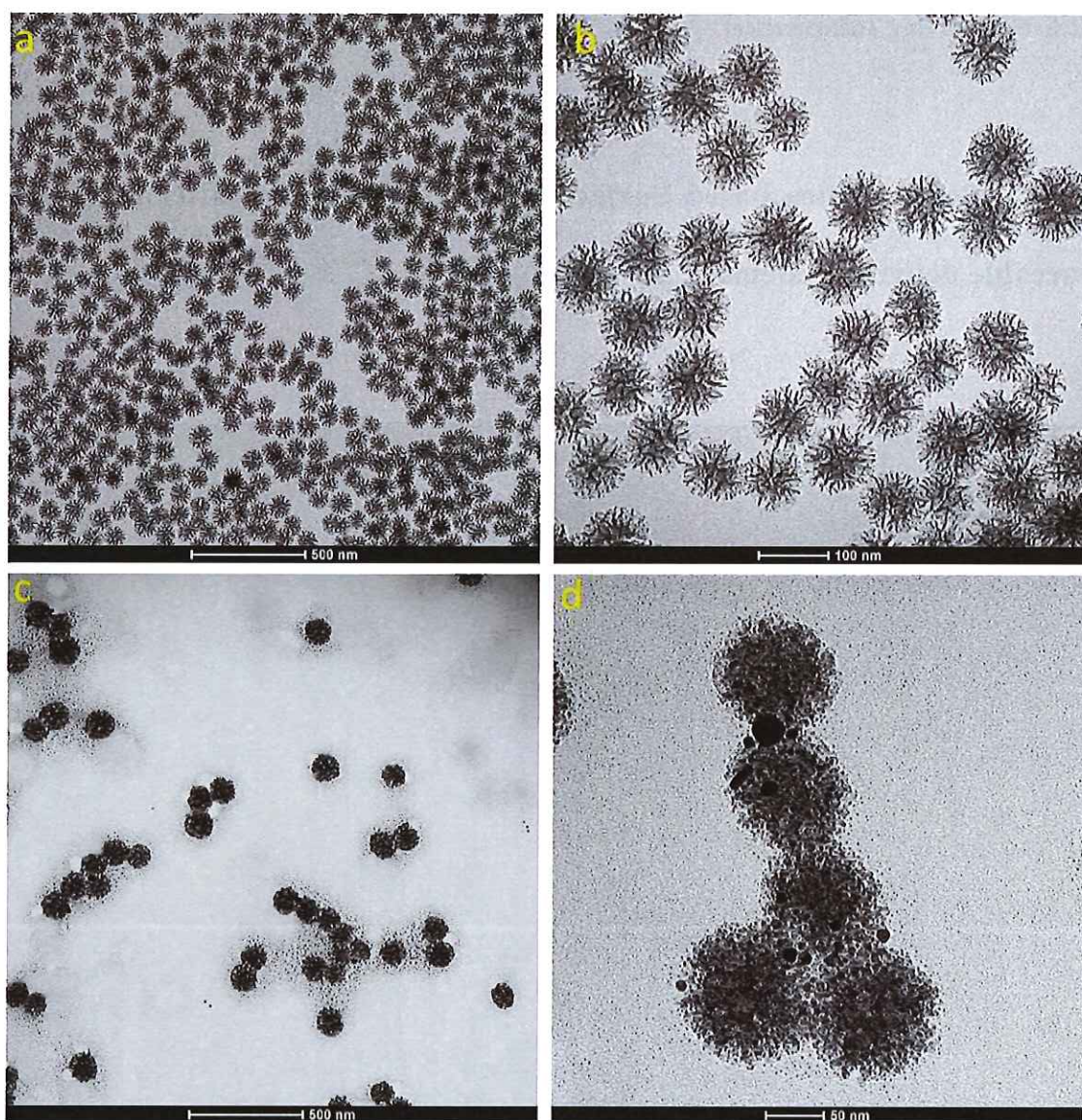
Figure S4.2. TEM images of ST-SiO$_2$(a, b) and Au-ST-SiO$_2$ (c, d) in low magnitude (a, c) and high magnitude (b, d).
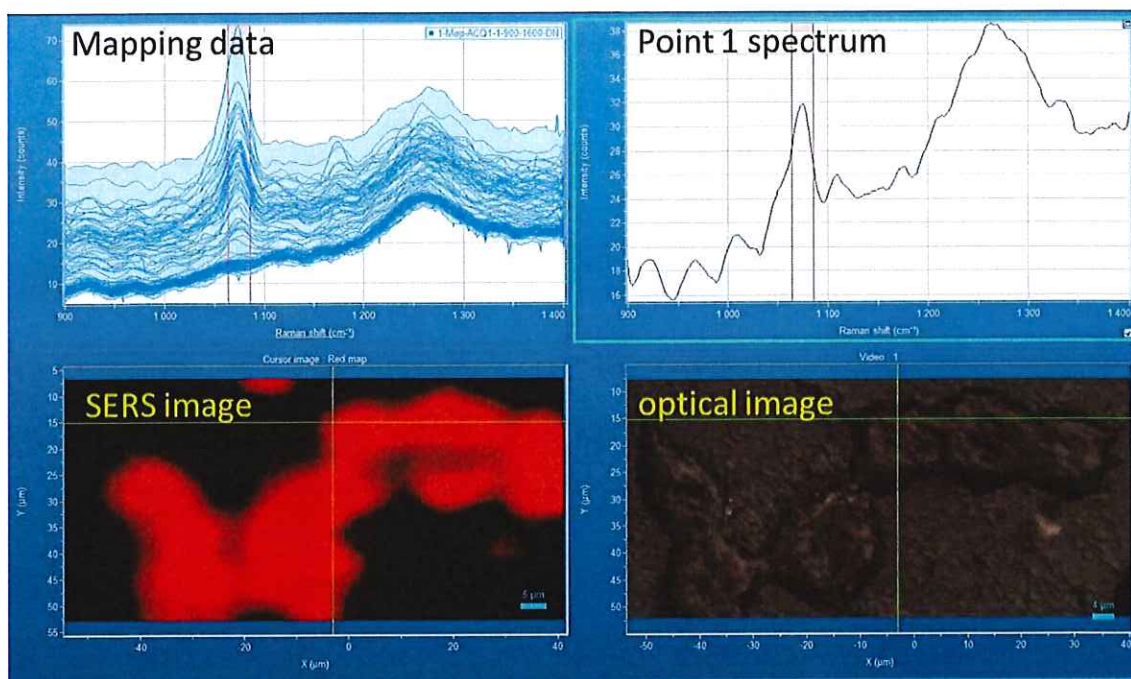
Figure S4.3. Original mapping data, SERS image and optical image of 4-MBA-Au-ST-SiO$_2$ in HeLa cells and SERS spectrum of selected point 1.
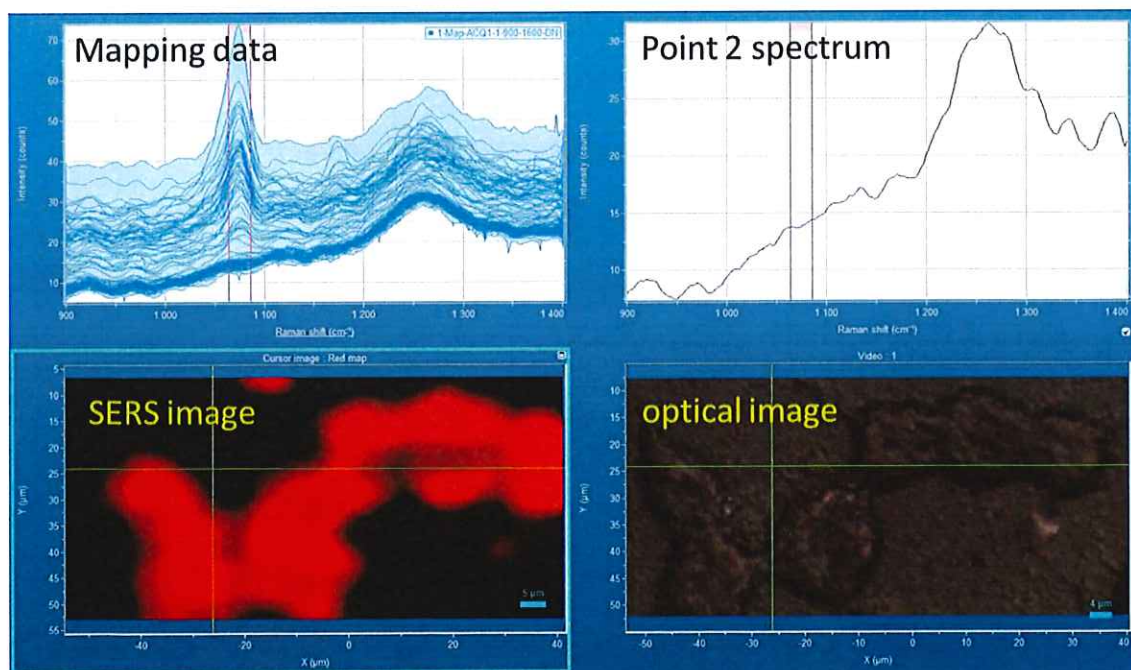
Figure S4.4. Original mapping data, SERS image and optical image of 4-MBA-Au-ST-SiO$_2$ in HeLa cells and SERS spectrum of selected point 2.

Table S4.1 Hydrodynamic sizes and zeta potential of samples measured at pH=7.

Sample Name	Zeta Potential (mV)	Size (nm)	PDI
ST-SiO$_2$	-30.5 ± 0.7	97.2	0.34
NH$_2$-ST-SiO$_2$	27.1 ± 1.2	105	0.31
Au-ST-SiO$_2$	8.7 ± 0.6	198.2	0.36

4.2.7. Acknowledgements

4.2.8. Reference

[1]   D. Peer, J. M. Karp, S. Hong, O. C. Farokhzad, R. Margalit, R. Langer, **2007**, *2*, 751.

[2]   F. Meng, R. Cheng, C. Deng, Z. Zhong, *Materials Today* **2012**, *15*, 436.

[3]   Y. Wang, P. Brown, Y. Xia, *Nat Mater* **2011**, *10*, 482.

[4]   C. E. Ashley, E. C. Carnes, G. K. Phillips, D. Padilla, P. N. Durfee, P. A. Brown, T. N. Hanna, J. Liu, B. Phillips, M. B. Carter, N. J. Carroll, X. Jiang, D. R. Dunphy, C. L. Willman, D. N. Petsev, D. G. Evans, A. N. Parikh, B. Chackerian, W. Wharton, D. S. Peabody, C. J. Brinker, **2011**, *10*, 389.

[5]   M. E. Davis, Z. Chen, D. M. Shin, *Nat Rev Drug Discov* **2008**, *7*, 771.

[6]   Z. Wang, G. Liu, H. Zheng, X. Chen, *Biotechnology Advances* **2014**, *32*, 831.

[7]   Q. He, J. Shi, *Adv Mater* **2014**, *26*, 391.

[8]   Y. Gao, J. Xie, H. Chen, S. Gu, R. Zhao, J. Shao, L. Jia, *Biotechnology Advances* **2014**, *32*, 761.

[9]   C. Argyo, V. Weiss, C. Bräuchle, T. Bein, *Chemistry of Materials* **2014**, *26*, 435.

[10] Z. Teng, X. Su, Y. Zheng, J. Sun, G. Chen, C. Tian, J. Wang, H. Li, Y. Zhao, G. Lu, *Chemistry of Materials* **2013**, *25*, 98.

[11] X. Fang, X. Zhao, W. Fang, C. Chen, N. Zheng, *Nanoscale* **2013**, *5*, 2205.

[12] M. Vendrell, K. K. Maiti, K. Dhaliwal, Y.-T. Chang, *Trends in Biotechnology* **2013**, *31*, 249.

[13] B. Fahrenkrog, U. Aebi, *Nat Rev Mol Cell Biol* **2003**, *4*, 757.

[14] S. Keren, C. Zavaleta, Z. Cheng, A. de la Zerda, O. Gheysens, S. S. Gambhir, *Proceedings of the National Academy of Sciences of the United States of America* **2008**, *105*, 5844.

[15] K. A. Stoerzinger, J. Y. Lin, T. W. Odom, *Chemical science* **2011**, *2*, 1435.

[16] S. Zong, Z. Wang, H. Chen, D. Zhu, P. Chen, Y. Cui, *Ieee Transactions on Nanobioscience* **2014**, *13*, 55.

[17] S. Zong, Z. Wang, H. Chen, J. Yang, Y. Cui, *Analytical chemistry* **2013**, *85*, 2223.

[18] D. Lin, T. Qin, Y. Wang, X. Sun, L. Chen, *Acs Applied Materials & Interfaces* **2014**, *6*, 1320.

[19] L. Xiao, S. Harihar, D. R. Welch, A. Zhou, *Analytica Chimica Acta* **2014**, *843*, 73.

[20] Z. Wang, S. Zong, W. Li, C. Wang, S. Xu, H. Chen, Y. Cui, *Journal of the American Chemical Society* **2012**, *134*, 2993.

[21] J. Xie, Q. Zhang, J. Y. Lee, D. I. C. Wang, *ACS Nano* **2008**, *2*, 2473.

[22] J. Fang, S. Du, S. Lebedkin, Z. Li, R. Kruk, M. Kappes, H. Hahn, *Nano Letters* **2010**, *10*, 5006.

[23] Z. Wang, J. Zhang, J. M. Ekman, P. J. A. Kenis, Y. Lu, *Nano Letters* **2010**, *10*, 1886.

[24] Q. Li, Y. Jiang, R. Han, X. Zhong, S. Liu, Z.-Y. Li, Y. Sha, D. Xu, *Small* **2013**, *9*, 927.

[25] A. M. Fales, H. Yuan, T. Vo-Dinh, *Langmuir* **2011**, *27*, 12186.

[26] A. M. Fales, H. Yuan, T. Vo-Dinh, *Molecular Pharmaceutics* **2013**, *10*, 2291.

[27] H. Yuan, A. M. Fales, C. G. Khoury, J. Liu, T. Vo-Dinh, *Journal of Raman spectroscopy : JRS* **2013**, *44*, 234.

[28] L. Xiong, X. Du, B. Shi, J. Bi, F. Kleitz, S. Z. Qiao, *Journal of Materials Chemistry B*

2015, *3*, 1712.

[29]   K. Zhang, L. L. Xu, J. G. Jiang, N. Calin, K. F. Lam, S. J. Zhang, H. H. Wu, G. D. Wu, B. Albela, L. Bonneviot, P. Wu, *Journal of the American Chemical Society* **2013,** *135*, 2427.

[30]   X. Du, J. He, *Nanoscale* **2012,** *4*, 852.

[31]   L. Wei, B. Jin, S. Dai, *The Journal of Physical Chemistry C* **2012,** *116*, 17174.

[32]   A. Michota, J. Bukowska, *Journal of Raman Spectroscopy* **2003,** *34*, 21.

[33]   P. H. C. Camargo, L. Au, M. Rycenga, W. Li, Y. Xia, *Chemical Physics Letters* **2010,** *484*, 304.

Chapter 5 Novel Graphitic Carbon Nitride Platform for Raman Traceable Delivery System

5.1. Introduction, Significance and Commentary

Graphitic carbon nitride (g-C_3N_4) composites have been constructed as gene delivery systems. As g-C_3N_4 has self-fluorescence and Raman-active features, intracellular delivery performances of delivery systems can be dual traced without labels. The highlights of this work include:

1. g-C_3N_4 nanosheets based gene delivery system

Although graphitic carbon nitride materials have been introduced to drug delivery areas, g-C_3N_4 nanosheets are seldom reported for delivering gene or siRNA in cancer cells.

2. Novel low molecular weight PEI system

Low molecular weight polyethylenimine (PEI) is a well-known biocompatible component for gene delivery system, this work is the first low molecular weight PEI combined with emerging g-C_3N_4 composite system.

3. Label-free tracing

Self-fluorescence and Raman-active g-C_3N_4 nanosheets facilitate direct tracing materials without artificial labels that might change physicochemical properties, uptake pathways and pharmacological effects of the delivery systems. This designed PEI-g-C_3N_4 systems are label-free.

4. Raman traceable delivery system

The intracellular performances of siRNA delivery system were traced by novel Raman

methods. As Raman trace results have higher sensitivities than common fluorescence ones, it could effectively replace widely implemented fluorescence tracing.

5.2. Graphitic Carbon Nitride Composites: Label-free Direct Raman Traceable siRNA Delivery System

This section is included in the thesis as it appears as an unpublished and unsubmitted work written in manuscript style.

5.2.1. Abstract

A novel ultrathin graphitic carbon nitride (g-C_3N_4) based system with small sheet size of 100-150 nm and thickness of nearly 0.6 nm has been developed for small interfering RNA (siRNA) delivery. The g-C_3N_4 materials was surface modified with low molecular weight branched polyethylenimine (PEI) to obtain the capabilities of siRNA loading. The simple and label-free siRNA delivery system, which avoid possible interactions of artificial labels, shows clear cytotoxicity in KHOS cancer cells and good biocompatibility in HEK293 normal human cells. As g-C_3N_4 is Raman-active, the intracellular uptake performances of the label-free delivery system have been directly traced by Raman spectroscopies. Since Raman signals have finger-print pattern and are not interrupted by background noises, Raman traced images demonstrate higher sensitivity and resolution than common fluorescence traced results, which makes it as a better method for real-time tracing and revealing nanotoxicity of delivery carriers.

5.2.2. Introduction

Cancer is one of the most life-threatening diseases against human race. Gene therapy has been considered as an alternative to chemotherapy in treating acute or chronic, acquired and inherited cancers [1, 2]. However, successful gene therapy needs to across multiple extracellular and intracellular barriers, such as poor gene stability caused by enzymes in human blood and serum, low rates of cellular uptake and endosomal escape [3-5]. To overcome these obstacles, numerous efforts on viral and polymeric carriers have been made, and nanoparticles have been introduced as promising carriers with good biocompatibilities and well-controlled gene delivery efficiency. Among gene treatments, small interfering RNA (siRNA) interference therapeutic play a critical and irreplaceable role in anticancer therapy, and the developments of nanoparticle-based siRNA delivery vehicles are strongly required for successful siRNA therapy[6, 7].

Due to unique structural, optical, biocompatible and physicochemical properties like high degree of specific surface areas, anisotropy and in thus high surface functionality, two-dimensional (2D) ultrathin materials have recently draw the numerous attentions from researchers [8-13]. Graphitic carbon nitride (g-C_3N_4), which was only synthesised in recent years [14-21], is an emerging member of the 2D layered nanomaterials for photochemical and electrochemical catalysis. However, for biomedical fields such as cancer cell diagnostics, biosensor, biomedical and drug/gene delivery applications, these g-C_3N_4 has been required having specific features like photoluminescence[22, 23], self-fluorescence[24] and high stability[25-28], but having small size (100-200 nm), and great biocompatibility as well. Although many efforts, as the liquid or water ultrasonic exfoliating method for example[26], has been made for producing g-C_3N_4 with uniform small sheet size, the efficient large-scale synthesis is still in its infancy.
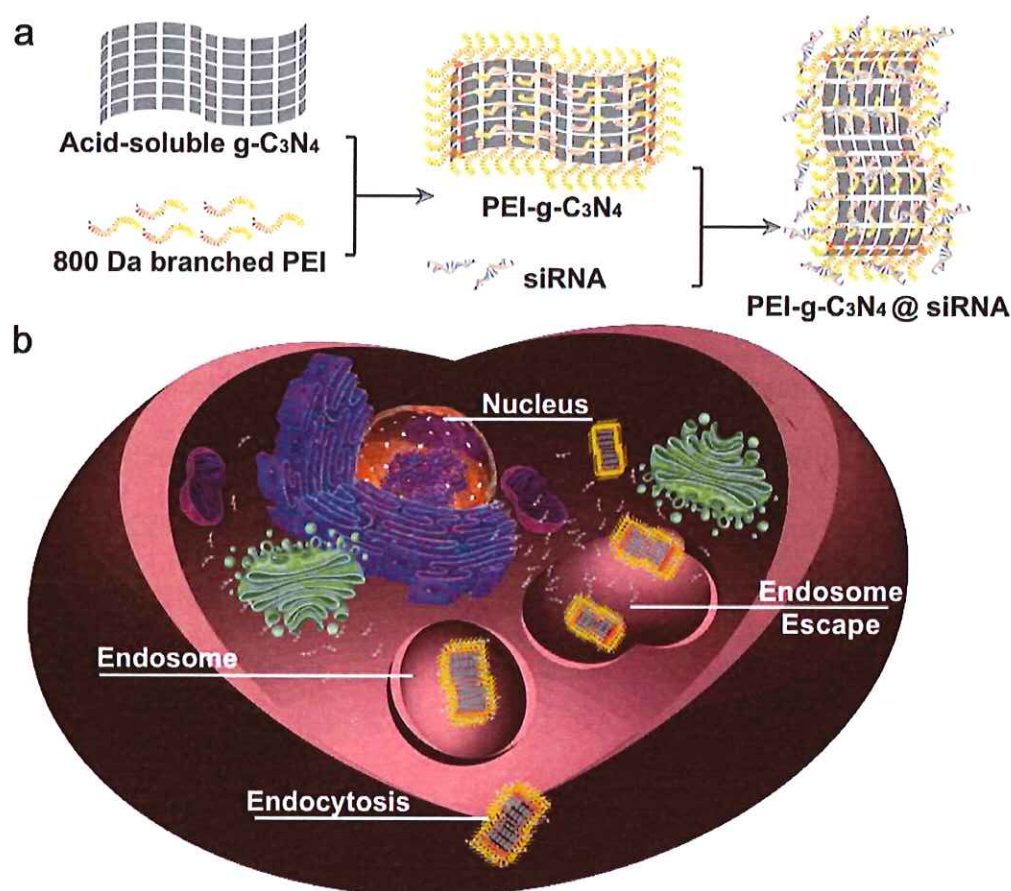
Scheme 5.1 a) synthesis process of low molecular weight PEI-g-C$_3$N$_4$@siRNA system and b) their possible intracellular delivery performances.

Since nanotoxicity of delivery carriers has raise world-widely awareness, it is important to trace their intracellular performances, investigate their potential internalizations and uptake visualizations. The common applied approach is fluorescence-based trace, which required inevitable artificial labelled fluorescent probes, which may probably change physicochemical and pharmacological effects of RNA, and may cause problems like peak overlapping in complex bio-systems and photo-bleaching [29-31]. Alarmingly, labelling might also cause several problems such as lower biosafety and higher cost in practical applications. In that case, label-free delivery carrier materials are highly recommended for drug/ gene delivery. On the

contrary, Raman is great for biological based characterizations. Signals of Raman methods are easier to separate, as Raman spectra is finger-printed and photo-stable. Similar to fluorescence, traditional Raman trace also needs labels like Raman reporters to give the delivery system Raman-active capabilities.

Interestingly, g-C$_3$N$_4$ nanosheets have been proved having Raman-active features under near-infrared (NIR, 785 nm) light scattering [32-34], which makes them possible for using as label-free Raman traceable delivery carriers. Since single g-C$_3$N$_4$ materials could hardly loading siRNA, this design selected biocompatible low molecular weight branched polyethylenimine (PEI) and g-C$_3$N$_4$ to conjugate the siRNA delivery system. Low molecular weight polyethylenimine (PEI, ~ 800Da) is a well-known biocompatible component[35-38], so it is great to form non-toxic nanocarriers. In this study, low molecular weight PEI combined g-C$_3$N$_4$ nanosheets composites were synthesised, and used as a novel siRNA delivery system (**Scheme 5.1a**). Based on Raman-active features, the cellular uptake results of PEI-g-C$_3$N$_4$@siRNA composites can be directly obtained by non-invasive Raman spectroscopies (**Scheme 5.1b**).

5.2.3. Experimental Section

5.2.3.1. Chemicals and Reagents

Tris Acetate-EDTA (TAE) buffers, fetal bovine serum (FBS), Dulbecco's modified eagle medium (DMEM), antibiotic-antimycotic (Anti-anti, 100X), phosphate buffered saline (PBS, pH=7.4) and 3-(4,5-Dimethylthiazol-2-yl)-2,5-diphenyltetrazolium bromide (MTT) were purchased from Life Technologies Australia Pty Ltd. Human osteosarcoma cell line KHOS were purchased from American Type Culture Collection. N-(3-Dimethylaminopropyl)-N'-ethyl carbodiimide hydrochloride (EDC), Human Kinase PLK1 small interfering RNA (siRNA), oligo DNA with same quantity of the

bases of siRNA, agarose, branched polyethylenimine (PEI, M.W: ~ 800 Da), melamine (99%), dimethyl sulfoxide (DMSO), N-hydroxysuccinimide (NHS) N, N-dimethylformamide (DMF) and other chemicals were purchased from Sigma Aldrich. Concentrated sulfuric acid (H_2SO_4, 98.0%) and sodium hydroxide (NaOH, pellets) were purchased from Chem-Supply Australia Pty Ltd. All materials were of analytical grade and used as received without further purification. Millipore water was obtained from a three-stage Millipore Mill-Q plus 185 purified cation system (Academic) with a resistivity higher than 18.2 MΩ·cm.

5.2.3.2. Material Characterisation

A FEI Tecnai G2 Spirit transmission electron microscope at an acceleration voltage of 120 kV was employed to take transmission electron microscopy (TEM) images. Scanning electron microscopy (SEM) observations were carried out on a FEI Quanta 450 FEG environmental emission scanning electron microscope operated at 10 kV. A Malvern Zeta-sizer Nano ZS (Malvern Inst. Ltd, U.K.) equipment was used to measure the hydrodynamic sizes and zeta-potentials of different products dispersed in deionized water. Fourier transform infrared (FT-IR) spectra were collected at room temperature on a Thermo Scientific NICOLET 6700 FTIR spectrometer with a Diamond ATR (attenuated total reflection) crystal. The pH values were measured by a pH meter (EL20, MET-TLER TOLEDO). Atomic force microscope (AFM) data was processed by NT-MDT Ntegra Solaris Atomic Force Microscope, and the figures were produced by the Nova software. A Mettler Toledo Thermogravimetric Analyser with an air atmosphere (60 mL min-1) and a heating ramp of 20 ˚C min^{-1} was used for thermogravimetric analysis (TGA). A HORIBA Lab RAM HR Evolution equipped with 785 nm laser was employed for Raman spectrum and SERS mapping images

5.2.3.3. Preparation of Low Molecular Weight PEI conjugated g-C3N4 Nanosheets

The bulk graphitic carbon nitride (g-C3N4) powder was prepared by thermal condensation of melamine.[25] Melamine powder in a covered crucible was heated at 600 °C for 2 hours with a ramp rate of 3 °C min^{-1} in a muffle furnace. The obtained yellow product bulk g-C3N4 was grinded into fine powder for further use.

Acidified soluble g-C3N4 nanosheets was synthesised in large-scale preparation methods [39-41].1 g of bulk g-C3N4 powder was dissolved in 20 mL concentrated H2SO4 at 100 °C for 1 hour, as the colour of solution gradually transferred from yellow to clear pale yellow. The obtained solution was natural cooled before it carefully injected into 80 mL 70 °C ethanol under 1000 rpm stirring. The obtained white precipitate acidified g-C3N4 was filtered, washed repeatedly by deionized water and ethanol and dried at 60 °C. Graphite-phase layered g-C3N4 nanosheets was obtained after 2 hour sonication of 100 mg acidified g-C3N4 into 100 mL water.

After adjusted the pH value of g-C3N4 nanosheets suspension to 7 by NaOH, 50 mg EDC and 50 mg NHS was added into 10 mL the above suspension under stirring at room temperature. 1 h later, 1 mL 100 mg mL^{-1} 800 Da PEI was added into the suspension, and after another 24 h, PEI-g-C3N4 composites were centrifuged, washed repeatedly and re-dispersed in water for further use.

5.2.3.4. Binding Ability and Preparation of siRNA Delivery System

The binding ability of siRNA to PEI-g-C3N4 composites was investigated by agarose gel electrophoresis. An oligo DNA with same quantity of the bases of functional siRNA was employed as model gene for electrophoresis. Various weight of PEI-g-C3N4 composites and 0.2 μg model DNA were mixed at different weight ratios from 5:1 to 200:1 with naked model DNA and a real functional sample with PEI-g-C3N4 composites: siRNA weight ratio of 200: 1 as two controls. Gel loading dye blue was added in each sample, after 30 min incubation at

room temperature to form PEI-g-C_3N_4@siRNA composites. The resulting gene migration patterns were recorded by UV irradiation (G-BOX, SYNGENE), after the composites electrophoresed in TAE buffer through a gel red stained 0.8% agarose gel at 90 V for 60 min.

5.2.3.5. Cell Culture and Biocompatibility Studies

Human osteosarcoma cell line KHOS and human embryonic kidney cell line HEK 293 were incubated in cell growth medium (90% (v/v) DMEM, 10% (v/v) fetal bovine serum (FBS) and 1% Anti-anti) at 37 °C, 5% CO_2 and humidified atmosphere. Cell viabilities of PEI-g-C_3N_4 composites and cell cytotoxicities of PEI-g-C_3N_4 composites @ siRNA in every cell line were evaluated by MTT assay. KHOS and HEK 293 cells were seeded into a 96-well plate at a density of 5×10^4 cells mL^{-1}, and incubated in 100 μL cell culture medium for 24 h. After that, the previous medium was replayed by 100 μL of 1 μg mL^{-1} fresh cell culture medium containing different particles (PEI-g-C_3N_4 composites, PEI-g-C_3N_4 composites @ siRNA and free siRNA). After incubation for 24 h, 10 μL of 0.5 mg mL^{-1}MTT was added to each well and further incubated 4 h. Later, the medium in each well was replaced by 150 μL DMSO to dissolve formazan crystals. The MTT assays were conducted in quadruplicate for each sample, and the absorbance of formazan crystals was measured by an ELx808 Absorbance Microplate Reader (Biotek, USA) at 595 nm.

5.2.3.6. Cell Uptake Traced by Fluorescence and Raman Methods

Cellular uptake of PEI-g-C_3N_4@siRNA composites were observed with confocal laser scanning microscopy. KHOS cells were seeded at a density of 2×10^5 cells per well in 6-well plates with 2 mL growth medium and a cover glass (for fluorescence) or quartz slide (for Raman) inside each well. After cultured for 24 h, the medium was replaced by 1 mL of 1 μg mL^{-1} fresh medium containing PEI-g-C_3N_4@siRNA composites. After 4 h incubation, the glass or quartz slide with cells and composites were softly washed twice by PBS. The cellular uptake

by fluorescence visualization were obtained by a Leica Confocal 1P/FCS laser scanning microscope and cellular uptake by Raman mapping were collected by a HORIBA Lab RAM HR Evolution Raman laser scanning microscope.

5.2.4. Results and Discussion

5.2.4.1. Synthesis of PEI-g-C₃N₄ Composites and Characterization

As shown in **Figure S5.1**, acidified g-C$_3$N$_4$ were prepared by acidifying bulk g-C$_3$N$_4$ powder.[39-41]

Photographs (**Figure S5.1a**) and scanning electron microscopy (SEM, **Figure S5.2a**) demonstrate that bulk g-C$_3$N$_4$ is yellow powder-like amorphous materials. After acidifying, the yellow bulk materials could be soluble in acid, and finally formed nearly transparent suspension in ethanol (**Figure S5.1b to d**). SEM (**Figure S5.2b**) and transmission electron microscopy (TEM, **Figure S5.2d**) show that the morphology of acidified g-C$_3$N$_4$ is layered nanosheets with an average size of 80-120 nm. PEI-g-C$_3$N$_4$ composites were synthesized by low molecular weight branched polyethyleneimine (PEI, M.W: ~ 800 Da) grafted onto layered g-C$_3$N$_4$ nanosheets. As demonstrated in **Figure S5.2c** and **Figure 5.1a**, PEI-g-C$_3$N$_4$ composites are nanoscale sheet-like waved materials with an average size of 100-150 nm. The sizes were confirmed by dynamic light scattering, and the results show that the average hydrodynamic size of g-C$_3$N$_4$ nanosheets is 118.4 nm with zeta potential of -32.2 ± 1.5 mV, while the hydrodynamic size of PEI-g-C$_3$N$_4$ composites is 122.1 nm with an average zeta potential of 42.5 ± 0.1 mV (**Figure S5.3 and Table S5.1**). From g-C$_3$N$_4$ nanosheets to PEI-g-C$_3$N$_4$ composites, the morphologies and average sizes remain little change, but the surface zeta potentials transfer from negative to positive, which makes them available as gene delivery carriers.
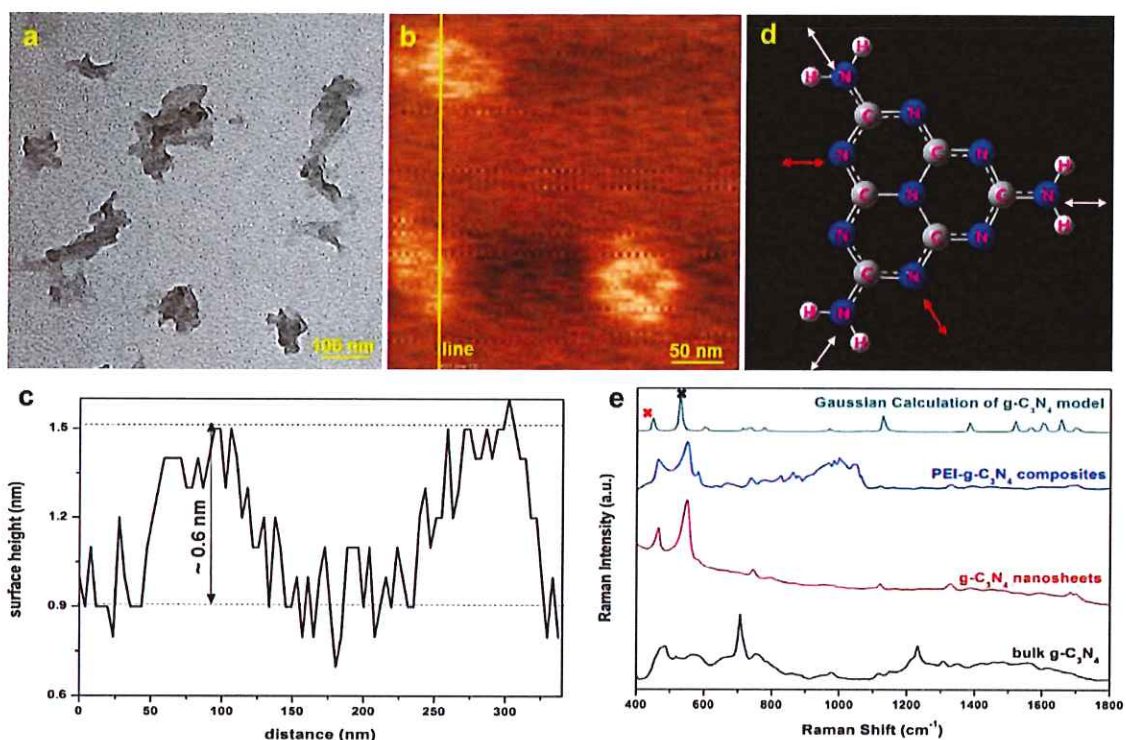
Figure 5.1 a) TEM image of PEI-g-C₃N₄ composites, b) AFM image of PEI-g-C₃N₄ with a randomly selected line, b) the g-C₃N₄ model for Gaussian calculations (arrows indicting the of 488 cm^{-1} (red) and 528 cm^{-1} (white) vibration directions), d) the surface height curve of PEI-g-C₃N₄, and e) Measured Raman spectra of bulk g-C₃N₄, g-C₃N₄ nanosheets and PEI-g-C₃N₄ composites with compared calculated Raman spectra of g-C₃N₄ model.

The atomic force microscopy with taping mode was also used to evaluate the size of PEI-g-C₃N₄ composites. As shown in **Figure 5.1c**, the sizes of composites are in a range of 80-120 nm with an average thickness around 0.6 nm. As g-C₃N₄ has graphite-like layered structure, and the distance between layers is about 3.3 nm [14, 25, 42], the synthesized PEI-g-C₃N₄ composites can be considered as single layered nanosheets.

FT-IR (**Figure S5.4a**) was used to verify the graphite-like structure of materials. The typical stretching vibration modes 1623, 1537, 1462, and 1410 cm^{-1} of heptazine-derived repeating units and the absorption peak at 803 cm^{-1} of the breathing mode of the triazine units can be observed in bulk g-C₃N₄, g-C₃N₄ nanosheets and PEI-g-C₃N₄ composites[39, 43, 44], which show

88

that graphite-like structure had not been destroyed during synthesis processes. The absorption peak at 1087 cm^{-1} can be attributed to -C–O stretching vibration, and the peak at 1710 cm^{-1} are representing the symmetric stretching of -C=O, which may be attributed to the hydrolysis and oxidation of g-C$_3$N$_4$ and confirm the presence of carboxyl groups. Peaks around 3000-3500 cm^{-1} can be attributed to N–H stretching vibrations.

As shown in **Figure S5.4b**, a fluorescence peak centred at 445 nm can be noticed when g-C$_3$N$_4$ nanosheets excited at 350 nm, which is similar to the photoluminescence intensity peak in pervious literatures[24, 25, 44]. In addition, the strong fluorescence peak centred at 401 nm of PEI-g-C$_3$N$_4$ composites was obtained by 300 nm excitation. The results show that both g-C$_3$N$_4$ nanosheets and PEI-g-C$_3$N$_4$ composites have photoluminescence properties, and the strong fluorescent PEI-g-C$_3$N$_4$ composites may be attributed to the single layered structure.

The thermogravimetric analysis result (TGA) was another evidence of successfully grafted PEI onto g-C$_3$N$_4$ nanosheets. As demonstrated in **Figure S5.5**, the weight loss percentages from 25 to 500 °C of 800 Da PEI, PEI-g-C$_3$N$_4$ composites and g-C$_3$N$_4$ nanosheets are 77.7, 27.5 and 21.5%. Pure 800 Da branched PEI starts losing weight around 200 °C, and g-C$_3$N$_4$ nanosheets demonstrate slight weight loss during the calcination processes. The weight loss of PEI-g-C$_3$N$_4$ composites is greater than g-C$_3$N$_4$ nanosheets, which prove the existence of PEI.

Raman measurements (**Figure 5.1e**) were taken under a 785 nm excitation laser. For bulk g-C$_3$N$_4$ powder, Raman peaks centred at 707 and 980 cm^{-1} can be attributed to different types of s-triazine ring breathing modes[33]. However, this two peaks are not obvious in Raman spectrum of g-C$_3$N$_4$ nanosheets. To investigate the Raman spectrum of nanosheets, a g-C$_3$N$_4$ model with a tri-s-triazine (melem) unit (**Figure 5.1d**) was constructed. The Raman activity spectrum of this model was theoretically calculated by a Gaussian 09 software. The results (**Figure 5.1e** and **Figure S5.8**) show g-C$_3$N$_4$ model have two dominated Raman peaks centred at 448 and 528 cm^{-1}, which represent bending (red arrows in **Figure 5.1d**) and stretching (white arrows in

89

Figure 5.1d) vibrations of the model. The animated video of these vibrations are demonstrated in **supporting information video 1 and 2**. For real tested Raman spectra of g-C_3N_4 nanosheets and PEI-g-C_3N_4 composites, two Raman peaks centred around 448 and 528 cm^{-1} can be clearly observed in **Figure 5.1e**. As 528 cm^{-1} Raman peak has high intensity in the Raman shift range of 400-1800 cm^{-1}, it is selected as the signal for Raman mapping trace.
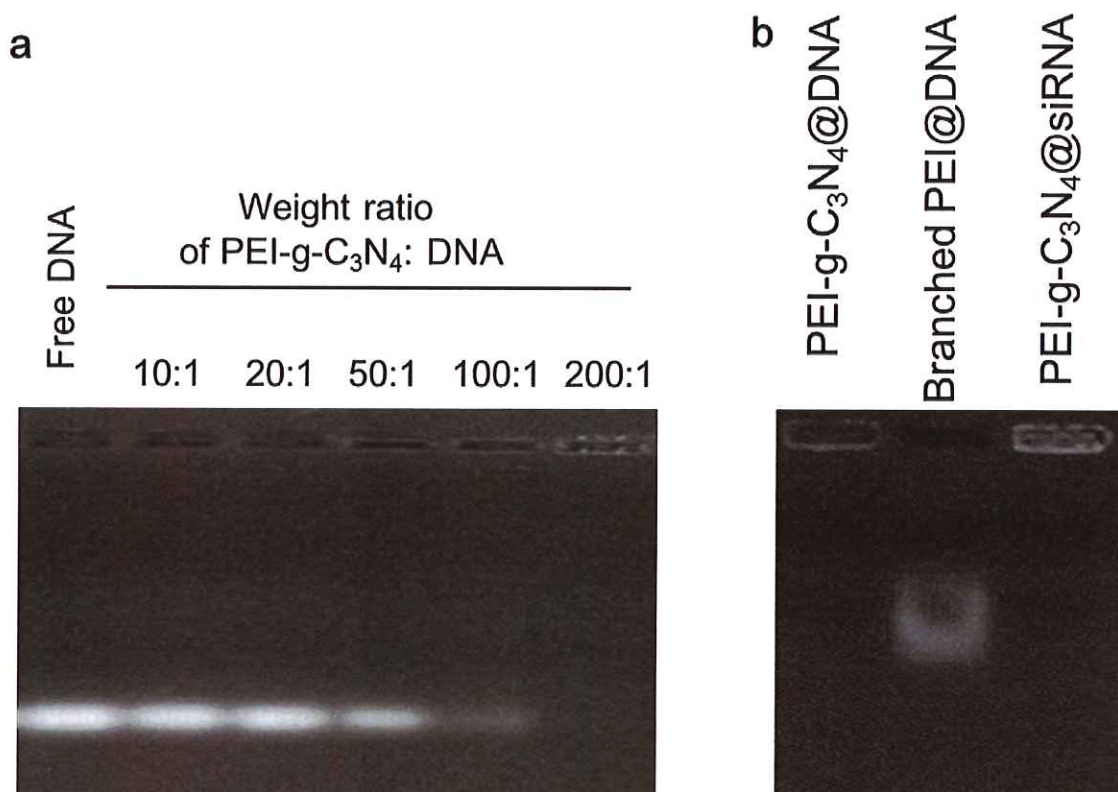

Figure 5.2. a) Gene binding capability of PEI-g-C_3N_4 composites with different composites to model DNA ratios and b) binding capability of same 200:1 weight ratio of PEI-g-C_3N_4 @DNA composites, 800 Da branched PEI@DNA and the PEI-g-C_3N_4 @siRNA composites.

5.2.4.2. Binding Capabilities of siRNA Delivery System

Agarose gel electrophoresis was used to evaluate the binding ability of delivery carriers. A model DNA with same quantity of the bases of functional siRNA was used to instead expensive

siRNA, and the weight ratio of delivery carriers to model DNA increased from 10 to 200. For g-C$_3$N$_4$ nanosheets, the brightness of escaped DNA remain similar with the increase of weight ratio, which indicates g-C$_3$N$_4$ nanosheets have weak binding abilities (**Figure S5.6**). While PEI-g-C$_3$N$_4$ composites show good binding capability of gene, as the brightness of escaped DNA decrease and thoroughly disappear at weight ratio 200, which may be attributed to completely binding DNA (**Figure 5.2a**). **Figure 5.2b** illustrates the binding capabilities of various samples at the above complete binding weight ratio 200. Low molecular weight branched PEI themselves cannot thoroughly bind gene, as the escaped model DNA can be observed. Neither g-C$_3$N$_4$ nanosheets nor Low molecular weight PEI has great gene binding abilities, but PEI-g-C$_3$N$_4$ composites show good binding abilities of both model DNA and real functional siRNA.
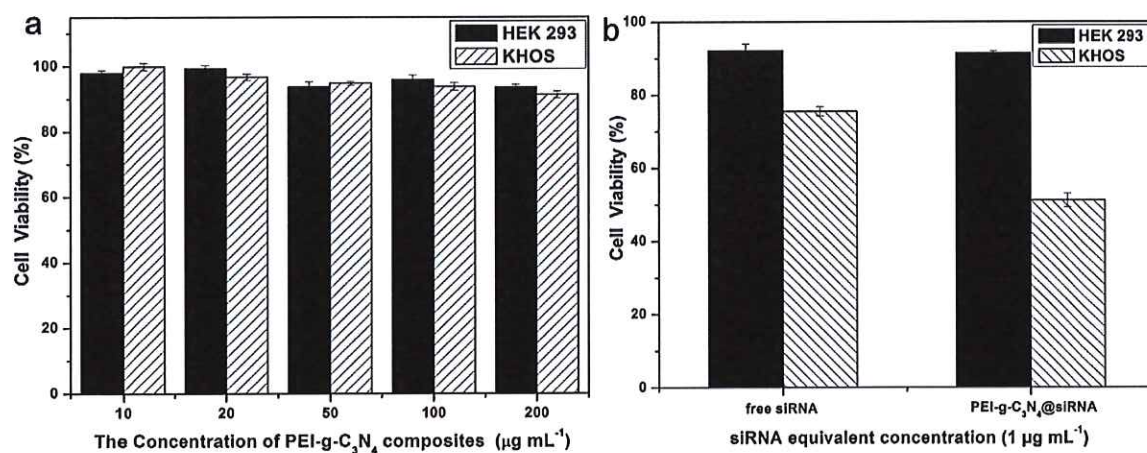
Figure 5.3. a) Biocompatibility of PEI-g-C$_3$N$_4$ composites and b) cytotoxicities of 1μg mL^{-1} equivalent concentration of free siRNA and PEI-g-C$_3$N$_4$ @ siRNA against HEK 293 and KHOS cell lines.

5.2.4.3. Biocompatibilities and Cytotoxicities Studies

Biocompatibilities of PEI-g-C$_3$N$_4$ composites were investigated by 3-(4,5-dimethylthiazol-2-yl)-2,5-diphenyltetrazolium bromide (MTT) assays against human osteogenic sarcoma

(KHOS) and human embryonic kidney (HEK 293) cell lines within material concentration range from 10 to 200 μg mL^{-1}. In **Figure 5.3a**, cell viabilities remain above 85% at high concentration 200 μg mL^{-1}, which means PEI-g-C$_3$N$_4$ composites have good biocompatibilities in both cancer and normal cell lines.

Based on the complete binding weight ratio 200, cytotoxicities of free siRNA and PEI-g-C$_3$N$_4$ composites @ siRNA were also investigated by MTT assays against KHOS and HEK 293 at 1 μg mL^{-1} siRNA equivalent concentration. As demonstrated in **Figure 5.3b**, free siRNA and PEI-g-C$_3$N$_4$ composites @ siRNA have no obvious cytotoxicity in HEK 293 cells, but show clear cytotoxicity in KHOS cells with cell viabilities around 75 and 50%. By comparison, the delivery system PEI-g-C$_3$N$_4$ composites @ siRNA has greater cytotoxicity in KHOS cells than free siRNA.

5.2.4.4. Raman Traced Cellular Uptake

Since the designed PEI-g-C$_3$N$_4$ composites @ siRNA delivery systems have Raman-active properties, their cellular uptake performances after 4 h incubations in the KHOS cells were traced Raman methods without artificial labels.

Fluorescence trace was also conducted as comparing experiments (**Figure S5.7**). The fluorescence results are demonstrated in low magnitude (**a-c**) and high magnitude (**d-f**). In optical images (**Figure S5.7a and d**), healthy morphologies of KHOS cells can be observed. With the limitation of instruments, the blue self-fluorescence trace pattern of delivery system was obtained under 405 nm excitation, which may cause low collections of fluorescence signals. That may be the reasons that the cellular uptakes of PEI-g-C$_3$N$_4$ composites, which are shown as the brightness of blue colour in fluorescence-traced images, can hardly observed from low magnitude image (**Figure S5.7b**). In high magnitude image (**Figure S5.7e**), the existences of PEI-g-C$_3$N$_4$ composites could be verified, but they are not shown clear cell morphologies. are

the merged images **Figure S5.7c and f** show that high brightness of blue colour are inside KHOS cells, which demonstrating these fluorescent delivery systems really delivery into cells at traced time point, but low blue brightness caused by noises signals can also be seen in the traced images. Although these PEI-g-C_3N_4 composites could be traced by fluorescence, the traced results can hardly show clear cell uptake images and influenced by the cell background noises.
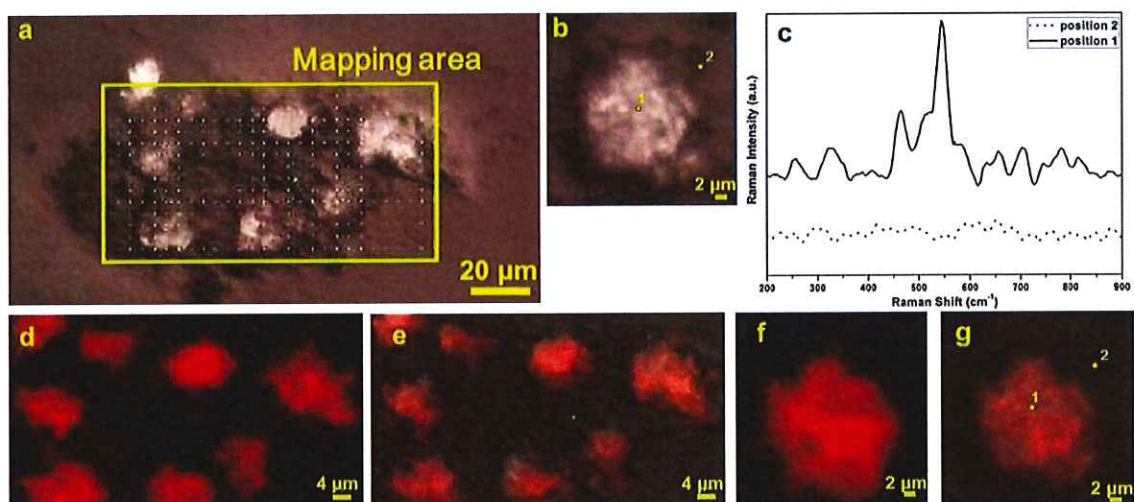
Figure 5.4. Raman mapping images of PEI-g-C_3N_4 composites @ siRNA with a) low magnitude and b) single cell scale with 2 points, c) Raman spectra of two selected positions 1 and 2, d, f) Raman mapping image, and e, g) merged images.

Figure 5.4 are the low magnitude (several cells, **a, d, e**) and high magnitude (single cell, **b, f, g**) Raman tracing results of PEI-g-C_3N_4 composites @ siRNA delivery systems under 785 nm excitation laser. **Figure 5.4c** shows the compared Raman spectra of position 1 in cell region and position 2 in substrate. The dominated Raman peak centred around 550 cm^{-1} can be clearly noticed. In **Figure 5.4d and f**, the traced pattern can demonstrate clear cell morphologies with different red brightness representing different uptake amount of delivery systems, and dark backgrounds also show little influenced on Raman trace. As Raman peaks are finger-print

93

bands with high sensitivities, Raman traced images are of higher resolutions and sensitivities with little affected background noises, compared with fluorescence ones (**Figure S5.7**). The Raman method could possibly replace widely implemented fluorescence in tracing, and these designed PEI-g-C_3N_4 composites make it possible to direct trace without further labelling.

5.2.5. Conclusion

Novel designed low molecular weight branched PEI and almost single-layer g-C_3N_4 nanosheets composite gene delivery systems with 100-150 nm in sheet sizes and 0.6 nm in thicknesses were successfully used as Raman traceable gene carriers for the first time. Low molecular weight branched PEI components with good cellular biocompatibilities are aimed to change the zeta potentials of the system from negative to positive and offer the system higher siRNA binding capabilities than 800 Da PEI themselves. The uniform layered g-C_3N_4 nanosheets, which form the main part of delivery carriers, provide the system with high degree of surface functionalities to conjugate PEI functional groups and with Raman-active features that contributes to target direct-Raman tracing of the system without artificial labels. Raman tracing shows several competitive advantages over fluorescence like higher resolution and low signal to noise ratio, which makes it as a better method for real-time uptake visualizations and the intracellular performances tracing of delivery system.

5.2.6. Supporting Information

Graphitic Carbon Nitride Composites: Label-free Direct Raman Traceable siRNA Delivery System
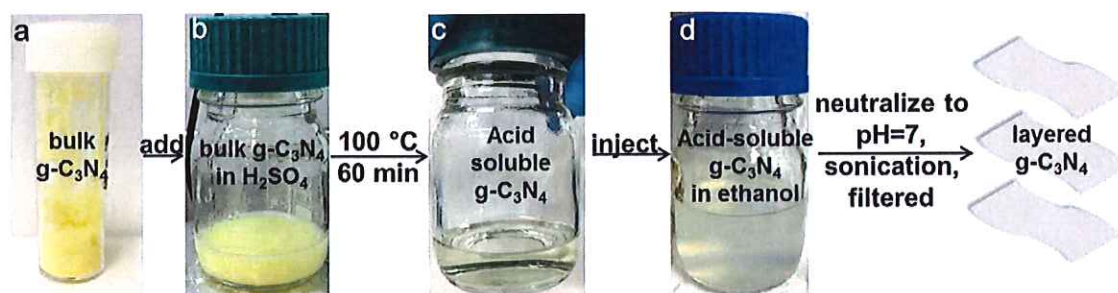
Figure S5.6. Synthesis process of acidified layered g-C$_3$N$_4$ nanosheets and photographs of a) bulk g-C$_3$N$_4$ powder, b) g-C$_3$N$_4$ powder in H$_2$SO$_4$ before reaction, c) acidified g-C$_3$N$_4$ nanosheets soluble in H$_2$SO$_4$ after reaction and d) suspension of acid-soluble g-C$_3$N$_4$ nanosheets in ethanol.
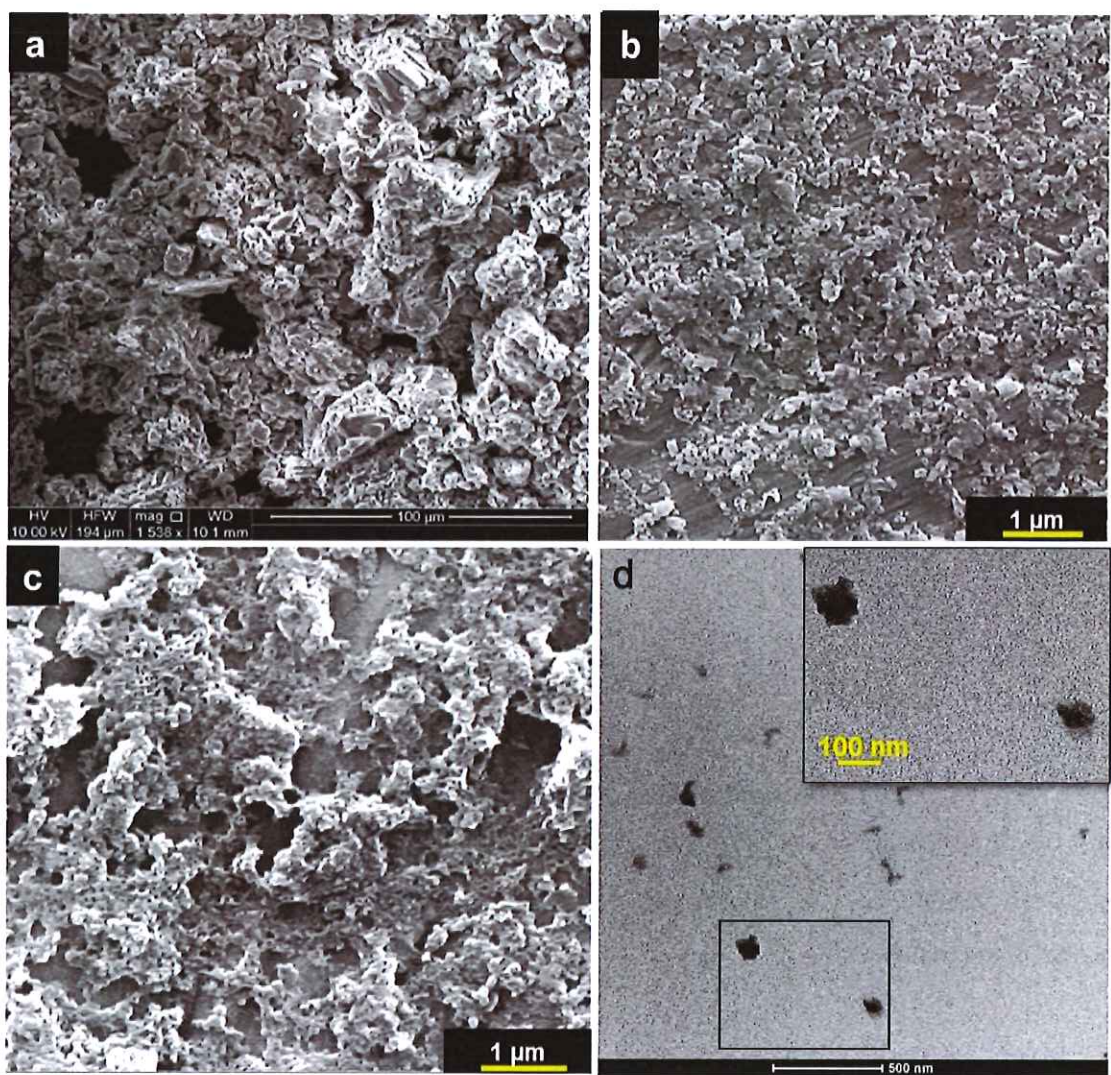
Figure S5.2. SEM images of a) bulk g-C$_3$N$_4$ powder, b) layered g-C$_3$N$_4$ nanosheets, c) PEI-g-C$_3$N$_4$ composites and d) TEM image of layered g-C$_3$N$_4$ nanosheets with enlarged one inset.
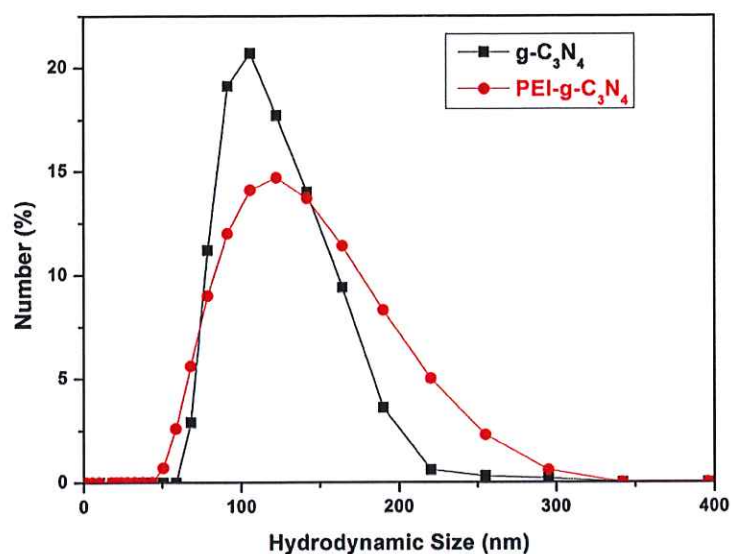
Figure S5.3. Hydrodynamic size distributions of g-C₃N₄ nanosheets and PEI-g-C₃N₄ composites in water at pH 7.
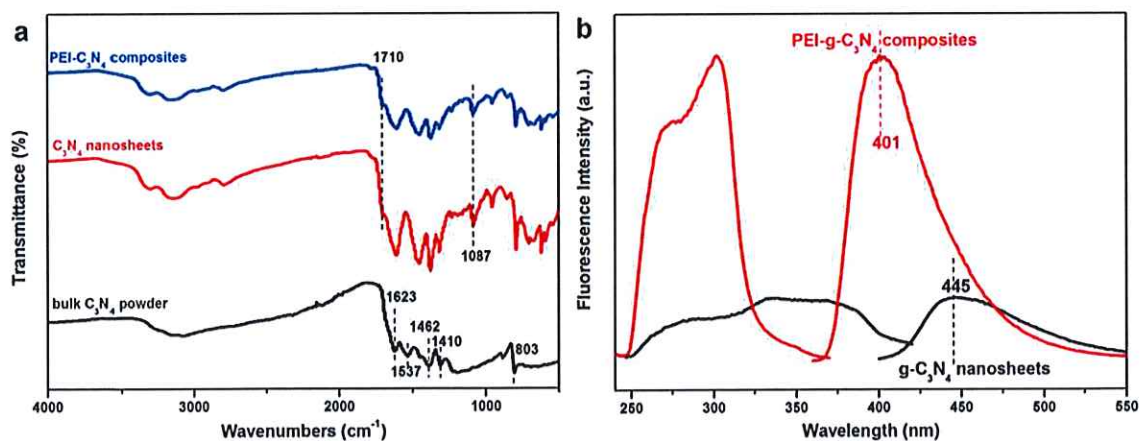
Figure S5.4. a) FT-IR of bulk g-C₃N₄ powder, g-C₃N₄ nanosheets and PEI-g-C₃N₄ composites, and b) Fluorescence excitation and emission spectra of g-C₃N₄ nanosheets and PEI-g-C₃N₄ composites.
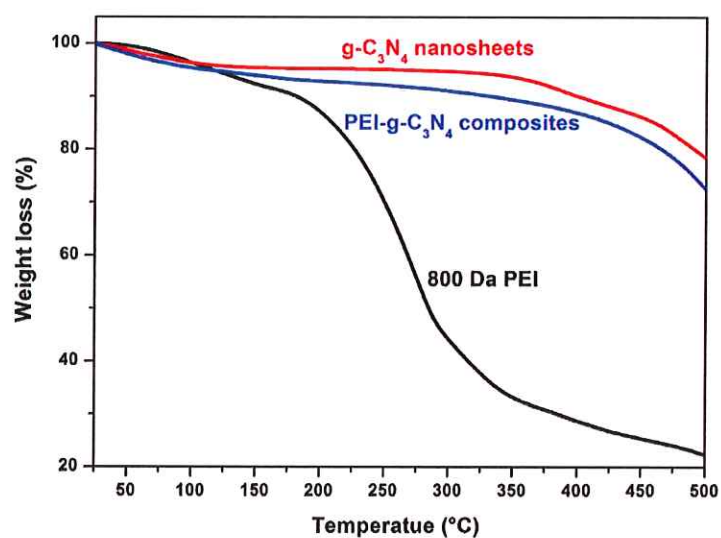
Figure S5.5. TGA curves of the calcination processes of 800 Da branched PEI, g-C$_3$N$_4$ nanosheets and PEI-g-C$_3$N$_4$ composites.
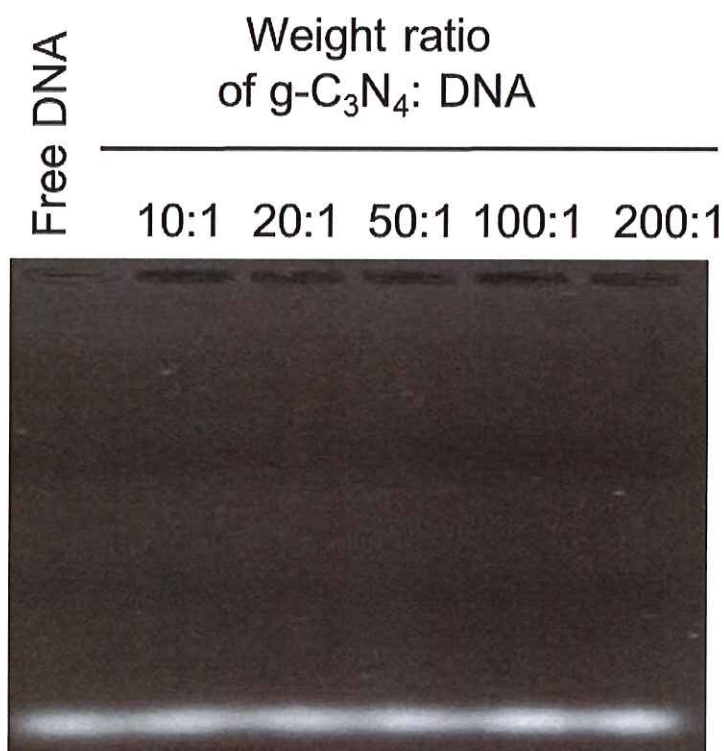
Figure S5.6. Agarose gel electrophoresis indicating the capabilities of g-C$_3$N$_4$ nanosheets binding model DNA from materials to DNA weight ratio 10 to 200.
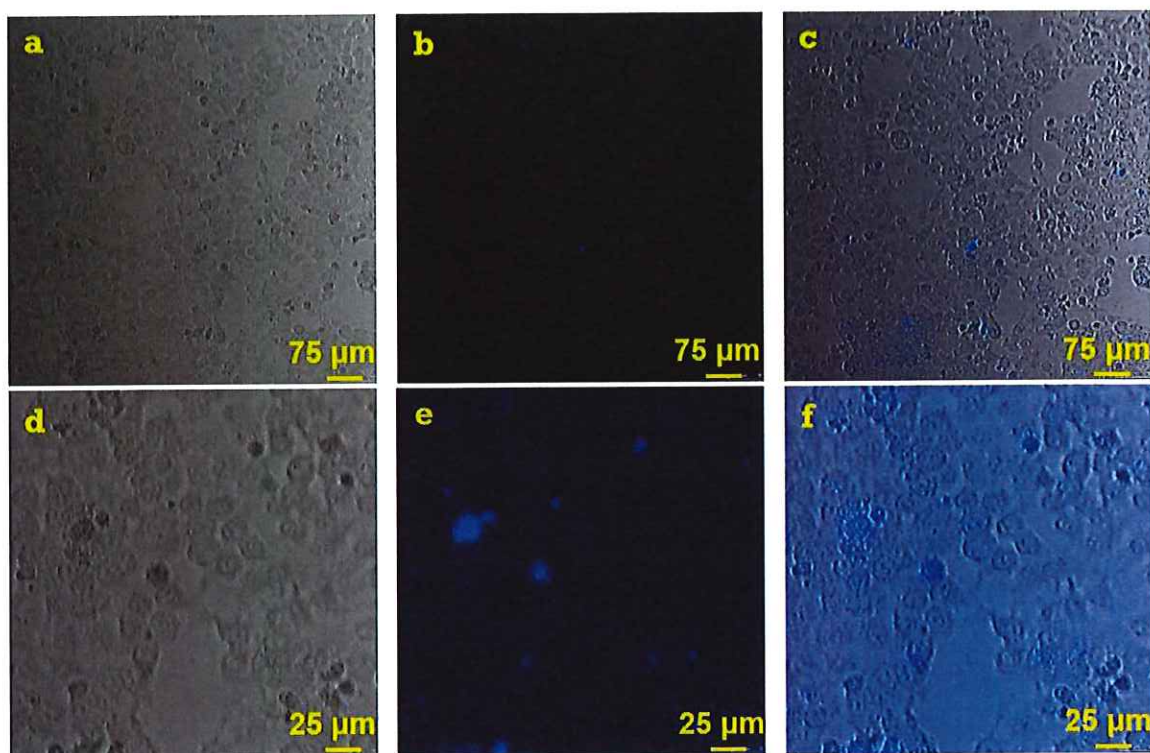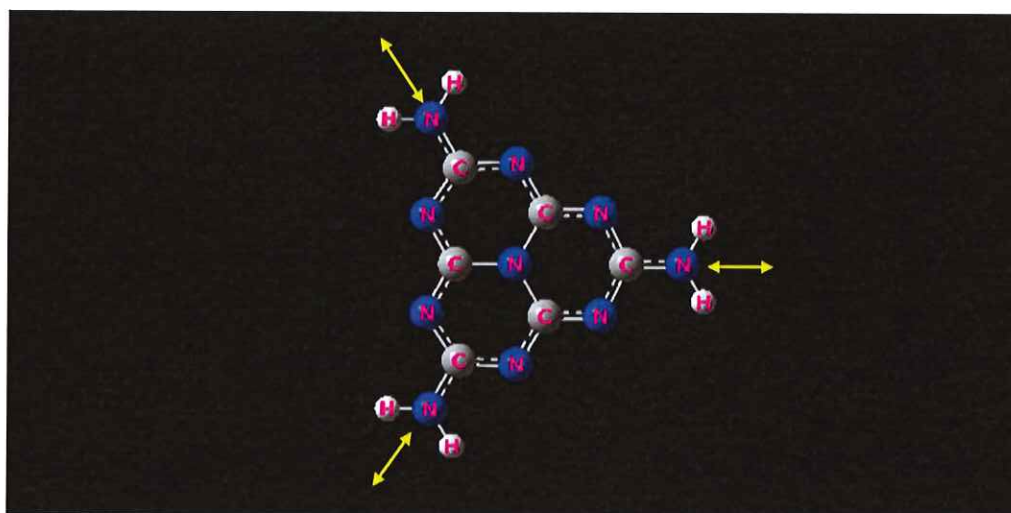
Figure S5.7. Fluorescence images of PEI-g-C$_3$N$_4$ @siRNA composites with low magnitude (a-c) and high magnitude (d-f), a, d) optical images, b, e) fluorescence images and c, f) merged images.
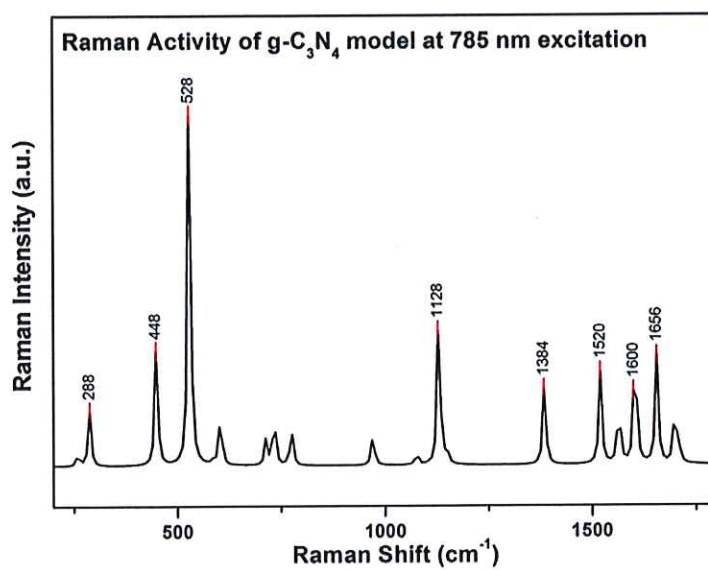
Figure S5.8. The calculated Raman activity of g-C$_3$N$_4$ model at 785 nm incident light.
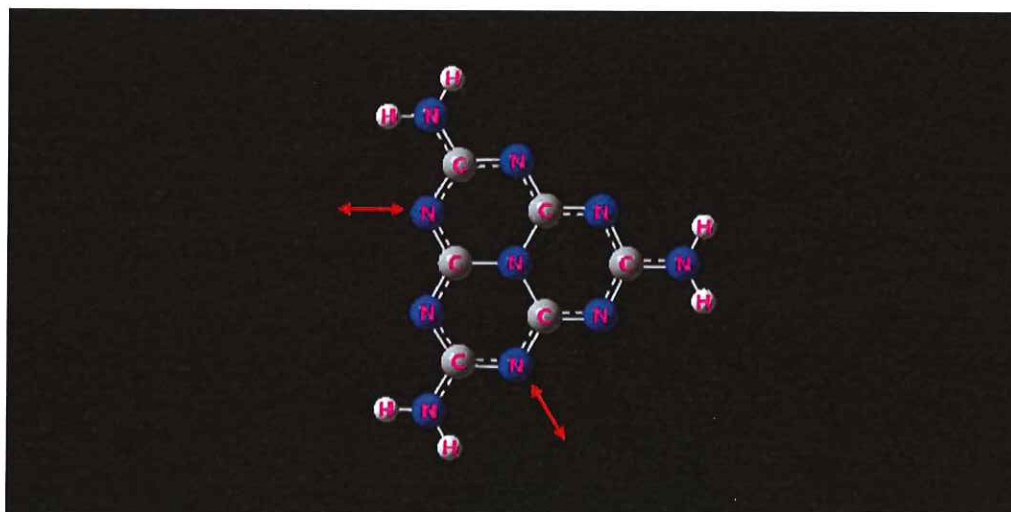
Figure S5.9. The vibrations of g-C_3N_4 model at 448 cm^{-1}Raman shift with arrows show the directions of vibrations.

Figure S5.10 The vibrations of g-C_3N_4 model at 528 cm^{-1}Raman shift with arrows show the directions of vibrations.

Table S5.1. Hydrodynamic sizes and zeta potential of g-C$_3$N$_4$ nanosheets and PEI-g-C$_3$N$_4$ composites measured at pH=7.

Sample Name	PDI	Hydrodynamic Size [nm]	Zeta Potential [mV])
g-C$_3$N$_4$	0.25	118.4	-32.2 ± 1.5
PEI-g-C$_3$N$_4$	0.46	122.1	42.5 ± 0.1

5.2.7. Acknowledgements

5.2.8. Reference

[1] J.-M. Kim, E. Shin, S.-M. Ryou, J.-H. Yeom, K. Lee, Biotechnology and Bioprocess Engineering 2013, 18, 637.

[2] Y. S. Choi, M. Y. Lee, A. E. David, Y. S. Park, Molecular & Cellular Toxicology 2014, 10, 1.

[3] Q. Yin, J. Shen, Z. Zhang, H. Yu, Y. Li, Advanced Drug Delivery Reviews 2013, 65, 1699.

[4] M. S. Shim, Y. J. Kwon, Advanced Drug Delivery Reviews 2012, 64, 1046.

[5] S. Ganta, H. Devalapally, A. Shahiwala, M. Amiji, Journal of Controlled Release 2008, 126, 187.

[6] I. M. Verma, M. D. Weitzman, Annual Review of Biochemistry 2005, 74, 711.

[7] A. de Fougerolles, H.-P. Vornlocher, J. Maraganore, J. Lieberman, Nat Rev Drug Discov 2007, 6, 443.

[8] Y. Chen, C. Tan, H. Zhang, L. Wang, Chemical Society Reviews 2015, 44, 2681.

[9] D. Chimene, D. L. Alge, A. K. Gaharwar, Advanced Materials 2015, 27, 7261.

[10]   R. Kurapati, K. Kostarelos, M. Prato, A. Bianco, Advanced Materials 2016, 28, 6052.

[11]   Z. Chengzhou, D. Dan, L. Yuehe, 2D Materials 2015, 2, 032004.

[12]   M. Xiong, Q. Rong, H.-m. Meng, X.-b. Zhang, Biosensors and Bioelectronics 2017, 89, Part 1, 212.

[13]   L. Gong, L. Yan, R. Zhou, J. Xie, W. Wu, Z. Gu, Journal of Materials Chemistry B 2017, 5, 1873.

[14]   X. Wang, K. Maeda, A. Thomas, K. Takanabe, G. Xin, J. M. Carlsson, K. Domen, M. Antonietti, Nat Mater 2009, 8, 76.

[15]   Y. Zhang, A. Thomas, M. Antonietti, X. Wang, Journal of the American Chemical Society 2009, 131, 50.

[16]   J. Zhang, X. Chen , K. Takanabe, K. Maeda, K. Domen, J. D. Epping, X. Fu, M. Antonietti, X. Wang Angewandte Chemie International Edition 2010, 49, 441.

[17]   S. Cao, J. Low, J. Yu, M. Jaroniec, Advanced Materials 2015, 27, 2150.

[18]   T. Y. Ma, S. Dai, M. Jaroniec, S. Z. Qiao, Angewandte Chemie International Edition 2014, 53, 7281.

[19]   J. Duan, S. Chen, M. Jaroniec, S. Z. Qiao, ACS Nano 2015, 9, 931.

[20]   P. Niu, L. Zhang, G. Liu, H.-M. Cheng, Advanced Functional Materials 2012, 22, 4763.

[21]   S. Yang, Y. Gong, J. Zhang, L. Zhan, L. Ma, Z. Fang, R. Vajtai, X. Wang, P. M. Ajayan, Advanced Materials 2013, 25, 2452.

[22]   A. Thomas, A. Fischer, F. Goettmann, M. Antonietti, J.-O. Muller, R. Schlogl, J. M. Carlsson, Journal of Materials Chemistry 2008, 18, 4893.

[23]   B. Jürgens, E. Irran, J. Senker, P. Kroll, H. Müller, W. Schnick, Journal of the American Chemical Society 2003, 125, 10288.

[24]   M.-H. Xiang, J.-W. Liu, N. Li, H. Tang, R.-Q. Yu, J.-H. Jiang, Nanoscale 2016, 8, 4727.

[25]   X. Zhang, X. Xie, H. Wang, J. Zhang, B. Pan, Y. Xie, J Am Chem Soc 2013, 135, 18.

[26]   L.-S. Lin, Z.-X. Cong, J. Li, K.-M. Ke, S.-S. Guo, H.-H. Yang, G.-N. Chen, Journal of Materials Chemistry B 2014, 2, 1031.

[27]   C. G. Liu, X. T. Wu, X. F. Li, X. G. Zhang, Rsc Advances 2014, 4, 62492.

[28] X. Zhang, H. Wang, H. Wang, Q. Zhang, J. Xie, Y. Tian, J. Wang, Y. Xie, Advanced Materials 2014, 26, 4438.

[29] A. Samanta, K. K. Maiti, K.-S. Soh, X. Liao, M. Vendrell, U. S. Dinish, S.-W. Yun, R. Bhuvaneswari, H. Kim, S. Rautela, J. Chung, M. Olivo, Y.-T. Chang, Angewandte Chemie International Edition 2011, 50, 6089.

[30] N. M. S. Sirimuthu, C. D. Syme, J. M. Cooper, Analytical Chemistry 2010, 82, 7369.

[31] G. Han, C.-C. You, B.-j. Kim, R. S. Turingan, N. S. Forbes, C. T. Martin, V. M. Rotello, Angewandte Chemie International Edition 2006, 45, 3165.

[32] S. Tonda, S. Kumar, S. Kandula, V. Shanker, Journal of Materials Chemistry A 2014, 2, 6772.

[33] P. V. Zinin, L.-C. Ming, S. K. Sharma, V. N. Khabashesku, X. Liu, S. Hong, S. Endo, T. Acosta, Chemical Physics Letters 2009, 472, 69.

[34] J. Wang, R. Liu, C. Zhang, G. Han, J. Zhao, B. Liu, C. Jiang, Z. Zhang, RSC Advances 2015, 5, 86803.

[35] X. Du, B. Shi, Y. Tang, S. Dai, S. Z. Qiao, Biomaterials 2014, 35, 5580.

[36] M. P. Xiong, M. Laird Forrest, G. Ton, A. Zhao, N. M. Davies, G. S. Kwon, Biomaterials 2007, 28, 4889.

[37] C. Hu, Q. Peng, F. Chen, Z. Zhong, R. Zhuo, Bioconjugate Chemistry 2010, 21, 836.

[38] S. Yun‑Xia, Z. Xian‑Zheng, C. Han, C. Si‑Xue, Z. Ren‑Xi, Journal of Biomedical Materials Research Part A 2008, 84A, 1102.

[39] X. Du, G. Zou, Z. Wang, X. Wang, Nanoscale 2015, 7, 8701.

[40] L. Xiong, X. Du, F. Kleitz, S. Z. Qiao, Small 2015, 11, 5919.

[41] Z. Zhou, J. Wang, J. Yu, Y. Shen, Y. Li, A. Liu, S. Liu, Y. Zhang, Journal of the American Chemical Society 2015, 137, 2179.

[42] M. Groenewolt, M. Antonietti, Advanced Materials 2005, 17, 1789.

[43] J. Zhang, M. Zhang, L. Lin, X. Wang, Angewandte Chemie International Edition 2015, 54, 6297.

[44] C. Liu, Z. Chen, Z. Wang, W. Li, E. Ju, Z. Yan, Z. Liu, J. Ren, X. Qu, Nanoscale 2016, 8, 12570.

Chapter 6 Advanced Label-free Graphitic Carbon Nitride Nanocarriers for Traced Delivery

6.1. Introduction, Significance and Commentary

Two-dimensional graphitic carbon nitride (g-C$_3$N$_4$) materials of tunable large band-gaps and good fluorescence properties have been regarded as one of suitable carriers for fluorescence-based bio-imaging and tracing applications. In order to investigate and find out whether g-C$_3$N$_4$ can be used for surface enhanced Raman scattering (SERS) imaging applications or for smart fluorescence imaging, g-C$_3$N$_4$ carriers with two advanced modifications have been designed. The highlights of this work include:

1. Extend the application of g-C$_3$N$_4$ materials from spontaneous Raman to SERS imaging

    By further modification of small gold nanoparticles on the surface of g-C$_3$N$_4$, the new structured materials can be used as SERS traceable nanocarriers, and it is evident that the strength of Raman signal can be enhanced up to 4.57×10^5 times.

2. Transfer g-C$_3$N$_4$ materials from two dimension to three dimension and form smart fluorescence nanocarriers

    As glutathione (GSH) concentration in cytosol and the cell nucleus is quite higher than those in body fluids like blood, while GSH concentration in cancer cells is higher than normal healthy cells. In addition, GSH can cut the disulfide bond into thiol groups. The designed disulfide bond cross-linked g-C$_3$N$_4$ nanocomposites might be separated into g-C$_3$N$_4$ nanosheets in the cancer cells. As single layer g-C$_3$N$_4$ has higher strength fluorescence signals than those of the cross-linked g-C$_3$N$_4$ nanocomposites, the designed cross-linked g-C$_3$N$_4$ nanocomposites could show different imaging pattern between healthy and cancer cells.

6.2. Advanced Label-Free g-C₃N₄ Composite Traceable Nanocarriers for Bio-Imaging and Traceable Delivery Applications

This section is included in the thesis as it appears as an unpublished and unsubmitted work written in manuscript style.

6.2.1. Abstract

Advanced label-free g-C$_3$N$_4$ composite nanocarriers were designed for surface enhanced Raman scattering (SERS) imaging applications and smart three-dimensional nanocarriers for fluorescence imaging applications. By modification of small gold nanoparticles on ultrathin PEI-g-C$_3$N$_4$ nanosheets, the spontaneous Raman intensity of g-C$_3$N$_4$ can be enhanced up to 5 orders of magnitude, which makes it possible for high sensitive SERS imaging. As glutathione (GSH) concentration in cytosol and the cell nucleus is quite higher than those in body fluids like blood, while GSH concentration in cancer cells is higher than normal healthy cells. By using redox-sensitive non-fluorescent cross-linker to form three-dimensional cross-linked g-C$_3$N$_4$ (CL-g-C$_3$N$_4$) nanocomposites, the fluorescence imaging can be specific and show selectivity between healthy and cancer cells.

6.2.2. Introduction

Since the successfully isolation and investigation of the graphene, which won the 2010 Nobel Prize, was reported, two-dimensional materials (2DMs) with unique optical, electrical and thermal features have attracted the world-wide research interests[1-3]. It is evident that the large surface area of mesopores highly contribute to efficient cargo loading[4], as 2DMs with ultrathin thickness and two dimensional morphologies provide ultrahigh surface-area for loading and adsorbing guest cargos. 2DMs could be ideal carriers for drug/gene delivery system. So far, 2DMs such as layered double hydroxides (LDHs)[5], ultra-thin black phosphorous (BP)[6, 7],

105

graphic carbon nitride (g-C$_3$N$_4$)[8-10], hexagonal boron nitride[11] and transition metal dichalcogenides like MoS$_2$[12] and WS$_2$[13] have been used in numerous bio-applications including antimicrobial activity, tissue engineering, bio-sensing, bio-imaging and tracing delivery applications.

Among those materials, g-C$_3$N$_4$ has promising water dispersibility without further surfactants or oxidation treatments, and that is why it can be easily direct-exfoliated in aqueous solutions like water.[8, 14] In addition, g-C$_3$N$_4$ also hold great features like small sheet size, high hydrophilicity and low toxicity, which makes it as a wonderful material for forming delivery vehicles. Water-dispersed exfoliated g-C$_3$N$_4$ nanosheets with pH-dependent photoluminescence (PL) was reported as fluorescence nanocarriers for imaging within HeLa cells[10]. Ultrathin g-C$_3$N$_4$ nanosheets were fabricated and reported as nanocarriers for anticancer drug (doxorubicin, Dox) delivery and photodynamic therapy[8]. Single-layered biocompatible g-C$_3$N$_4$ quantum dots (QDs) were introduced to two-photon fluorescence imaging applications, for it has large two-photon absorption, high photo-stability and great photo-thermal effects[15]. Consequently, g-C$_3$N$_4$ of tunable large band-gaps and good fluorescence properties have been proved as suitable carriers for fluorescence-based bio-imaging and tracing applications.

In order to investigate the potential cytotoxicity of these very small inorganic g-C$_3$N$_4$ nanocarriers, the bio-imaging and carrier visualization studies have been put on the researchers' agenda. In our previous work, a kind of ultrathin PEI-g-C$_3$N$_4$ nanosheets has been synthesised and confirmed that they have fluorescent and Raman-active properties, so it can be used for spontaneous Raman imaging.

In order to investigate and find out whether g-C$_3$N$_4$ can be used for other bio-imaging applications or synthesis smart nanocarriers for fluorescence imaging, g-C$_3$N$_4$ carriers with two advanced modifications were designed in this work. The first one was coating small gold

nanoparticles on the surface of PEI-g-C₃N₄ nanosheets, which formed SERS tags. The second one was combined several PEI-g-C₃N₄ nanosheets by non-fluorescent disulfide cross-linker to construct a three dimensional structure, which is great for endocytosis, the major cellular uptake mechanisms for pharmaceutics, and it is also a simulation to form static fluorescence quenching and recovered design model. Cytosol and the cell nucleus have a high redox potential with glutathione (GSH) concentrations ranging from 2 to 10 mM, while body fluids like blood and normal extracellular matrices possess a low reducing power with GSH concentration as low as $2 - 20$ μM[16-20]. In addition, GSH concentration in cancer cells is higher than normal healthy cells. Based on thiol-disulfide exchange reaction, the disulfide bond can be cleaved into thiol by GSH[16-18]. As shown in **Scheme 6.1**, the synthesised three dimensional g-C₃N₄ nanocomposites could possibly be separated into single layered nanosheets in cell cytosol.
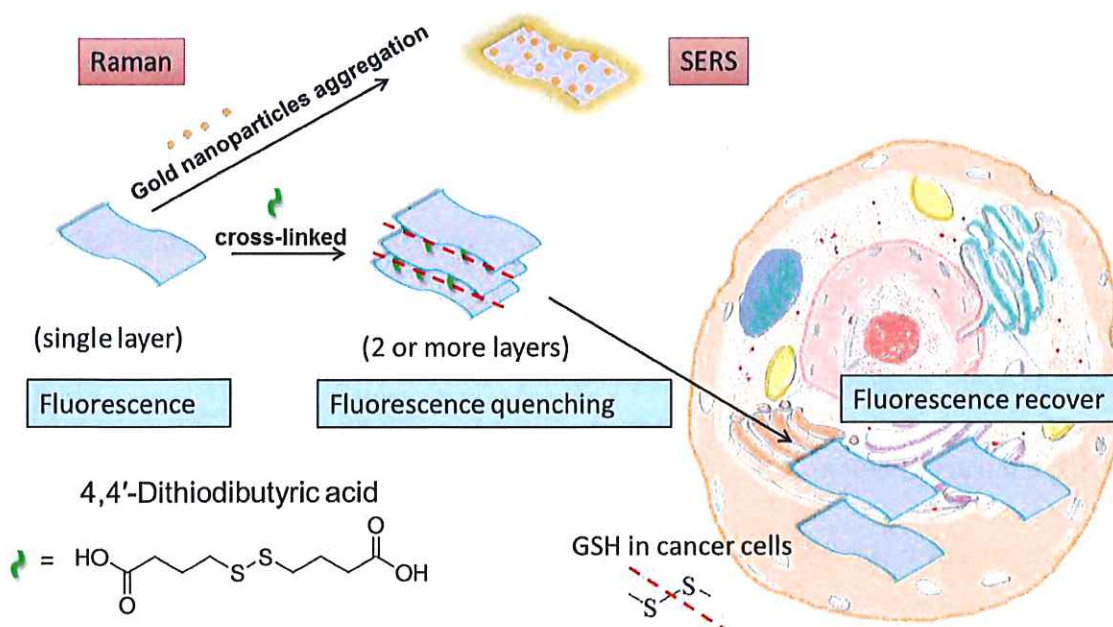
Scheme 6.1 Advanced g-C₃N₄ composites (Au-PEI-g-C₃N₄ nanosheets and 3D cross-linked g-C₃N₄ composites) synthesis processes and their possible fluorescence

quenching and recover performances in cancer cells.

6.2.3. Experimental Section

6.2.3.1. Materials and Chemicals

Melamine (99%), branched polyethylenimine (PEI, M.W: ~ 800 Da), Sodium borohydride ($NaBH_4$), sodium citrate (Na_3Ct), N-(3-Dimethylaminopropyl)-N'-ethylcarbodiimide hydrochloride (EDC), N-hydroxysuccinimide (NHS), 4,4'-Dithiodibutyric acid (95%), ethanol solution, dimethyl sulfoxide (DMSO) and other chemicals were purchased from Sigma Aldrich. Concentrated sulfuric acid (H_2SO_4, 98.0%), gold (III) chloride trihydrate ($HAuCl_4 \cdot 3H_2O$) and sodium hydroxide (NaOH, pellets) were purchased from Chem-Supply Australia Pty Ltd. Fetal bovine serum (FBS), Dulbecco's modified eagle medium (DMEM), Minimum Essential Media (MEM), sodium pyruvate (NaP, 100 mM), L-Glutamine (200 mM), HEPES (1 M) buffers, phosphate buffered saline (PBS, pH=7.4), trypsin (0.25%) and 3-(4,5-Dimethylthiazol-2-yl)-2,5-diphenyltetrazolium bromide (MTT) were purchased from Life Technologies Australia Pty Ltd. Human osteosarcoma cell line KHOS were purchased from American Type Culture Collection. All materials were of analytical grade and used as received without further purification. Millipore water was achieved from a three-stage Millipore Mill-Q plus 185 purified cation system (Academic) with a resistivity higher than 18.2 $M\Omega \cdot cm$.

6.2.3.2. Characterisation

Scanning electron microscopy (SEM) observations were carried out on a FEI Quanta 450 FEG environmental emission scanning electron microscope operated at 10 kV. IN addition, SEM observations were taken after each specimen coated 5 nm platinum layer by ion sputtering. Transmission electron microscopy (TEM) images were obtained by a

FEI Tecnai G2 Spirit transmission electron microscope at an acceleration voltage of 120 kV. Fourier transform infrared (FTIR) spectra were recorded at room temperature on a Thermo Scientific NICOLET 6700 FTIR spectrometer. The pH values were measured by a pH meter (EL20, MET-TLER TOLEDO). X-ray diffraction (XRD) patterns were obtained on a powder X-ray diffractometer at 40 kV and 15 mA using Co-Kα radiation (Miniflex, Rigaku). Raman spectrum were collected by a HORIBA Lab RAM HR Evolution equipped with 785 nm laser. Fluorescence emission and excitation spectra were recorded on a RF-5301PC spectrofluorophotometer (Shimadzu Scientic Instruments). Fluorescence traced images were taken on a ZEISS Axio Vert. A1 inverted microscope equipped with 370 nm laser.

6.2.3.3. Preparation of PEI-g-C$_3$N$_4$ Nanosheets

The bulk graphitic carbon nitride (g-C$_3$N$_4$) was prepared by 2 hours 600 °C thermal condensation of melamine with a ramp rate of 3 °C min^{-1} in a muffle furnace. Then bulk g-C$_3$N$_4$ powder (1 g) was dissolved in concentrated H$_2$SO$_4$ (20 mL) at 100 °C for 1 hour, natural cooled, and carefully injected into 70 °C ethanol (80 mL) with 800~1000 rpm stirring during the process. The precipitate acidified g-C$_3$N$_4$ was centrifuged at 16000 rpm, washed with deionized water and dried in a 60 °C oven for 24 h. Subsequently under sonication, acidified g-C$_3$N$_4$ (100 mg) was dispersed in water (100 mL) and adjusted the pH value to neutral by NaOH for further use. After the addition of EDC (100 mg) and HNS (100 mg) in the aqueous acidified g-C$_3$N$_4$ suspension, 100 mg mL^{-1} 800 Da PEI (2 mL) was added and then stirring for 24 h, PEI-g-C$_3$N$_4$ were centrifuged, washed and dried in a 60 °C oven for 24 h. Then PEI-g-C$_3$N$_4$ was dispersed in water to form aqueous PEI-g-C$_3$N$_4$ solution (1 mM) for further use.

6.2.3.4. Preparation of Au-PEI-g-C$_3$N$_4$ Nanosheets

Typically, 1 wt% HAuCl$_4$·3H$_2$O (100 µL) and water (9 mL) were mixed under 800~1000 rpm stirring at room temperature, and then 38.8 mM Na$_3$Ct (200 µL) solution was injected. After dropwise adding 0.075 wt% NaBH$_4$ (100 µL), gold nanoparticles were synthesised. Finally, gold nanoparticles were aggregated on PEI-g-C$_3$N$_4$ nanosheets under sonication, and formed purple solution containing Au-PEI-g-C$_3$N$_4$ nanosheets. The precipitate was centrifuged, washed several times, and re-dispersed in water for further use.

6.2.3.5. Preparation of Cross-Linked g-C$_3$N$_4$ Nanosheets

4,4'-Dithiodibutyric acid was dispersed in water to obtain aqueous solution (2 mM). EDC (100 mg) and HNS (100 mg) was added into 100 mL aqueous 4,4'-Dithiodibutyric acid solution and stirred for 1 h. Then aqueous PEI-g-C$_3$N$_4$ solution (1 mM, 100 mL) was put into the above system, after 24 h stirring, the products CL-g-C$_3$N$_4$ were filtered, centrifuged, washed repeatedly and re-dispersed in water.

6.2.3.6. Cell Culture and Material Biocompatibility

Cells were cultured in growth medium at 37 °C, 5% CO$_2$ and humidified atmosphere. The growth medium of human cervical cancer HeLa cells is 90% MEM, 10%FBS, 0.1% NaP, 0.1%L-Glutamin, 0.15% HEPES and 1% Anti-anti solution, while growth medium of human embryonic kidney cell line HEK 293T is in the same prescription, expect the 90% MEM was replaced by 90% DMEM. Material biocompatibility was measured by MTT assays, as MTT could access cell metabolic activity. The cellular oxidoreductase enzymes in living cells can reduce the tetrazolium dye MTT to formazan, which is a purple crystal and insoluble in cell culture medium. In a 96-well plate, cells were seeded at a density of 5×10^4 cells mL^{-1} in each well with their growth medium (100 µL). Subsequently after 24 h incubation, the previous medium was replayed by fresh medium (100 µL) together with various concentration of materials (Au-PEI-g-C$_3$N$_4$ and CL-g-C$_3$N$_4$). After another 24 h incubation, 0.5 mg mL^{-1}MTT

110

(10 μL) was added to each well and then incubated for a further 4 h. In the end, the medium in each well was replaced by 150 μL DMSO to dissolve formazan crystals. In dark conditions, the MTT assays were conducted in quadruplicate for each sample. The absorbance of formazan crystals was measured by an ELx808 Absorbance Microplate Reader (Biotek, USA) at 595 nm.

6.2.3.7. Cell Uptake of CL-g-C₃N₄ Traced by Fluorescence Microscopy

In a typical run, 2×10^5 HeLa and HEK 293T cells were seeded separately on a cover-glass with their own growth medium (2 mL) and in a well of the 6-well plates. After 24 h incubation at 37 °C, 5% CO_2 and humidified atmosphere, the medium was replaced by fresh medium containing CL-g-C₃N₄ composites. After another 4 h incubation, the cover-glass with cells and composites were carefully washed by PBS twice. The fluorescence traced image was taken by a ZEISS Axio Vert. A1 inverted microscope equipped with ~370 nm DAPI fluorescent port.

6.2.4. Results and Discussion

As shown in **Scheme 6.1**, in order to find novel g-C₃N₄ based traceable delivery systems, single layered low molecular weight PEI combined g-C₃N₄ nanosheets were post-functionalized in two ways. One is using gold nanoparticles attaching the g-C₃N₄ nanosheets, and to discover whether they are suitable for SERS tracing or not. The other one is using non-fluorescent polymer linker to cross-link g-C₃N₄ nanosheets, and to investigate the fluorescence quenching and recovery phenomena.
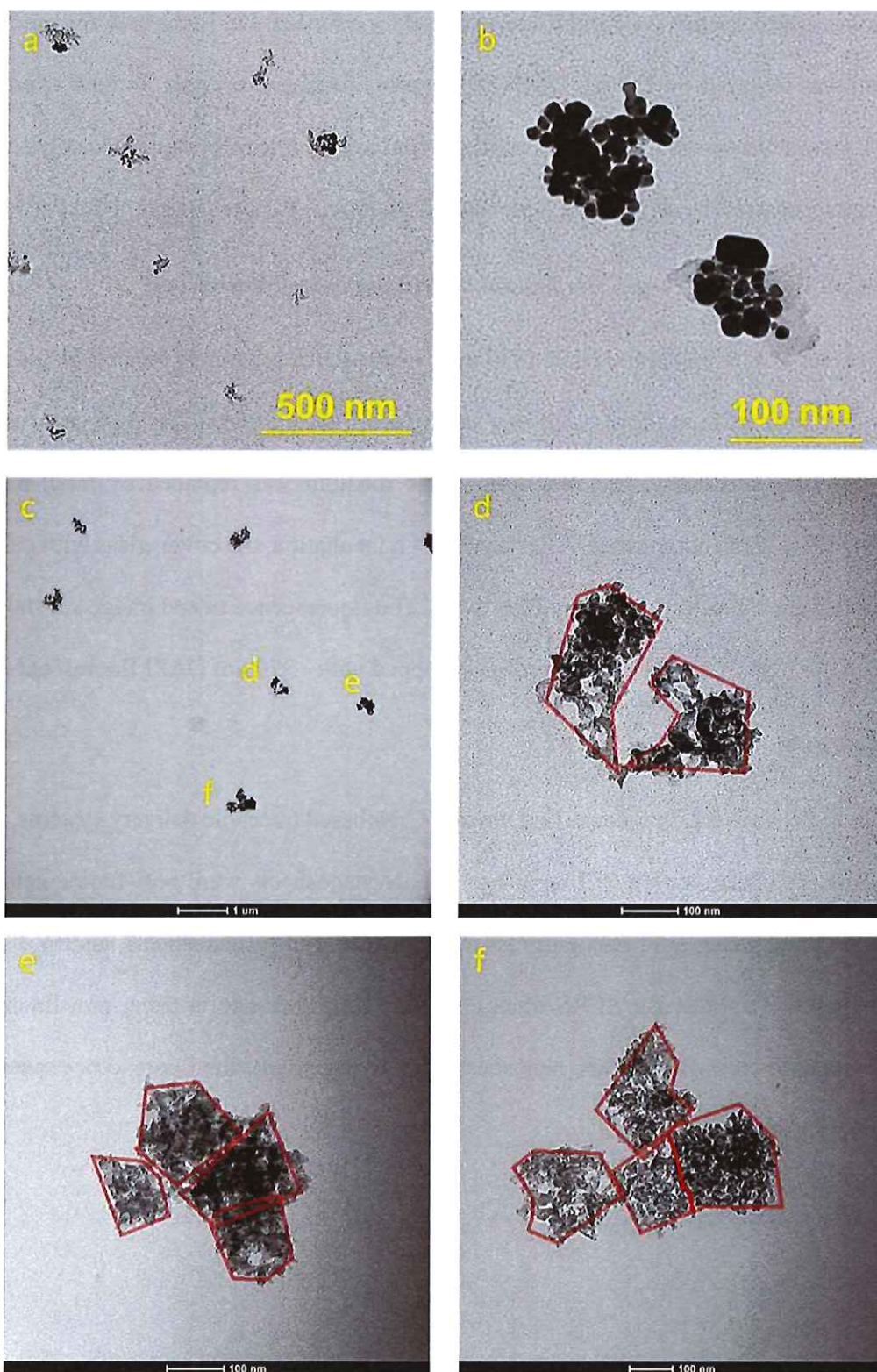
Figure 6.1. TEM images of Au-PEI-g-C$_3$N$_4$ nanosheets with low magnitude (a) and high magnitude (b) and TEM images of cross-linked g-C$_3$N$_4$ composites with low magnitude (c), high magnitude (d-f).

6.2.4.1. Synthesis of Au-PEI-g-C₃N₄ Nanosheets

Au-PEI-g-C$_3$N$_4$ nanosheets were synthesised by small gold nanoparticles attaching on PEI-g-C$_3$N$_4$ nanosheets. Transmission electron microscopy (TEM, **Figure 6.1a and b**) shows that small gold nanoparticles with size ranged from 2-20 nm were aggregated on layered PEI-g-C$_3$N$_4$ nanosheets with an average size around 100 nm. In FT-IR spectrum (**Figure 6.2**), peaks centre at 1620, 1562, 1470, 1404, 1318 and 1239 cm^{-1} are due to the skeletal vibrations of heptazine-derived repeating units of aromatic CN heterocycles, and peak-centre at 800 cm^{-1} is because of the breathing vibration mode of the tri-s-triazine units. Peaks centre around 3100 cm^{-1} are the results of N–H stretching vibrations from the absorbed H$_2$O molecules and amino groups. To verify the gold aggregation, wide-angle X-ray diffraction (XRD) analysis was conducted for PEI-g-C$_3$N$_4$ and Au-PEI-g-C$_3$N$_4$, the XRD pattern is shown in **Figure 6.3**. For both PEI-g-C$_3$N$_4$ and Au-PEI-g-C$_3$N$_4$, peaks centre at 13.3° and 27.4° can be considered as the evidence of (100) in-plane repeating tri-s-triazine units and (002) interlayer reflection of graphitic-like structures[21]. A standard XRD curve of the gold nanoparticle from JCPDS card no. 04-0784 is shown by red vertical line, which represent (111), (200), (220) and (311) planes. The diffraction angle of Au-PEI-g-C$_3$N$_4$ 2θ =38.18°, 44.39°, 64.58° and 77.55° can match the standard data. It also confirms the attachments between gold and PEI-g-C$_3$N$_4$ nanosheets. In addition, it can be noticed that there is a slight low shift of peak (002) from PEI-g-C$_3$N$_4$ to Au-PEI-g-C$_3$N$_4$, which can be attributed to interactions between gold and PEI-g-C$_3$N$_4$.

In **Figure 6.4**, two dominated peaks centre at 448 and 550 cm^{-1}, which can be noticed in the Raman spectrum of PEI-g-C$_3$N$_4$ nanosheets. While in the SERS spectrum of Au-PEI-g-C$_3$N$_4$, only peak centres at 559 cm^{-1} can be easily observed. The shift from 550 to 559 cm^{-1} may be attributed to the interactions between gold and g-C$_3$N$_4$. Based on that 559

cm^{-1} band intensity, effective enhancement factor (EEF) of Au-PEI-g-C$_3$N$_4$ can be roughly calculated by the following equation.

$$EEF = \frac{I_{SERS} N_{bulk}}{I_{bulk} N_{SERS}}$$

Where I_{SERS} and I_{bulk} are the intensities of SERS and bulk spectra at the 1078 cm^{-1} band, $\frac{N_{bulk}}{N_{SERS}}$ is the molar ratio between bulk and SERS sample[22, 23].

As demonstrated in the insect of **Figure 6.4**, EEF of Au-PEI-g-C$_3$N$_4$ is calculated as approximate 4.57×10^5, based on 550 cm^{-1} Raman peak and 559 cm^{-1} SERS peak. As the EEF is quite high, that means the Au-PEI-g-C$_3$N$_4$ nanosheets have the capability to conduct ultra-sensitive SERS trace.
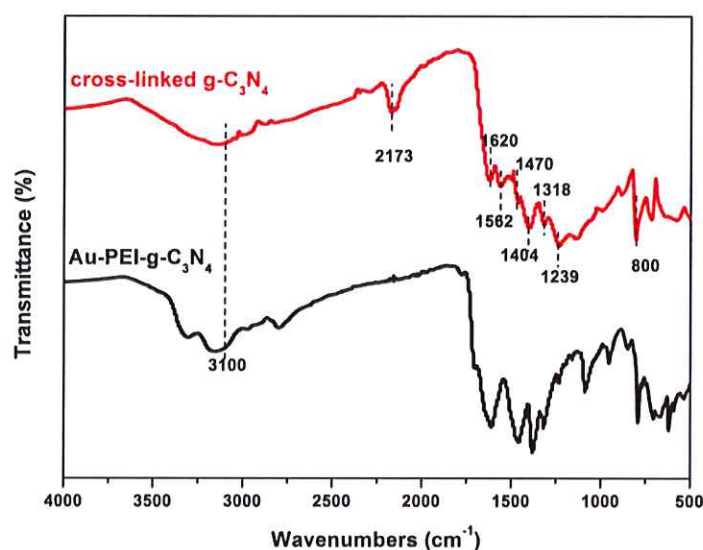
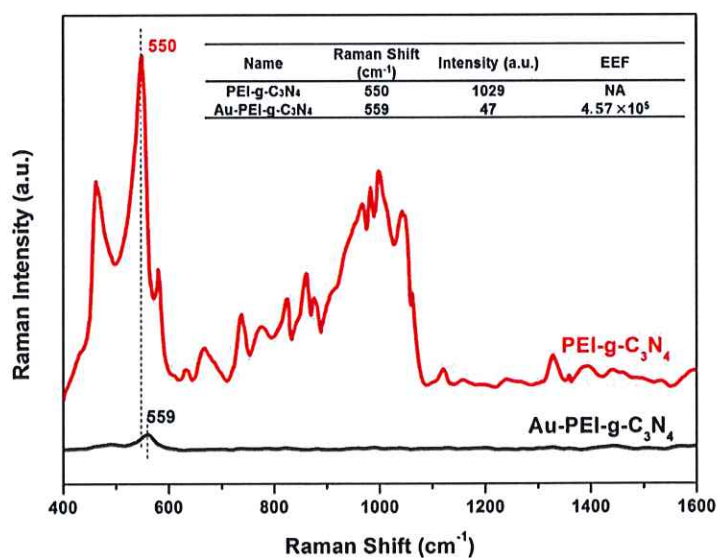**Figure 6.2.** FTIR spectra of cross-linked g-C$_3$N$_4$ composites and Au-PEI-g-C$_3$N$_4$ nanosheets.
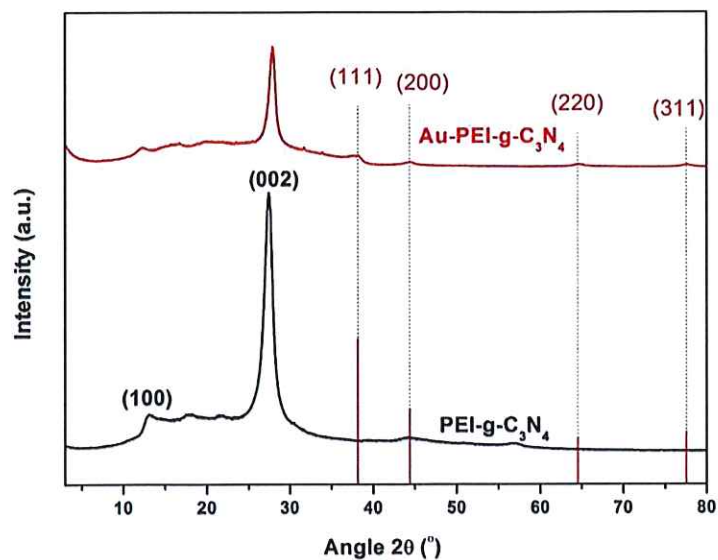
Figure 6.3. XRD pattern of PEI-g-C₃N₄ and Au-PEI-g-C₃N₄ nanosheets with standard intensity obtained from JCPDS card no. 04-0784.
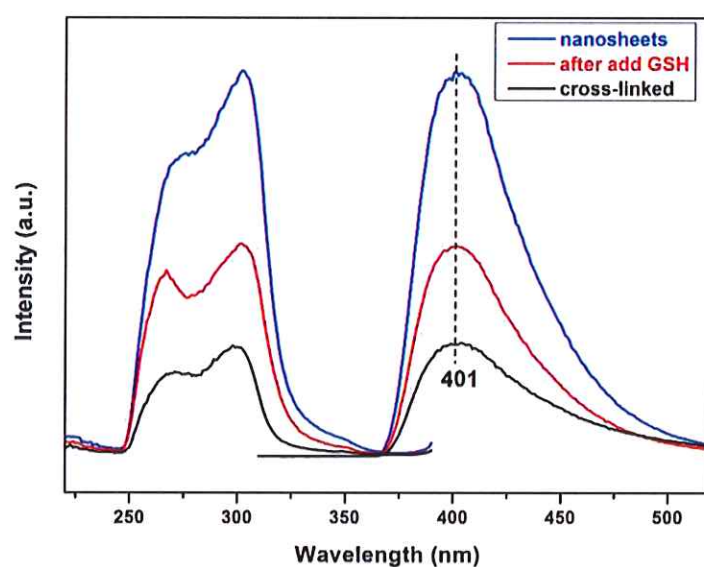

Figure 6.4 Raman spectra of PEI-g-C₃N₄ nanosheets, SERS spectra of Au-PEI-g-C₃N₄ nanosheets and the estimated effective enhancement factor.

6.2.4.2. Synthesis of CL-g-C₃N₄ Composites

Cross-linked graphitic carbon nitride (CL-g-C₃N₄) composites were fabricated by using

115

non-fluorescence polymer linkers with disulfide (-S-S-) bonds, which transfers the two dimensional materials to a three dimensional platform. 3D structure is great for endocytosis, which is the major cellular uptake mechanisms for pharmaceutics. TEM images (**Figure 6.1 c-f**) show that CL-g-C$_3$N$_4$ composites with an average size of 200 - 500 nm.are estimated as the combinations of two and more layered g-C$_3$N$_4$ nanosheets. From FT-IR (**Figure 6.2**), typical skeletal CN heterocycle vibration peaks centre at the range 1200-1600 cm^{-1} and the peak-centre of tri-s-triazine unit breathing mode 800 cm^{-1} can also be found, which confirms the structure of g-C$_3$N$_4$ are not damaged by cross-linkage. In addition, 2173 cm^{-1} peak-centre was attributed to C≡N and N=C=N groups[24, 25]. Peaks centre around 3100 cm^{-1} are the results of N–H stretching vibrations.

Figure 6.5. Fluorescence spectra of single layered PEI-g-C$_3$N$_4$ nanosheets, cross-linked g-C$_3$N$_4$ composites and GSH added cross-linked g-C$_3$N$_4$ composites.

6.2.4.3. Fluorescence Quenching of CL-g-C$_3$N$_4$ Composites

As illustrated in **Figure 6.5**, single-layer PEI-g-C$_3$N$_4$ nanosheets display fluorescent feature with maximum emission wavelength at 401 nm. However, CL-g-C$_3$N$_4$ composites have same

fluorescence peak at 401 nm with quite lower intensity. This phenomenon is called fluorescence quenching. Based on thiol-disulfide exchange reaction, the disulfide bond (-S-S-) can be cleaved into thiol (-SH) by the glutathione (GSH)[16-18]. After add GSH into the CL-g-C_3N_4 composites can cut the linkage between nanosheets. It can be found in **Figure 6.5**, there is an increase of the intensity of 401 nm peak. The reduction of fluorescence intensity value recovered a bit but still lower than single layer fluorescence value. Consequently, the fluorescence quenching phenomenon is proved.
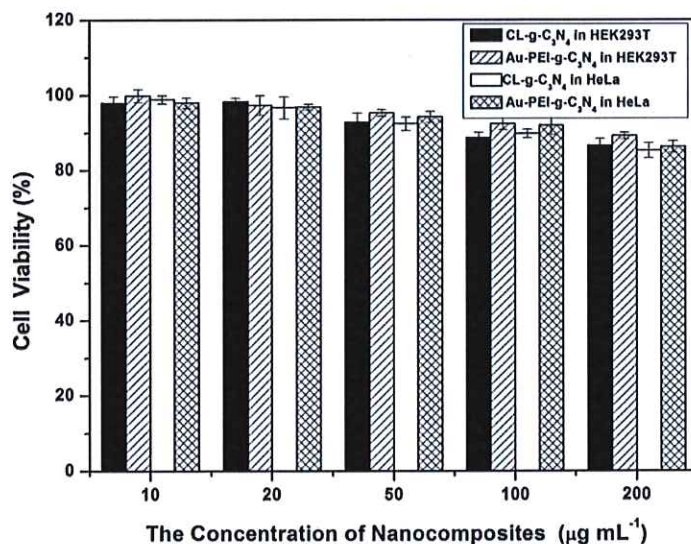
Figure 6.6. Biocompatibilities of CL-g-C_3N_4 composites and Au-PEI-g-C_3N_4 nanosheets in HEK 293T and HeLa cell line.

6.2.4.4. Biocompatibilities of Advanced Graphitic Carbon Nitride Nanocarriers

3-(4,5-dimethylthiazol-2-yl)-2,5-diphenyltetrazolium bromide (MTT) assays against human cervix carcinoma (HeLa) and human embryonic kidney (HEK 293T) cell lines were conducted to measure cell viabilities within material (CL-g-C_3N_4 composites and Au-PEI-g-C_3N_4 nanosheets) concentrations ranging from 10 to 200 µg mL^{-1}. As shown

in **Figure 6.6**, cell viabilities of both HeLa and HEK 293T cells remain above 85% at high material adding concentration 200 μg mL^{-1}, which means CL-g-C$_3$N$_4$ composites and Au-PEI-g-C$_3$N$_4$ nanosheets both have good biocompatibilities in cancer and normal cell lines.
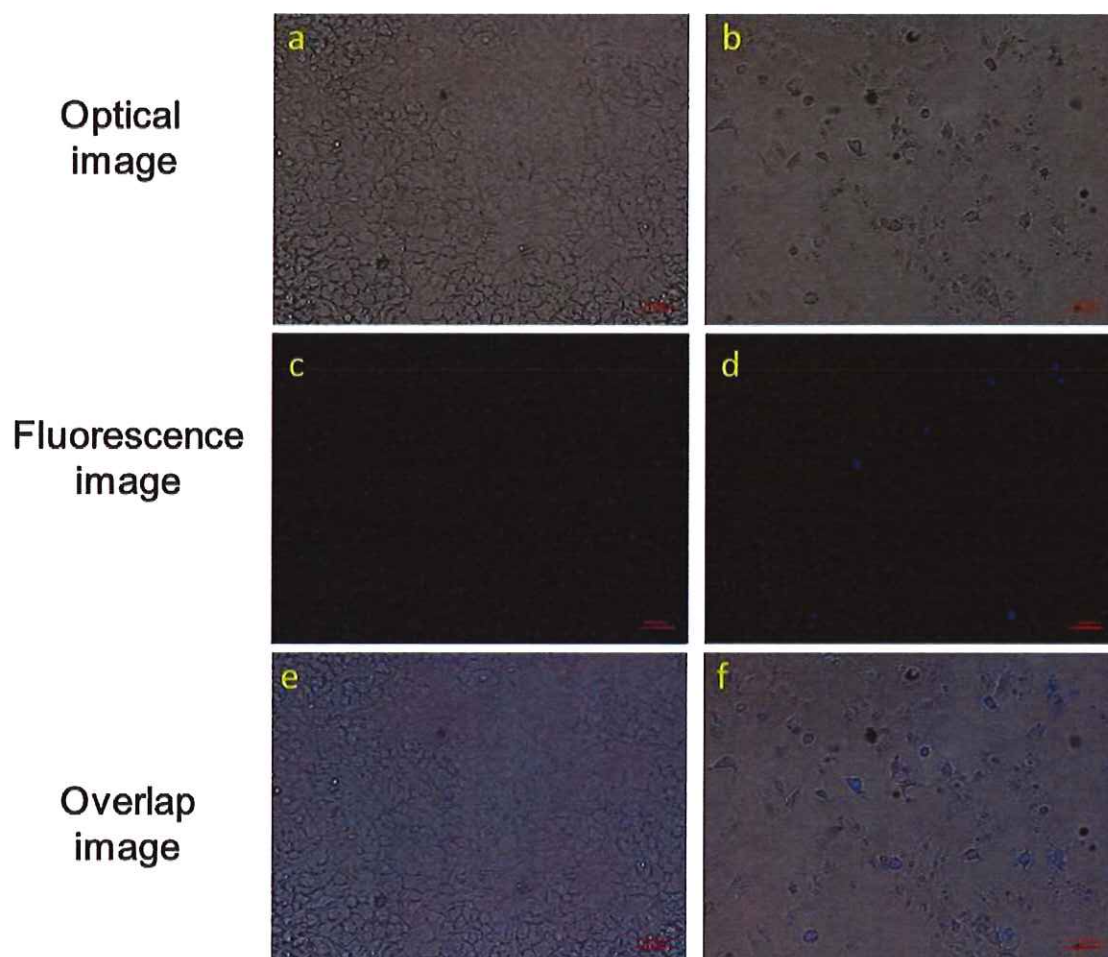
Figure 6.7. Fluorescence traced images of CL-g-C$_3$N$_4$ composites 4 h incubated in HEK293T cells (a, c, e) and HeLa cells (b, d, f) with scale bar of 50 μm.

6.2.4.5. Fluorescence Based Cellular Uptake and Cell Specificity

Since the intracellular concentration of GSH is quite higher than extracellular ones, and GSH concentration in cancer cells is also higher than health cells, the constructed CL-g-C$_3$N$_4$ composites have capability to be traced by fluorescence and have cell selectivity between

healthy and cancer cells. HEK 293T cells were grown well at the traced moment (**Figure 6.7a**). But the fluorescence intensity of CL-g-C$_3$N$_4$ composites is low and only display slight brightness in the traced image (**Figure 6.7c**). It can also be observed HeLa cells distributed in **Figure 6.7b**, and by compared between traced images (**Figure 6.7c and d**), in HeLa cells, the reduction of fluorescence intensity could be recovered better than it in HEK 293T cells. The merged images (**Figure 6.7e and f**) illustrate that the fluorescence traced result and optical observed results can match well. The fluorescence signals were collected from intracellular parts. The higher fluorescence in cancer than health cells demonstrated the designed smart CL-g-C$_3$N$_4$ composites have specificity for tracing intracellular performance in cancer cells.

6.2.5. Conclusion

Two kinds of novel advanced label-free g-C$_3$N$_4$ composite nanocarriers were designed and successfully synthesized. One is Au-PEI-g-C$_3$N$_4$ nanosheets for ultra-sensitive SERS analysis, as its EEF can reach as high as 4.57×10^5. The attachments of small gold nanoparticles on PEI-g-C$_3$N$_4$ nanosheets make it possible for SERS trace. The other one is cross-linked g-C$_3$N$_4$ composites, which design idea is obtained from the combination of redox responsible and fluorescence quenching. Interestingly, the fluorescence traceable CL-g-C$_3$N$_4$ composites is specific for cancer cells, as the fluorescence traced cellular uptake image in cancer cells is better than those in healthy cells.

6.2.6. Acknowledgements

6.2.7. Reference

[1]   Y. Chen, C. Tan, H. Zhang, L. Wang, *Chemical Society Reviews* **2015**, *44*, 2681.

[2]   D. Chimene, D. L. Alge, A. K. Gaharwar, *Advanced Materials* **2015**, *27*, 7261.

[3]   R. Kurapati, K. Kostarelos, M. Prato, A. Bianco, *Advanced Materials* **2016**, *28*, 6052.

[4]   C. E. Ashley, E. C. Carnes, G. K. Phillips, D. Padilla, P. N. Durfee, P. A. Brown, T. N. Hanna, J. Liu, B. Phillips, M. B. Carter, N. J. Carroll, X. Jiang, D. R. Dunphy, C. L. Willman, D. N. Petsev, D. G. Evans, A. N. Parikh, B. Chackerian, W. Wharton, D. S. Peabody, C. J. Brinker, *Nat Mater* **2011**, *10*, 389.

[5]   Y. Zhao, C. J. Wang, W. Gao, B. Li, Q. Wang, L. Zheng, M. Wei, D. G. Evans, X. Duan, D. O'Hare, *Journal of Materials Chemistry B* **2013**, *1*, 5988.

[6]   H. Wang, X. Yang, W. Shao, S. Chen, J. Xie, X. Zhang, J. Wang, Y. Xie, *Journal of the American Chemical Society* **2015**, *137*, 11376.

[7]   Z. Sun, H. Xie, S. Tang, X.-F. Yu, Z. Guo, J. Shao, H. Zhang, H. Huang, H. Wang, P. K. Chu, *Angewandte Chemie International Edition* **2015**, *54*, 11581.

[8]   L.-S. Lin, Z.-X. Cong, J. Li, K.-M. Ke, S.-S. Guo, H.-H. Yang, G.-N. Chen, *Journal of Materials Chemistry B* **2014**, *2*, 1031.

[9]   C. G. Liu, X. T. Wu, X. F. Li, X. G. Zhang, *Rsc Advances* **2014**, *4*, 62492.

[10]   X. Zhang, X. Xie, H. Wang, J. Zhang, B. Pan, Y. Xie, *J Am Chem Soc* **2013**, *135*, 18.

[11]   D. Lee, B. Lee, K. H. Park, H. J. Ryu, S. Jeon, S. H. Hong, *Nano Letters* **2015**, *15*, 1238.

[12]   X. Wang, N. D. Mansukhani, L. M. Guiney, Z. Ji, C. H. Chang, M. Wang, Y.-P. Liao, T.-B. Song, B. Sun, R. Li, T. Xia, M. C. Hersam, A. E. Nel, *Small* **2015**, *11*, 5079.

[13]   S. Xu, D. Li, P. Wu, *Advanced Functional Materials* **2015**, *25*, 1127.

[14]   X. Dong, F. Cheng, *Journal of Materials Chemistry A* **2015**, *3*, 23642.

[15]   X. Zhang, H. Wang, H. Wang, Q. Zhang, J. Xie, Y. Tian, J. Wang, Y. Xie, *Advanced Materials* **2014**, *26*, 4438.

[16]   R. Cheng, F. Feng, F. Meng, C. Deng, J. Feijen, Z. Zhong, *Journal of Controlled Release* **2011**, *152*, 2.

[17]   M. H. Lee, Z. Yang, C. W. Lim, Y. H. Lee, S. Dongbang, C. Kang, J. S. Kim, *Chemical Reviews* **2013**, *113*, 5071.

[18]   X. Du, B. Shi, Y. Tang, S. Dai, S. Z. Qiao, *Biomaterials* **2014**, *35*, 5580.

[19] X. Du, L. Xiong, S. Dai, F. Kleitz, S. Z. Qiao, *Advanced Functional Materials* **2014,** *24*, 7627.

[20] X. Du, L. Xiong, S. Dai, S. Z. Qiao, *Advanced Healthcare Materials* **2015,** *4*, 771.

[21] X. Wang, K. Maeda, A. Thomas, K. Takanabe, G. Xin, J. M. Carlsson, K. Domen, M. Antonietti, *Nature Materials* **2008,** *8*, 76.

[22] L. Wei, B. Jin, S. Dai, *The Journal of Physical Chemistry C* **2012,** *116*, 17174.

[23] P. H. C. Camargo, L. Au, M. Rycenga, W. Li, Y. Xia, *Chemical Physics Letters* **2010,** *484*, 304.

[24] X. Bai, J. Li, C. Cao, S. Hussain, *Materials Letters* **2011,** *65*, 1101.

[25] J. Zhang, M. Zhang, L. Lin, X. Wang, *Angewandte Chemie International Edition* **2015,** *54*, 6297.

Chapter 7 Conclusion and Perspective

7.1. Conclusion

The works in this thesis are aimed to develop a serial of functional composite nanoscale carriers for traceable drug/gene delivery based on conventional silica nanomaterials and emerging two dimensional graphitic carbon nitride materials with favourable size, morphology, structure and surface modifications, which can be used for fluorescence, Raman or surface-enhanced Raman scattering (SERS) trace applications. Based on researches, the following conclusions have been achieved:

1) Initially, we use easy accessed silica nanospheres to valid the feasibility of SERS trace.

A new smart DDS with 5-10 nm gold nanoparticles aggregated on the surface of silica nanoparticles with an average particle diameter of ca. 80-100 nm was designed through SERS-traceable nanocarriers baring carboxylic hydrazone-conjugated DOX anticancer agent. This design displays a *sesame-bread* structure to stimulate SERS effects by the aggregation of small exposed gold seeds. It is evident that the nanocarriers have adequate biocompatibilities, while the smart DDS exhibits selective cytotoxicities between cancer and healthy cells. By choosing DOX as anticancer model drug, intracellular uptake of DDS particles could be traced by compared SERS and fluorescence approaches. As SERS signals have higher sensitivities than fluorescence ones, it could effectively replace fluorescence in tracing. With further consideration of the non-destructive features of SERS methods, these designed DDS might be implemented to evaluate other general drugs without fluorescence. This point is also valid for general drugs without killing cell functions. In that case, we envision that these structured nanocarriers might have the capability to unveil dynamic processes of drug delivery in living cells.

2) Then we continued on developing advanced SERS tags based on silica materials, and applied in gene delivery.

A novel surface-enhanced Raman scattering (SERS) traceable gene delivery system has been synthesized under a stellate porous silica platform. In here, gold nanoparticles were obtained by in-site reduction of $HAuCl_4 \cdot 3H_2O$, and aggregated on silica skeleton by electrostatic and capillary adsorptions. The special gold-silica structure can give the delivery system SERS active effects, which allows the SERS trace be possible. In addition, SERS trace is great for delivery performance, as it has high sensitivity and non-invasive features, which makes the constructed delivery system have considerable capabilities to discover the real-tine delivery performances in living cells.

3) Subsequently, we combined emerging two-dimensional materials and selected graphitic carbon nitride (g-C_3N_4) as new platform for traceable delivery studies.

Novel designed low molecular weight branched PEI and almost single-layer g-C_3N_4 nanosheets composite gene delivery systems with 100-150 nm in sheet sizes and 0.6 nm in thicknesses were successfully used as Raman traceable gene carriers for the first time. Low molecular weight branched PEI components with good cellular biocompatibilities are aimed to change the zeta potentials of the system from negative to positive and offer the system higher siRNA binding capabilities than 800 Da PEI themselves. The uniform layered g-C_3N_4 nanosheets, which form the main part of delivery carriers, provide the system with high degree of surface functionalities to conjugate PEI functional groups and with Raman-active features that contributes to direct Raman tracing of the system without artificial labels. Raman tracing shows several competitive advantages over fluorescence like higher resolution and low signal to noise ratio, which makes it as a better method for real-time uptake visualizations and the intracellular performances tracing of delivery system.

4) Later, we developed advanced modified g-C$_3$N$_4$ nanocarriers for the purpose of extending their use for other high-sensitive bio-imaging applications and combining with stimuli-responsible linker to form smart nanocarriers.

Two kinds of novel advanced label-free g-C$_3$N$_4$ composite nanocarriers were designed and successfully synthesized. One is Au-PEI-g-C$_3$N$_4$ nanosheets for ultra-sensitive analysis, as its EEF can reach as high as 4.57×10^5. The attachments of gold nanoparticles make it possible for SERS trace. The other is a cross-linked g-C$_3$N$_4$ composite, which is designed by the combination of redox responsible and fluorescence quenching. Interestingly, the fluorescence traceable CL-g-C$_3$N$_4$ composites is specific for cancer cells, as the traced image of cellular uptake in cancer cells is better than those in health cells.

5) Finally, the differences between mesoporous silica nanoparticles and graphitic carbon nitride are summarized based on the advantages and disadvantages for used as nanocarriers.

Material Name	mesoporous silica nanoparticles	graphitic carbon nitride
Structure Control	mature and well-discovered synthesis method, easy to get uniform and control particle size, pore structure, pore size	an emerging material, not well-discovered synthesis method, hard to control size, require further steps to get uniform size
Morphology	nanoparticles are spheres, which is great for endocytosis.	two dimensional nanosheets
Functionalization	layer by layer functionalized, but the size may increase	functionalized based on stick layer to the surface, similar as layer to layer
Fluorescence Trace	non-fluorescent, need artificial fluorescent-marker	photoluminescence, fluorescent, can be used as label-free carriers
Raman Trace	no Raman-active, require artificial Raman-marker	have spontaneous Raman spectrum, can be used as label-free carriers.

7.2. Perspective

Based on the conclusions and work presented in the thesis, we propose some further research perspectives that can be possibly achieved in the following directions:

1) Multiple trace of nanocarriers and drugs/genes fate by SERS imaging.

In Chapter 3 and 4, it is evident that silica-gold nanocomposite carriers can successfully trace the intracellular uptake of carriers by SERS imaging. In addition, SERS imaging have high sensitivity and stability than fluorescence. As the fingerprint features of SERS signals, the influence of different SERS reporters is distinct. If we select two different SERS reporters grafted on carriers and drugs, it is possibly to trace their intracellular performances simultaneously, which is good for analyzing multi-drug delivery systems.

2) Continue the studies of SERS traceable $g-C_3N_4$ nanocarriers.

In Chapter 5, we find the single-layer $g-C_3N_4$ have spontaneous Raman intensity, while in Chapter 6, we confirmed that Au-PEI- $g-C_3N_4$ nanosheets have the possibilities for SERS imaging. As SERS imaging approach is non-destructive, the real-time trace of SERS traceable nanocarriers should have the possibility to figure out the dynamic intracellular performances of the samples in living cells.

3) Discover novel biocompatible materials for SERS traceable nanocarriers.

In this project, biocompatible silica was used for synthesis SERS traceable nanocarriers, but it required SERS reporter connections. Two dimensional $g-C_3N_4$ was used for constructing SERS traceable nanocarriers as an advanced platform, for $g-C_3N_4$ has spontaneous Raman spectrum. But $g-C_3N_4$ is not as good as silica to be easily biodegraded in vitro. In that case, both silica and $g-C_3N_4$ have their merits and demerits, the search of novel favorable biocompatible materials for SERS trace is still needed.

4) In vivo SERS trace.

In this project, all the work is conducted in vitro. However, in order to further clinic applications, the in vivo evolution is of great importance. The in vitro results can be different from in vivo ones, as there are a large majority of biological barriers and complex bio-chemistry reactions in the real body circumstances. The in vivo performances requires high resolution imaging techniques like SERS for trace and evaluation.

Appendix: Publications Based on this Thesis

1. L. Liu, Y. Tang, S. Dai, F. Kleitz and S. Z. Qiao. Smart Surface Enhanced Raman Scattering Traceable Drug Delivery System, Nanoscale, **2016**, 8, 12803-12811.

2. L. Liu, S. Dai, S.Z., Qiao, Papers have been prepared for submission. Advanced Silica based Surface-Enhanced Raman Scattering (SERS) Traceable Gene Delivery Systems (To be submitted).

3. L. Liu, Y. Tang, S. Dai, S.Z., Qiao, Graphitic Carbon Nitride Composites: Label-free Direct Raman Traceable siRNA Delivery System (To be submitted).

4. L. Liu, S.Z., Qiao, Advanced Label-Free g-C3N4 Composite Traceable Nanocarriers for Bio-Imaging and Traceable Delivery Applications (In preparation)